Magnetism and structure of Mn_xAu_{1-x} on Cu(001) and Ag(001)

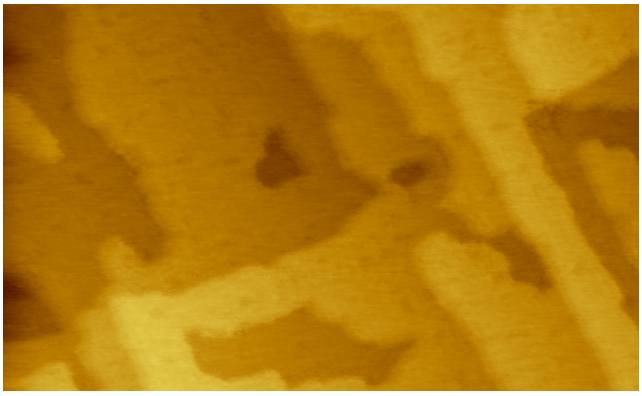

zur Erlangung des akademischen Grades des
Doktors der Naturwissenschaften (Dr. rer. nat.)
im Fachbereich Physik
der Freien Universität Berlin
eingereicht Dissertation

vorgelegt von

İsmet Gelen

Berlin, 2023

Approved by:

1. Gutachter: Prof. Dr. Wolfgang Kuch
2. Gutachter: Prof. Dr. Paul Fumagalli

Tag der Disputation: 17.04.2023

Declaration of authorship

Surname: Gelen
Name: İsmet

I declare to the Freie Universität Berlin that I have completed the submitted dissertation independently and without the use of sources and aids other than those indicated. The present thesis is free of plagiarism. I have marked as such all statements that are taken literally or in content from other writings. This dissertation has not been submitted in the same or similar form in any previous doctoral procedure.

I agree to have my thesis examined by a plagiarism examination software.

Date: Signature:

ABSTRACT

In this thesis, ultra-thin films of Mn_xAu_{1-x} have been studied structurally and magnetically. We prepared the thin films with electron-beam evaporators in ultra-high vacuum (UHV). The growth of the films was monitored by medium-energy electron diffraction (MEED). The films' structures were investigated by means of low-energy electron diffraction (LEED) and scanning tunneling microscopy (STM), and the chemical composition was checked by Auger electron spectroscopy (AES). The magnetic property of the antiferromagnetic (AFM) films in contact with FM films was studied by longitudinal magneto-optic Kerr effect (L-MOKE), X-ray magnetic circular dichroism (XMCD), and X-ray resonant magnetic reflectivity (XRMR) spectroscopy at $L_{2,3}$ absorption edge.

AFM Mn_2Au might be very significant for future spin-electronic applications. We studied Mn_xAu_{1-x} films in detail to investigate their structure for a variety of thicknesses on Cu(001) and Ag(001) single crystals. First, we studied Au/Mn/Co on Cu(001) to define the growth rate for Au, Mn, and Co using MEED. The vertical interlayer distances for Co on Cu(001) and Mn on Co/Cu(001) and surface topography of Au on Mn/Co/Cu(001) were investigated by LEED-I(V) (00 spot intensity was recorded vs. electron beam energy) and STM, respectively. After that, we studied from sub-ML (surface coverage of less than one monolayer) to more than 1 ML of Mn_xAu_{1-x} on Cu(001) structurally by LEED and STM. We observed a c(2×2) superstructure for coverages between 0.5 and 1 ML of Mn_xAu_{1-x} on Cu(001). Mn_xAu_{1-x} revealed MEED oscillations during growth on Cu(001), but no LEED patterns could be observed for thicker films ($>$ 1 ML). For studying the magnetic properties of AFM Mn_xAu_{1-x} on Cu(001), we grew Co on top, then we employed MOKE after zero-field cooling as well as after field cooling. We observed coercivity changes with temperature, however, we did not observe any exchange bias.

Finally, we studied Mn and Mn_xAu_{1-x} growth on Ag(001) to define the growth rate and structure of the resulting films. Fe growth on Ag(001) was also studied structurally. We deduced vertical interlayer distances for single-layer and bilayer films (Fe, Mn_xAu_{1-x}) on Ag(001) from a kinematic analysis of LEED-I(V) curves because both show LEED patterns. The Mn_xAu_{1-x} showed MEED oscillations during growth on Ag(001). Fe/Mn_xAu_{1-x} bilayers on Ag(001) were studied magnetically by MOKE. We did not observe any significant change in coercivity to confirm the antiferromagnetism of the Mn_xAu_{1-x} films.

KURZFASSUNG

In dieser Arbeit wurden ultradünne Mn_xAu_{1-x}-Filme strukturell und magnetisch untersucht. dünnen Schichten wurden mit Elektronenstrahlverdampfern im Ultrahochvakuum (UHV) hergestellt. Das Wachstum der Filme wurde mittels Mittelenergie-Elektronenbeugung (MEED) überwacht. Die Strukturen der Filme wurden mittels Niederenergie-Elektronenbeugung (LEED) und Rastertunnelmikroskopie (STM) untersucht, und die chemische Zusammensetzung mit Auger-Elektronenspektroskopie (AES) überprüft. Die magnetischen Eigenschaften der antiferromagnetischen (AFM)-Filme in Kontakt mit ferromagnetischen (FM)-Filmen wurden mit Hilfe des longitudinalen magneto-optischen Kerr-Effekts (L-MOKE), des magnetischen Zirkulardichroismus in der Röntgenabsorption (XMCD) und der Röntgenresonanzmagnetreflexionsspektroskopie (XRMR) an der $L_{2,3}$-Absorptionskante untersucht.

AFM Mn_2Au könnte für zukünftige spinelektronische Anwendungen von großer Bedeutung sein. Mn_xAu_{1-x}-Filme wurden im Detail untersucht, um ihre Struktur für verschiedene Dicken auf Cu(001)- und Ag(001)-Einkristallen zu untersuchen. Zunächst wurde Au/Mn/Co auf Cu(001) untersucht, um die Wachstumsrate für Au, Mn und Co mittels MEED zu bestimmen. Die vertikalen Zwischenschichtabstände für Co auf Cu(001) und Mn auf Co/Cu(001) und die Oberflächentopographie von Au/Mn auf Co/Cu(001) wurden mit LEED-I(V) (00 Spotintensität als Funktion der Elektronenstrahlenergie) bzw. STM untersucht. Danach wurden sub-ML (Oberflächenbedeckung von weniger als einer Monolage) bis hin zu mehr als 1 ML von Mn_xAu_{1-x} auf Cu(001) strukturell mit LEED und STM untersucht. c(2×2) Überstrukturen wurden für Bedeckungen zwischen 0,5 und 1 ML von Mn_xAu_{1-x} auf Cu(001) beobachtet. Mn_xAu_{1-x} zeigte MEED-Oszillationen während des Wachstums auf Cu(001), aber es konnten keine LEED-Beugungsbilder für dickere Schichten ($>$ 1 ML) beobachtet werden. Um die magnetischen Eigenschaften von AFM Mn_xAu_{1-x} auf Cu(001) zu untersuchen, wurde Co auf Mn_xAu_{1-x}/Cu(001) aufgewachsen und anschließend, durchgeführt MOKE-Messungen nach Null-Feld-Kühlung und Feld-Kühlung, bei denen beobachtet wurde, dass sich die Koerzitivfeldstärke mit der Temperatur ändert, jedoch keine Austauschverschiebung zu messen ist.

Schließlich wurde das Wachstum von Mn und Mn_xAu_{1-x} auf Ag(001) untersucht, um die Wachstumsrate und die Struktur der entstehenden Filme zu bestimmen. Das Fe-Wachstum auf Ag(001) wurde ebenfalls strukturell untersucht. Aus einer kinematischen Analyse von LEED-I(V)-Kurven wurden vertikale Zwischenschichtabstände für einschichtige und zweischichtige Filme (Fe, Mn_xAu_{1-x}) auf Ag(001) abgeleitet, da beide LEED-Beugungsbilder aufweisen. Mn_xAu_{1-x} zeigte MEED-Oszillationen auf Ag(001). Fe/Mn_xAu_{1-x}-Doppelschichten auf Ag(001) wurden mit MOKE magnetisch untersucht, wobei keine signifikante Änderung der Koerzitivfeldstärke zur Bestätigung des Antiferromagnetismus von Mn_xAu_{1-x}-Filmen zu beobachten war.

Contents

List of Tables

List of Figures

CHAPTER 1

Introduction

Magnetism has played a significant role in human life. Around 2500 B.C., the Chinese were using the compass, and at 600 B.C., magnetite was known that attracted iron [1]. Later on, the earth was found to be a huge magnet by Gilbert (1540 - 1603). After investigating the magnetic pole, P. Peregrines made a piece of iron that was attracted more by a magnetic pole than magnetite (around 1269 A.D.). Then Coulomb (1736 - 1806) measured the forces between magnetic poles of long thin steel rods quantitatively [1].

As briefly defined in the history of magnetism above, we know that magnetism has a wide range of applications. It is used as a magnetic compass to find the direction, but also in motors and generators. Besides the previously mentioned important applications of magnetism, it is also being used in read heads in hard disks since 1956 [2]. After Grünberg [3] and Fert [4] found the giant magnetoresistance (GMR) effect, both of them shared the Nobel Prize in 2007. Consequently, the hard disk read head was made based on the GMR principle, which increased the read head performance and areal storage density by replacing anisotropic magnetoresistance (AMR) heads, so the hard disk physical size reduced. Later on, tunneling magnetoresistance- (TMR-) based heads also have been used commercially by Seagate [5]. In general, by the improvement in read/write heads from the 1950s till now, while the hard disk physical size shrank, the storage capacity increased, and the price also decreased [6]. Another significant application of magnetism is data storage. Therefore, magnetic-based data storage has attracted more attention in recent years due to the increasing demand of mass data storage. While current magnetic data storage devices seem to be almost at their limit [7], spin electronic logic devices could potentially, consume less power than current electronics and, at the same time, include non-volatile memory functions [8]. Therefore, the investigation

of novel materials and the study of their magnetic properties is very crucial. Studies of magnetic thin films become significant for understanding how to control the magnetic property of materials. Magnetic interface coupling is crucial for understanding antiferromagnetic (AFM)/ferromagnetic (FM) interface coupling to prevent other effects such as contamination, roughness, and defects: ultra-thin film preparation on a single crystal is one of the prominent methods to yield the opportunity to control and characterize the interface very effectively. The material concentration or thickness has a big influence on the magnetic properties. In magnetic thin films, the exchange-bias field (H_{EB}) depends on AFM/FM thickness, interface disorder, and orientation, which can all be controlled [9]. The exchange bias is a shift in the magnetic loop along the magnetic field axis in an AFM/FM exchange-coupled system [9]. The work needs ultra-thin films which can be prepared in an ultra-high vacuum (UHV) system to evade contamination and guarantee high-quality film growth.

AFM materials are very prominent materials that could be used in future spintronic devices because they are robust against magnetic fields, and have an ultra-fast dynamics [10, 11]. AFM materials have been examined for around 60 years [12]. The purpose of studies of magnetic materials for data storage is to improve energy consumption and scale [12]. While AFM materials are antiparallel magnetic ordered, FM materials are parallel magnetic ordered, therefore AFM does not have a net magnetic moment, but FM does. AFM materials are vital to use in magnetic data recording since the stored data will not be deleted or affected from an external magnetic field because they are robust to the magnetic field.

A variety of AFM materials have been studied by many scientists. Mn is an interesting AFM material because of its rich phase diagram with different ground states corresponding to body-centered cubic (bcc), simple cubic (sc), and face-centered cubic (fcc) phases. Mn forms a variety of alloys that are AFM, such as FeMn, IrMn, RhMn, and RuMn, which all have a face-centered cubic (fcc) structure. Mn alloys also comprise of NiMn [13, 14, 15], PtMn, and PdMn, which have a face-centered tetragonal (fct) crystal structure and offer the advantage of having

a higher blocking temperature. Moreover, most of them need post-annealing during or after evaporation to obtain the desired phase. Mn-Au also creates alloys that have multiple phases. These are Mn_2Au (Néel temperature, T_N 1600 K) [16], MnAu (T_N 523 K [17], 503 K [18]), $MnAu_3$ (T_N 140 K), and Mn_3Au_5 (T_N 354 K) [19]. Au_2Mn is an AFM with T_N 363 K, and nevertheless, Au_4Mn is an FM with Curie temperature T_C 371 K [20].

Mn_2Au, theoretically [16, 21] and experimentally [17] has been proven to be an AFM material. Mn_2Au is a crucial material that can be switched by applying an electrical current perpendicular to the locally broken inversion symmetry axis [22]. However, first CuMnAs was experimentally investigated with respect to electrical switchability [23]. Later, Mn_2Au also achieved this [24]. Mn_2Au has some advantages compared to CuMnAs, for example, it is not as toxic as CuMnAs. Mn_2Au (T_N above 1000 K [17]) has a higher Néel temperature than CuMnAs (T_N 480 K [23]). Its high T_N makes it thermally more stable in the AFM-ordered state. The uniaxial magnetic anisotropy in Mn_2Au AFM films can be switched by an electric field. In the work of Chen et al., they observed an asymmetric Néel spin-orbit torque [25]. Changing the magnetic order by electric current pulses is a promising approach to obtain fast spintronic devices [26]. AFM-based materials can be used in ultrafast spin dynamics. They are even 2-3 orders of magnitude faster than FM materials [27]. Roy et al. also show the possible ultrafast switching of Mn_2Au [22]. The spin Hall effect was observed in Mn_2Au by Chen et al. [28]. All these properties make Mn_2Au a promising candidate in future memory devices [29].

Ultra-thin films can be prepared by various methods such as magnetron sputtering, pulsed-laser deposition, chemical/physical vapor deposition, and molecular beam epitaxy. In this work, the ultra-thin films were prepared by electron beam evaporation in the Ångstrom (Å) thickness range. The film thickness was monitored by medium-energy electron diffraction (MEED). Thin films were elementally, structurally, and morphologically analyzed by means of Auger electron spectroscopy (AES), low-energy electron diffraction (LEED), and scanning tunneling

microscopy (STM), respectively.

The magnetic properties of the AFM and FM thin films were investigated via magneto-optic Kerr effect (MOKE) by observing the exchange-bias field (H_{EB}) and coercive filed (H_C) changes. We also used X-ray magnetic circular dichroism (XMCD) and X-ray resonant magnetic reflectivity (XRMR) spectroscopy at the $L_{2,3}$ absorption edges to investigate the magnetic properties of the samples. The film growth and analysis should be done under UHV conditions in order to obtain clean films. The samples can be measured in other chambers by transferring them either by capping thin films or in a vacuum suitcase.

In this thesis, the goal was to prepare well-ordered single-crystalline films with different concentrations in order to see how this influences the magnetic coupling to the FM layer, how these films can be grown with an FM layer in contact, how the interface would look like, how the films could be covered with a protective overlayer and how this would change the properties magnetically and structurally. Therefore, in order to prepare a well-ordered single-crystalline film, we prepared our thin films on the single-crystal surfaces Cu(001) and Ag(001). Cu(001) and Ag(001) are chosen because these two single crystal surfaces have not been used before as a substrate for Mn_xAu_{1-x} films. Cu(001) was selected especially for the growth of sub-ML to investigate Mn-Au alloy formation, and we could also compare to the growth of Mn or Au on Cu(001) structurally by STM and LEED. These two single crystals can be cleaned by Argon ion sputtering and annealed to 900 K, which is possible for our experimental setup and does not require much effort or time. Therefore, we used two different single crystals as a substrate. On the other hand, Co and Fe grow epitaxially on Cu(001) and Ag(001), respectively. We study different Mn-Au alloy ratios and different thicknesses on these single crystals (Ag(001), Cu(001)). We investigate the films' growth mode and structure. For studying magnetic properties, we grow Mn_2Au in contact with an FM layer. We also studied Mn_xAu_{1-x} in the sub-ML regime by scanning tunneling microscopy (STM) to determine the initial stages of growth.

This thesis is organized as follows. Chapter 2 is devoted to the experimental setup, and the preparation and analysis methods of the thin films will be discussed. Chapter 3 briefly presents the theoretical background of this study. In Chapter 4, the growth of Au, Mn, and Co on Cu(001) was studied by means of LEED, LEED-I(V), MEED, AES and XMCD, and XRMR. We could define Co, Mn, and Au growth rates from MEED oscillations.

In Chapter 5, the growth of a sub-ML (sub-monolayer $<$ 1 ML) Mn_xAu_{1-x} on a single crystal of Cu(001) is studied to investigate the Mn_xAu_{1-x} thin films' structure in the sub-ML regime and above 1 ML. The structure and morphology of the films were studied by LEED and STM, respectively. The Mn and Au are already individually studied on Cu(001) by STM in the sub-ML regime. 0.5 ML Au grown on Cu(001) [30] and 0.5 ML Mn grown on Cu(001) display a c(2$\times$2) superstructure in LEED [31]. However, we investigate the same LEED pattern for a Mn-Au alloy in the sub-ML regime on single-crystalline Cu(001).

In Chapter 6, we aim to study the magnetic property of Mn_xAu_{1-x}. Therefore, we grow Co on Mn_xAu_{1-x}/Cu(001) to find the AFM/FM coupling and measure MOKE for field cooling and zero field cooling. The MEED oscillations for Mn_xAu_{1-x} on Cu(001) help to define the film thickness. The structure of the films was studied by LEED. However, there was no clear LEED image for Mn_xAu_{1-x} on Cu(001).

In Chapter 7, the growth of Fe/Mn_xAu_{1-x} on a single crystal of Ag(001) was studied. Our objective for Chapter 7 was to find the AFM/FM coupling. The structure of the films was studied by LEED. We also study the structure of Mn grown on Ag(001) by means of AES, LEED, and LEED-I(V) to compare to the Mn_xAu_{1-x} on Ag(001). The magnetic properties of Fe/Mn_xAu_{1-x} bilayers on Ag(001) samples were studied by MOKE.

Finally, in Chapter 8, we summarized the main conclusions of all works done in this thesis.

CHAPTER 2

Experimental Setups

The thin films in this thesis were prepared in ultra-high vacuum (UHV) by electron-beam-assisted thermal evaporation in the range from few Ångstrom (Å) to nanometer (nm) thickness on single-crystal surfaces. Materials were either rods, or pieces in a crucible. Gold was placed directly inside a tungsten filament for thermal evaporation. The thin films' growth was monitored by MEED. The sample structure was analyzed by LEED and STM. The chemical composition and cleanliness of the samples were checked by AES. The magnetic properties were studied by MOKE and XMCD. In this chapter, we focus on the methods that were used for growing and analyzing the samples.

The chamber has two main parts. The first part is the preparation chamber, which has three electron-beam evaporators, LEED (Omicron), AES (PHI-155A), L-MOKE, MEED, mass spectrometer, and sputtering gun (SPECS) as they are depicted in Fig. 2.1 (a). The electron-beam evaporators are one single Omicron and two Oxford 4-pocket (EGN4) electron beam evaporators. The second part has just an analysis part with STM and P-MOKE, which is shown in Fig. 2.1 (b). The preparation chamber is pumped by an ion getter pump, a turbomolecular pump (TMP), and a titanium sublimation pump (TSP) that allow to reach a base pressure of around 3×10^{-10} mbar after baking at around 150 °C for 36 hours. The second part is pumped by an ion getter pump only in the case of the closed valve between preparation and STM chamber with a base pressure of around 2×10^{-10} mbar.

In the preparation chamber, there is a load lock to load or unload the samples from the air. A UHV suitcase is also used for transferring the sample to other chambers without breaking the vacuum and preventing the sample from contamination. The transfer of the sample from the load lock to the manipulator or to a transfer rod, by which the sample can be transferred to the STM chamber, is done by a wobble

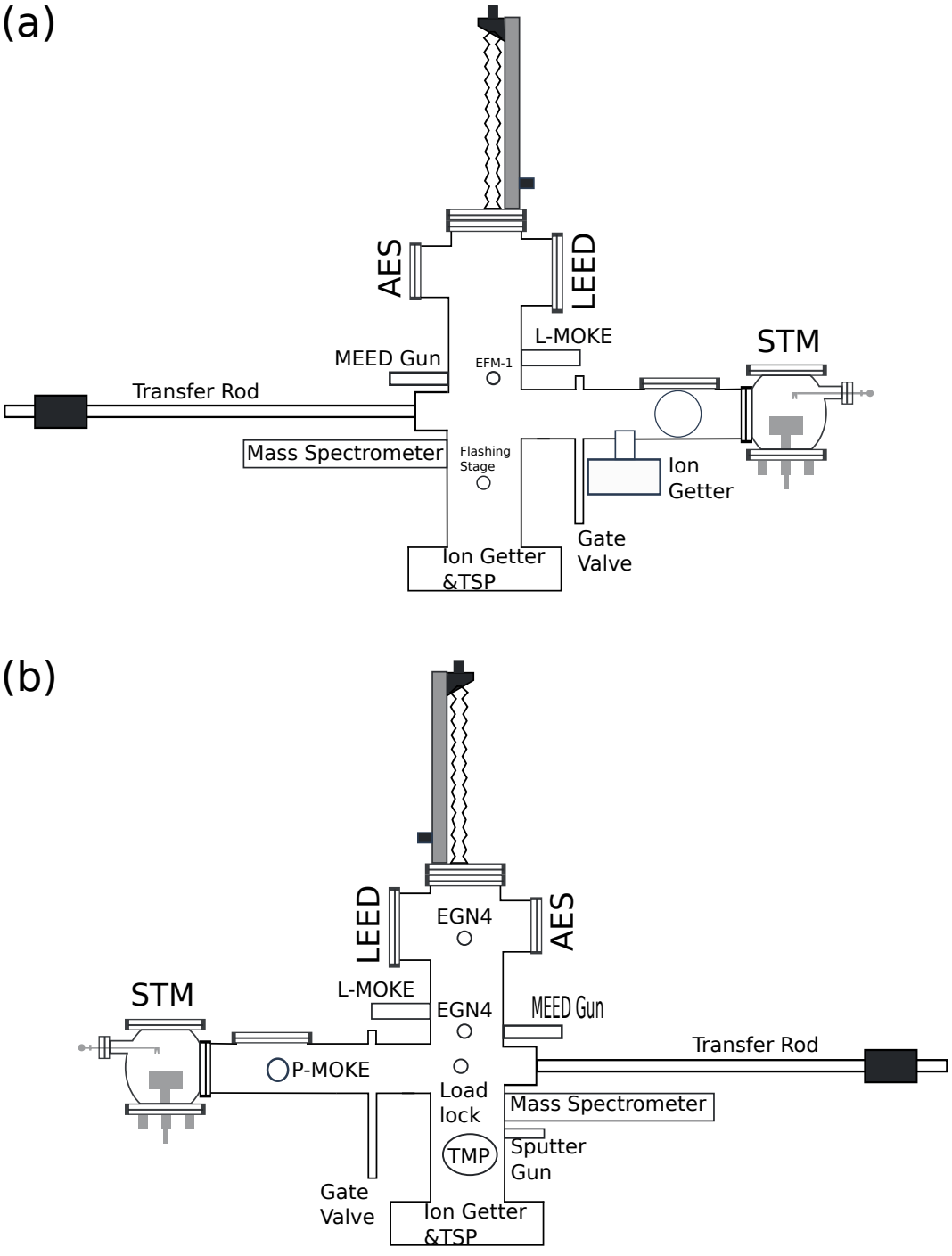

Figure 2.1: Experimental setup of preparation and STM chambers (a) front and (b) back views.

stick in the preparation chamber. The manipulator has five axes that give freedom to adjust the sample for LEED, MEED, MOKE, and sputtering as well as grabbing by the wobble stick. The sample holder on the manipulator has two K-type thermocouples that are mounted below and above the sample. The sample is electrically isolated from ground, such that the sample current can be monitored during AES, LEED, and sputtering. The sample heating on the manipulator is done by a tungsten filament which can heat the sample up to 1000 K. The sample can also be cooled down by liquid nitrogen (LN_2) to about 160 K. Substrates like tantalum and tungsten need higher temperatures to be cleaned. Therefore, a flashing stage has been built for the preparation chamber that can heat the substrate to above 2000 °C by electron bombardment.

2.1 Growth Methods

The materials are picked as rods for Co (99.99% purity, diameter 2 mm) and Fe (99.99% purity, diameter 2 mm), wire for Au (diameter 1 mm), and pieces for Mn (99.99% purity, diameter 2 mm), because of the way they can easily be evaporated by electron-beam evaporators.

The growth has been performed as follows: The first step is cleaning the substrate by Ar^+ sputtering. The cleanliness of the sample is assured by AES, where contaminations were below the detection limit. Subsequently, the sample is annealed at the required temperature. After annealing, the cleanliness and surface quality are checked again by AES and LEED, respectively. Then the thin films are deposited, while the growth is monitored by MEED. The MEED displays intensity oscillations if the growth is layer-by-layer. Indeed, growth can proceed in three different growth modes depending on material, temperature, deposition rate, and substrate. When films grow layer-by-layer, it means an atomic layer is completed before starting the growth of a new layer, which is called Frank-van der Merwe (FvM) growth mode. If the first layer is completed and then island growth starts, it is called Stranski-Krastanov (SK) mode. If islands are created from the begin-

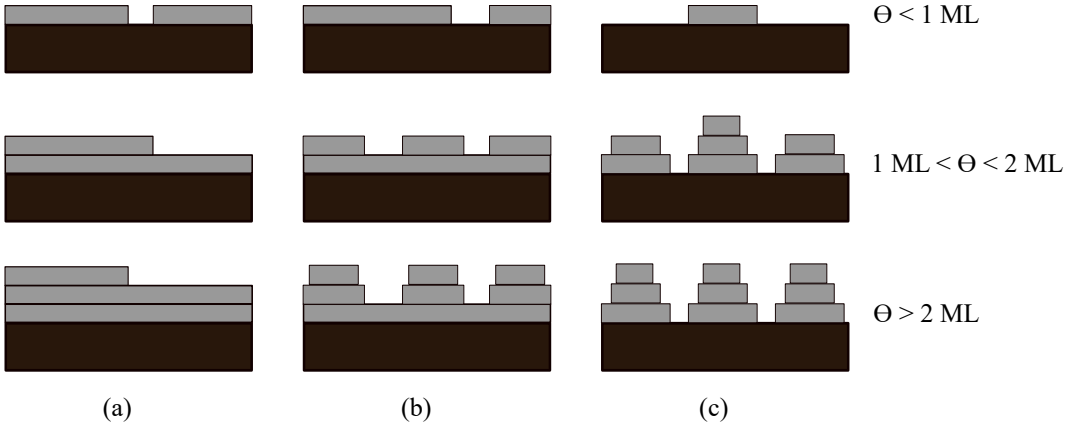

Figure 2.2: Sketch views of the three main growth modes of thin films consisting of (a) Frank–van der Merwe (FvM), (b) Stranski–Krastanov (SK), and (c) Volmer–Weber (VW) growth. Three different coverages are shown for each growth mode. Reprinted with permission from [32, 33] by Springer Nature and Copyright Clearance Center.

ning, it is called Volmer-Weber (VW) growth, as depicted in Fig. 2.2 (a), (b), (c), respectively.

Last but not least, for the thin-film growth mode, the interaction potential between film and substrate is very crucial. If the interaction potential for the adatoms themselves is bigger than the interaction potential between the film and substrate, then the adatoms will grow as three-dimensional growth. But, if the strength of the interaction potential between the film and substrate is bigger than the interaction potential between the adatoms themselves, then the film will follow a layer-by-layer growth [34]. The Ehrlich–Schwoebel barrier (or step-edge barrier) height is very important for layer-by-layer growth because, if the adatoms can cross the step edge and stick at the lower edge, then they can lead to layer-by-layer growth. However, when the Ehrlich–Schwoebel barrier is too high, then they form islands [35].

2.1.1 Substrate Preparation

The substrate preparation is very important for the growth of epitaxial thin films. In this work, polished single-crystals of Cu(001) and Ag(001) (Mateck, diameter 10 mm, 2 mm thickness) with miscut $\leq 0.1°$ were mounted on Omicron molybdenum plates with Ta wire. The Ta wire was spot-welded to the plate. The substrates were sputtered by several cycles of 1 keV Ar^+ bombardment at 8×10^{-6} mbar and

subsequent annealing around 900 K. The sample current was monitored during sputtering by a Keithley digital multimeter (between 6.5 µA and 7.0 µA). The thermocouple wires are connected very close to the Mo plate to read the correct temperature of the sample. The benefit of using these single crystals in situ is that they can be reused. After the sample preparation and all the measurements, the sample can be resputtered to remove the films. Depending on film thickness, sputtering can take up to six or more hours. After annealing the single-crystal, the LEED pattern displays very sharp spots. This indicates a well-ordered, unreconstructed surface. After all these processes, the substrate can be used for another sample preparation again. AES is very significant to check the sample cleanliness after annealing, even if this displays substrate LEED pattern because the annealing process can let bulk impurities diffuse to the surface, which causes contamination that might not become visible in LEED images.

2.1.2 Ultra-Thin Film Preparation

The samples to be discussed here are ferromagnetic and antiferromagnetic thin films. The samples were prepared by electron beam evaporation on Cu(001) and Ag(001). The typical thickness of the FM and AFM films discussed here is in the range of less than 1 ML up to 30 ML (monolayer). Mn on Cu(001) does not grow layer-by-layer, Cobalt (Co) is grown on Cu(001) layer-by-layer. This can be monitored by MEED. After the growth of Co, Mn can be grown on Co/Cu(001) layer-by-layer and shows MEED oscillations [36]. From these oscillations, the Mn growth rate can be obtained. Then the growth of Mn_2Au on Cu(001) can be obtained by adjusting the gold rate accordingly.

The Mn_xAu_{1-x} thin films were prepared by electron beam evaporation. The Mn is from Mateck company with 99,99 % purity and consists of pieces from 3 mm to 12 mm size. The Mn pieces were filled in a tantalum (Ta) crucible. The Ta crucible was cleaned with acetone and ethanol in an ultrasonic bath for around 30 min. The Ta crucible was mounted to a small chamber that is dedicated to the crucible

preparation, with a base pressure of $\sim 1 \times 10^{-7}$ mbar. In this chamber, the crucible was degassed by electron bombardment. After degassing the crucible, it was let to cool down to room temperature (RT), was taken out, and filled with Mn pieces. The Mn was either prepared in this small chamber or directly mounted in the electron beam evaporator. The preparation of Mn in the small chamber consisted of melting the Mn to wet the crucible to prevent falling out from the crucible during or after mounting the electron beam evaporator. When the crucible is filled with Mn pieces, the Mn pieces were blocked by fixing the crucible by a tungsten (W) wire. The evaporator was mounted in a horizontal way to the small chamber. Then the chamber was baked for 24 h. After the bake-out, the filament and Mn-filled crucible were gradually degassed. When the degassing is completed, the power for the crucible is increased for a few seconds to a high power to melt the Mn. If it is exposed for a too long time, the whole Mn can evaporate. After melting the Mn in the crucible and cooling down to RT, it is ready to mount to the electron beam evaporator. The degassing and melting can be done in the preparation chamber, too. Co and Fe are mounted to the EGN4 evaporator as rods 2 mm in diameter. A gold (Au) wire (1 mm in diameter) was wrapped by a tungsten wire and then mounted to the EGN4. Before the thin film evaporation, the materials and filaments were degassed. The base pressure was 5×10^{-10} mbar; during material evaporation, the pressure rose to around $\approx 5 \times 10^{-9}$ mbar.

2.2 Analysis Methods

The single crystals and the ultra-thin film crystal structure are checked by LEED images, and the vertical layer distance of the films is examined by LEED-I(V). The same LEED system is also used to do AES, but not for all measurements. For most samples, a PHI-Auger (10-155A) was used to provide the elemental composition of the thin films. After the structural and chemical investigation of the thin films is completed, the surface morphology is investigated by STM. Subsequently, the magnetic properties of the films are measured in-situ by L-MOKE. In this section,

the analysis method will be explained in detail.

2.2.1 Low-Energy Electron Diffraction

The low-energy electron diffraction (LEED) was first discovered by Clinton Davisson and Lester Germer in 1925 at Bell Labs in New York [37]. In 1937 Davisson and Thomson got the Nobel Prize because of the experimental study of the diffraction of electrons by crystals. Indeed Davisson and Germer were looking for elastic scattering of electrons from a nickel crystal. The scattering distribution was changing by azimuthal angle and applied voltage. The electron wave behavior was already suggested by Louis De Broglie in 1923. Their experimental works agreed to de Broglie's electron wave behavior. In general, LEED studies became popular after the 1960s when UHV systems improved.

A simplified sketch of a LEED setup is shown in Fig. 2.4 (a). The LEED optics consist of a beam gun, four hemispherical concentric grids, and a phosphor screen. The beam gun consists of filament, wehnelt, 4 lenses, and anode. Grid 1 is earth-grounded, 2 and 3 are used for retardation, 4^{th} one is on 0 V. The grids are used for screening out the inelastically scattered electrons. The LEED optic and LEED power supply control are from SpectaLEED Omicron. The collimated mono-energetic beam of electrons is directed towards a single crystal as in Fig. 2.4 (a). The electrons which are produced by the gun are diffracted from the sample surface and create a diffraction pattern on a fluorescent screen. On the fluorescent screen, the 2-D reciprocal crystal structure is obtained. The spot's intensity can be recorded by a CCD camera.

The result of LEED and LEED-I(V) can be discussed qualitatively and quantitatively if the diffraction patterns are saved. Qualitatively because the pattern gives the symmetry of the substrate and films. Quantitatively, when in LEED-I(V) intensity of the diffracted spots is recorded vs. beam energy. LEED-I(V) curves of the (00)-spot were measured to determine the vertical interlayer space by a simple kinematical calculation.

In LEED, the employed energy ranges from 5 to 600 eV. The result depends on the electron wavelength. The wavelength λ_e is calculated in the following:

$$\lambda_e = \frac{h}{\sqrt{2m_e v}} \approx \sqrt{\frac{150\,\mathrm{eV}}{\mathrm{E}_{kin}}}(\text{Å}) \tag{2.1}$$

where h is Planck's constant, m_e the electron rest mass, v the velocity, and E_{kin} the kinetic energy. The wavelengths of 5 and 600 eV are 5.4 and 0.5 Å, respectively.

The corresponding wave vector, k_e is:

$$k_e = \frac{2\pi}{\lambda_e} = \frac{2\pi}{h} m_e v \tag{2.2}$$

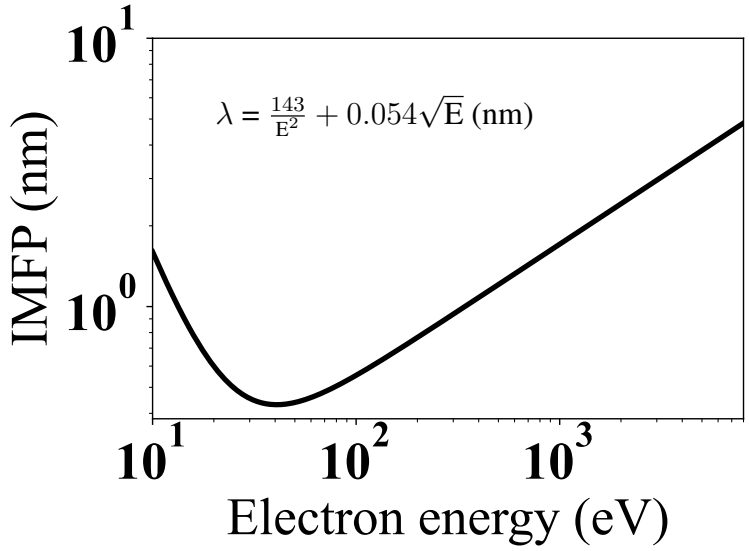

Figure 2.3: An empirical relation of the inelastic mean free path (IMFP) as a function of electron energy. From [38].

In general, LEED does not have element specificity, and it does not give information about the bulk structure. The interference patterns observed in LEED can help to determine the crystal structure. In a LEED experiment, the inelastic mean free path (IMFP) is very low (5 to 10 Å), as it is shown in Fig. 2.3, therefore the LEED is surface-sensitive. LEED can be used to study the surface structure of the substrate and thin films [33].

In a LEED pattern, the surface (i.e., in-plane) reciprocal lattice vectors define

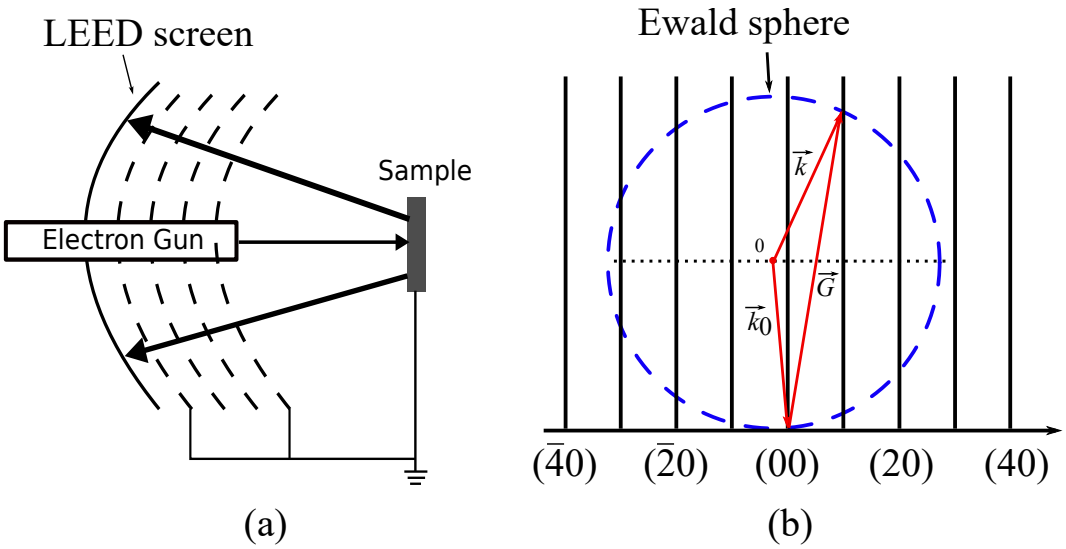

Figure 2.4: Sketch views of LEED optics and Ewald sphere construction in (a) and (b), respectively.

the crystal symmetry, as depicted in Fig. 2.4 (b). $\vec{k_0}$ is the incident wave vector, $\vec{k}$ the scattered wave vector, and $\vec{G}$ a lattice vector the in-plane component of which corresponds to an in-plane reciprocal lattice vector. Only the conservation of the parallel component of the incident, scattered, and reciprocal lattice wave vectors are concerned [32]. The relation between them gives

$$\vec{G} = \vec{k} - \vec{k_0} \tag{2.3}$$

In the diffraction case, only elastic scattering is considered; therefore, the energy is conserved such that $|\vec{k}| = |\vec{k_0}|$. As an example, Fig. 2.5 (a), (b) display the real space and reciprocal diffraction pattern of a c(2×2) superstructure on an fcc(100) substrate. Crystal lattice vectors are determined by a Wood notation such that a_1, a_2 and b_1, b_2 are lattice vectors of substrate and adsorbate layer in real space, respectively. a_1^*, a_2^* and b_1^*, b_2^* are the reciprocal lattice vectors of the substrate and adsorbate layer, respectively.

In LEED-I(V), the energy dependence of the diffracted electron intensity along one or several truncation rods is measured. For the Ewald-sphere construction, the surface sensitiviy is reflected by using rods instead of reciprocal lattice points, as shown in Fig. 2.4 (b) [39]. The Bragg condition and the de Broglie wavelength

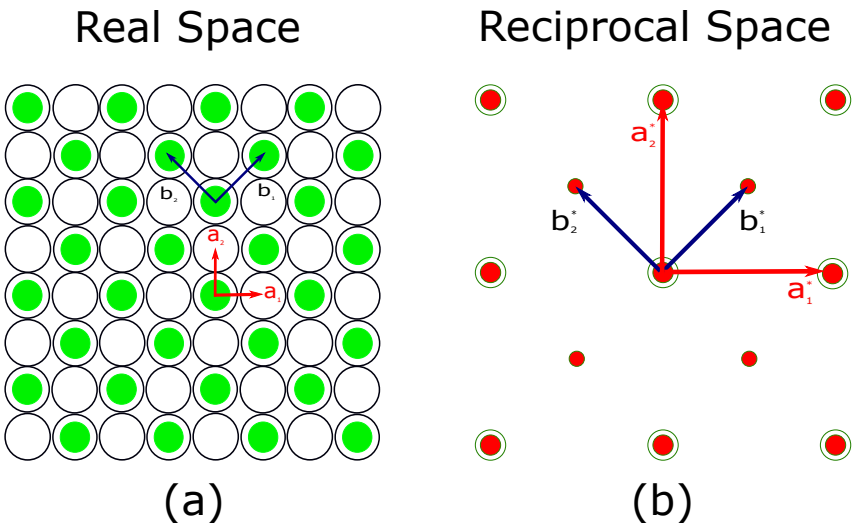

Figure 2.5: A c(2×2) superstructure on the fcc(100) surface in (a) real and (b) reciprocal space. a_1, a_2 and b_1, b_2 are surface lattice vectors of the substrate and the adsorbate layer, respectively. And a_1^*, a_2^* and b_1^*, b_2^* are the reciprocal lattice vectors of substrate and adsorbate layer, respectively.

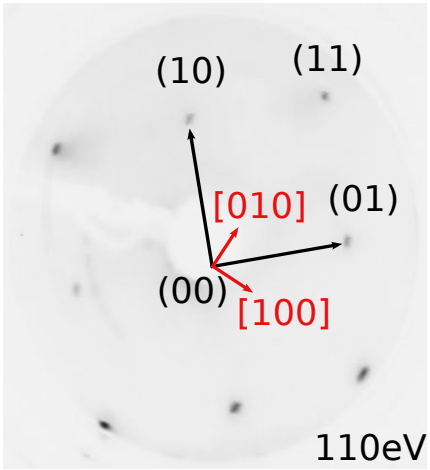

Figure 2.6: A LEED pattern of the clean Cu(001) substrate at 110 eV. The bulk crystallographic directions are indicated by red arrows.

relation give equation (2.4).

$$2d\sin\theta = n\lambda = n\frac{h}{p} = n\frac{h}{\sqrt{2m_e(\mathrm{E_n} - \mathrm{V_0})}} \tag{2.4}$$

By rewriting equation (2.4), we have

$$\mathrm{E_n} = \frac{h^2\mathrm{n}^2}{8m_e\sin^2\theta d^2} + \mathrm{V_0} \tag{2.5}$$

$\mathrm{E_n}$, h, m_e, and θ represent energy, Planck's constant, electron mass, and diffrac-

tion angle relative to the sample surface, respectively. The inner potential, V_0 is the height of the surface potential barrier at the crystal/vacuum interface. It consists of an exchange correlation and a dipole contribution. The exchange correlation is a bulk term, and it is isotropic. However, the dipole term is surface-dependent and varies only by tenths of a volt between different planes of the same crystal [40]. By linear regression, d is obtained from a plot of E_n vs n^2, as demonstrated in Fig. 2.7 (b).

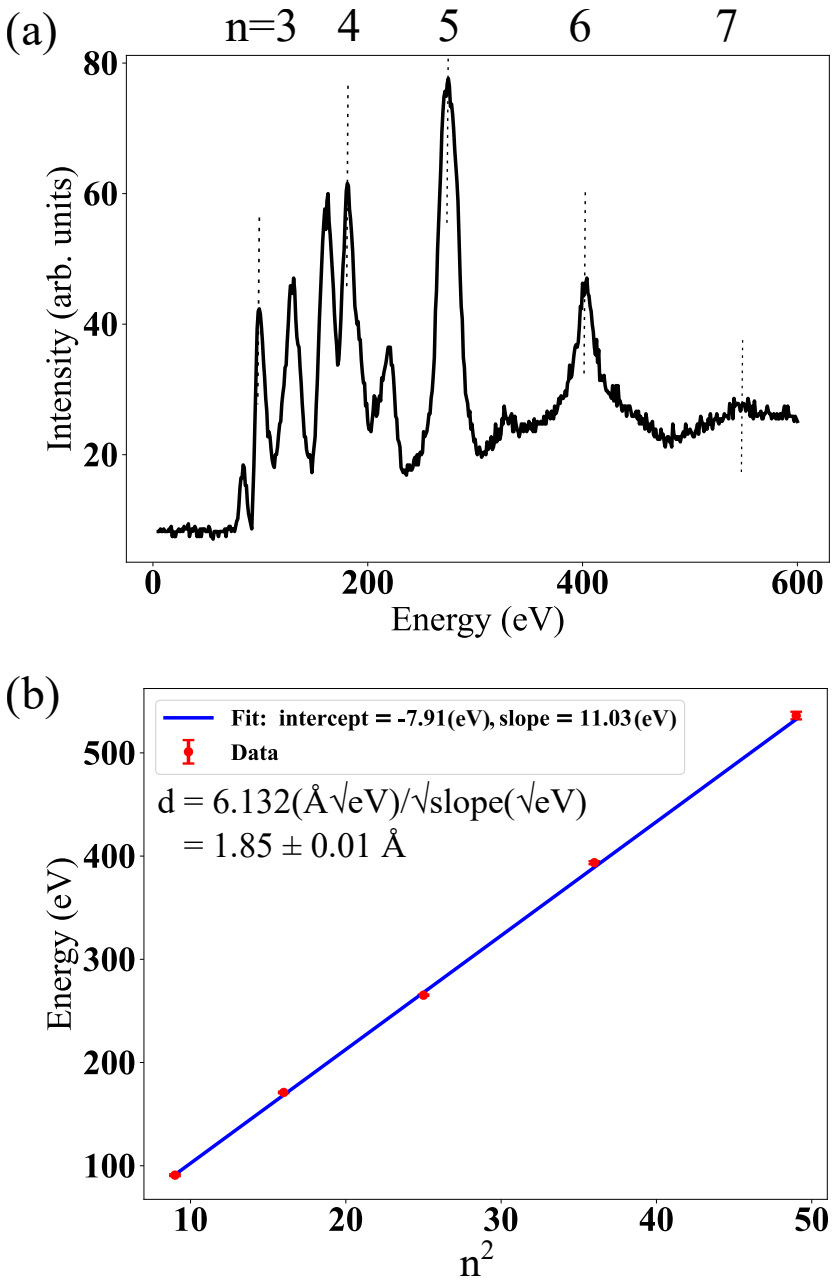

Figure 2.7: (a) LEED-I(V) of the (00)-spot intensity recorded for Cu(001). (b) Kinematic approach for vertical layer distance calculation of Cu(001).

In LEED-I(V), the average interlayer distance is determined by the Bragg maxima for each energy (E_n) position [41]. The LEED-I(V) is obtained by scanning the energy of the electrons from 5 to 600 eV and recording the intensity of the (00) or any other spot by a charge-coupled device (CCD) camera (EHD) as in Fig. 2.7 (a).

2.2.2 Medium-Energy Electron Diffraction

Medium-energy electron diffraction (MEED) is a surface analysis method that can give information about the films' growth mode. MEED is working differently from LEED. The electron source is an electron gun which is in the range of 1 to 5 keV. The electrons from this electron gun hit the sample with a grazing angle ($< 5°$) and then create a diffraction structure on the screen as depicted in Fig. 2.8. MEED is very surface sensitive because of the grazing angles of incidence. MEED needs a very high flatness of the surface. By MEED, the (00) or any other spot is displayed on the screen, and this spot intensity is monitored by a CCD camera. While a film grows in monolayer levels, the intensity of the spot will change. This intensity can be seen as periodic changes if the growth is layer-by-layer. From this periodic oscillation, the film thickness can be counted. Each oscillation is equivalent to 1 ML. If the growth is not layer-by-layer, there will be no oscillation. The (00)-spot intensity increases when the 1^{st} ML is completed and then decreases when the 2^{nd} ML is completed, the intensity increases again, and so on.

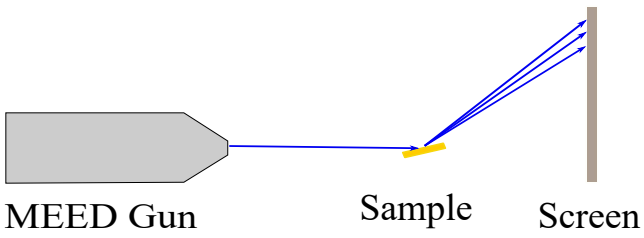

Figure 2.8: Sketch view of the MEED process. The primary electron beam is incident under a grazing angle onto the sample surface.

In this work, the set-up to measure MEED consists of an electron gun and a phosphor-coated view port. A CCD camera was used for recording. The I(t) (MEED (00)-spot intensity) was recorded by using the EE2010 software. MEED

was employed to determine the growth rate for Au, Mn, Co, Fe, Mn_xAu_{1-x} on single crystals.

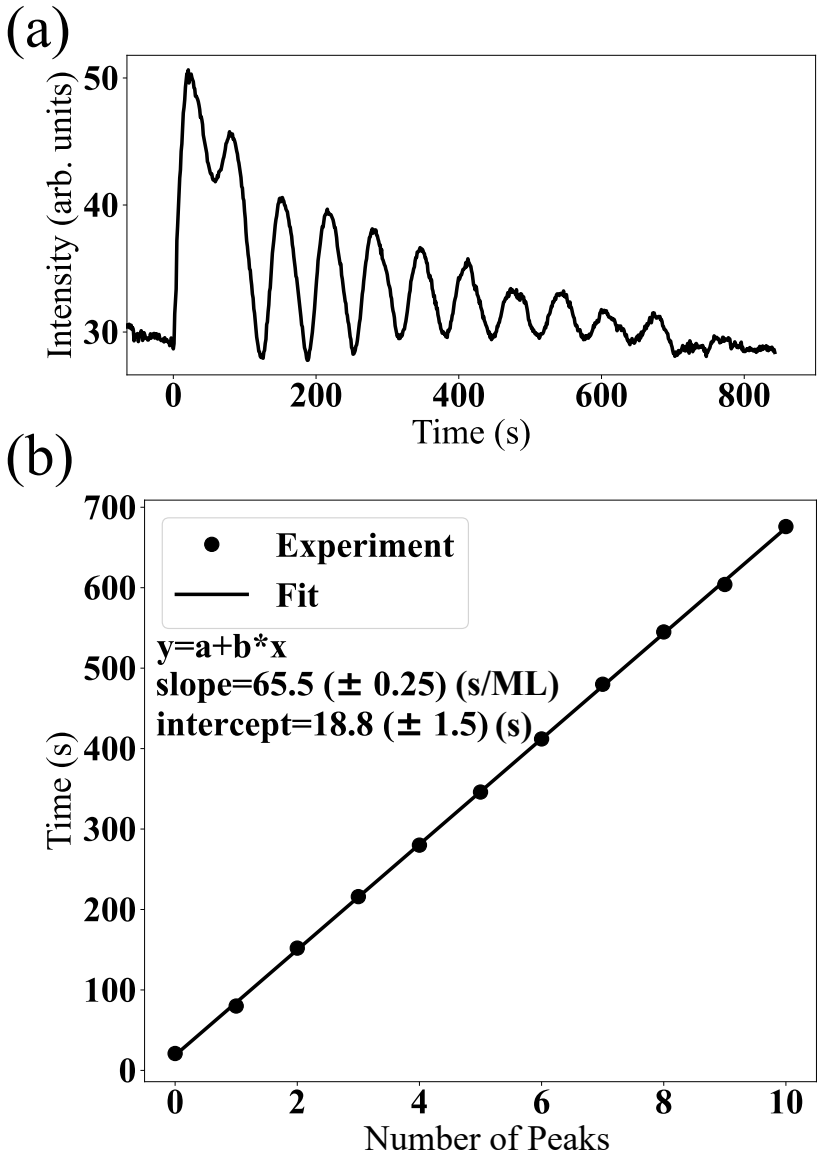

Figure 2.9: (a) The MEED oscillations of Co (11 ML) on Cu(001). (b) The linear fitting of maximum peak numbers vs. time for defining the growth rate.

For defining the growth rate of Mn, first, Co needs to be grown on Cu(001), then Mn is grown on that. The Ag(001) single crystal was also selected as a substrate for the growth of Fe and Mn_xAu_{1-x}. While Mn_xAu_{1-x} oscillates and displays LEED patterns on Ag(001). Fe has very low lattice misfit on Ag(001) (around 0.8%) and does not show MEED oscillations but clear LEED patterns. In Fig. 2.9, the MEED oscillations during the growth of 11 ML of Co on Cu(001) are presented, and the

growth rate was calculated and is shown in Fig. 2.9 (b).

2.2.3 Auger Electron Spectroscopy

Auger electron spectroscopy (AES) is one of the analyzing methods that is being used as material chemical composition investigation for a quantitative analysis of the sample [33]. It can be used to calculate the amount of film or the atomic ratio of an alloy. And the cleanliness of a substrate can be confirmed.

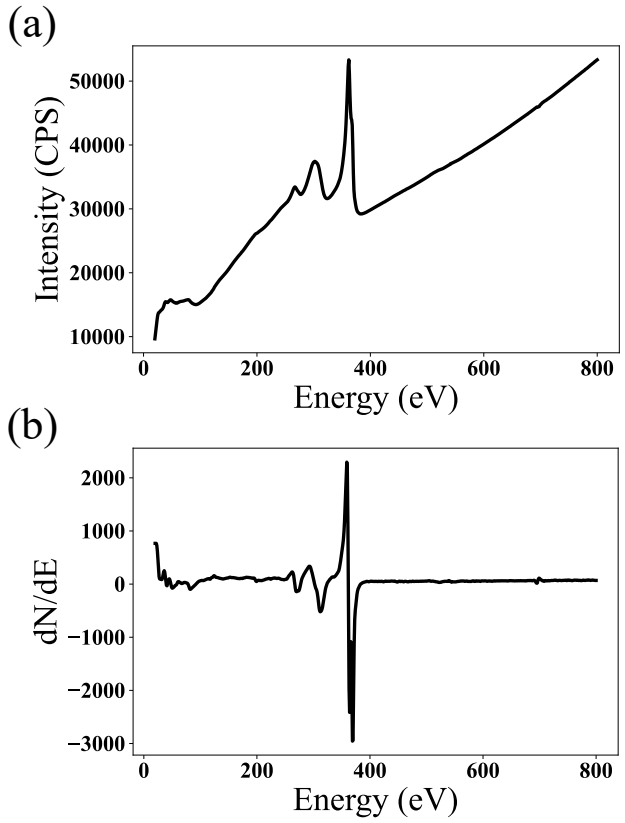

Figure 2.10: The AES spectrum from clean Ag(001) single crystal by PHI-Auger. (a) Auger electron intensity, (b) numerical derivative of (a).

In this work, PHI-Auger (10-155A) and LEED optics (Omicron) were used for AES. Initially, the LEED optics was used for AES. The derivative of the energy distribution is observed as in (d/dE)N(E). The LEED electron gun and LEED optics were used as retarding field analyzer (RFA), and the fluorescent screen was used to detect the electrons as a detector. The Lock-In Amplifier was used to apply an oscillation to the detection energy to increase the signal-to-noise ratio, and by using 2F mode, the 2^{nd} derivative of the signal was obtained. In the PHI-Auger, the

derivative of the signal is obtained numerically. In Fig. 2.10 (a) and (b), we see the AES spectra as intensity and numerical derivative, which is obtained from Fig. 2.10 (a), respectively, spectra are obtained via the PHI-Auger. In the derivative Auger spectrum, the background is suppressed. The derivative AES peak intensity can be used for quantitative calculation.

The PHI-Auger was needed because by using the LEED optics, the resolution was not sufficient for the lower energy range ($< 120\,\text{eV}$). Therefore, we decided to mount the PHI-Auger in this chamber. To have Auger with LEED together, another CF-100 port was added in the same height level as LEED and a cross of the LEED system, such that it can be used as a source of electrons for MEED.

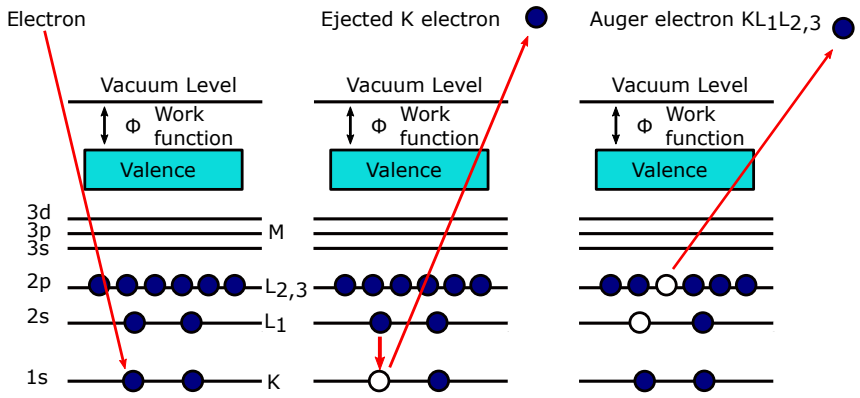

Figure 2.11: Three steps of the Auger electron process.

Auger electrons were investigated by Pierre Victor Auger in 1922. Therefore this technique was named after him. The AES technique was developed in the late 1960s. The Auger electron phenomena occur in three steps, as it is displayed in Fig. 2.11. For instance, core electrons (K) are ejected either by high-energy electrons or by X-rays (in this work 3 kV electrons are used to obtain Auger electrons). This core vacancy is filled by an outer shell electron (for example, L_1). This electron either releases X-ray photons or excites another electron (for example L_2), which is emitted as an Auger electron (KLL). These excited electrons are called Auger electrons with an energy $E_{KL_1L_2}$. The energy of Auger electrons is determined by the three energy levels concerned, where

$$E_{KL_1L_2} = E_K - E_{L_1} - E_{L_2} \tag{2.6}$$

The observed Auger signal I_A from an element A is determined by the expression [42].

$$I_A = I_0 \cdot N_A \cdot T(E_A) \cdot \sigma(E_0) \cdot (1 + r(E_c, E_0)) \cdot \gamma \cdot \lambda(E_A) \cdot \sin\phi \cdot \cos\theta \tag{2.7}$$

where I_0 = incident beam intensity, E_0 = primary beam energy, E_A = Auger electron energy, E_c= critical ionization potential, N_A = atom density of element A, $T(E_A)$ = detection efficiency of the spectrometer and detector, $\sigma(E_0)$ = ionization cross-section for the relevant shell of A, $r(E_c, E_0)$ = fractional contribution to total ionization by the flux of back-scattered electrons, γ = probability of ionization giving rise to an Auger electron (including the effect of Coster-Kronig transitions), $\lambda(E_A)$ = inelastic mean free path for electrons of energy E_A, θ = angle of incidence of primary beam, ϕ = effective exit angle of Auger electrons entering the spectrometer.

These electrons are detected and integrated over a large area of the surface. By AES, the quantity of the element on the sample can be determined. The chemical ratio in an alloy and the layer thickness can be determined by the help of AES. From the Auger peak intensity of substrate I_s, and film I_f we can get the thickness of the film t_f:

$$I_f = I_0 \cdot S_f \cdot (1 - \exp(-t_f/\lambda_f)), \tag{2.8a}$$

$$I_s = I_0 \cdot S_s \cdot \exp(-t_f/\lambda_s) \tag{2.8b}$$

where I_f is the film peak intensity, I_0 is primary beam intensity, S_f the film sensitivity factor, t_f the film thickness, λ_f the inelastic mean free path (IMFP) of Auger electrons from the film in the film, I_s the substrate peak intensity, S_s the

substrate sensitivity factor, and λ_s is the IMFP of the substrate Auger electrons in the film. The peak intensities I_f and I_s are directly obtained from the Auger spectrum, and the thin film thickness t_f is obtained by MEED. In this study, the sensitivity factors S_f and S_s are not obtained separately. The ratio of S_s/S_f is calculated as in equation (2.9).

$$\frac{S_s}{S_f} = \frac{I_f}{I_s} \cdot \frac{1 - \exp(-t_f/\lambda_f)}{\exp(-t_f/\lambda_s)} \tag{2.9}$$

As we already mentioned, we can calculate the alloy ratio by AES. Let A and B be the elements in an alloy film on the substrate, and the ratio of A/B is needed. The ratio of A/B is calculated as:

$$I_A = I_0 \cdot S_A \cdot x \cdot (1 - \exp(-t_{AB}/\lambda_A)), \tag{2.10a}$$

$$I_B = I_0 \cdot S_B \cdot (1 - x) \cdot (1 - \exp(-t_{AB}/\lambda_B)) \tag{2.10b}$$

where I_A and I_B are Auger intensities of A and B, respectively. S_A and S_B are the sensitivity factors of film of A and B, respectively. t_{AB} is the alloy film thickness. x and $(1 - x)$ are the fractions of A and B, respectively, in an AB alloy film. λ_A and λ_B are the IMFP of the Auger electrons of A and B, respectively, in the AB alloy film.

The fractions of the materials are calculated as follows:

$$\frac{I_A}{I_B} = \frac{S_A}{S_B} \cdot \frac{x}{1 - x} \cdot \frac{1 - \exp(-t_{AB}/\lambda_A)}{1 - \exp(-t_{AB}/\lambda_B)} \tag{2.11}$$

Equation 2.11 gives the Auger intensity ratio of A and B in the AB ultra-thin alloy film on the single-crystal substrate. If the film thickness is known or if λ_A and λ_B are equal (or similar or very close, then the influence of t_{AB} is small), Eq. 2.11 can be used to determine x.

2.2.4 Scanning Tunneling Microscopy

Scanning tunneling microscopy (STM) provides a direct observation and manipulation of the atomic structure of surfaces in the nm range. The first STM was built by Binning and Rohrer in 1982 [43], for which they received the Nobel prize in 1986. Since their discovery, it has become the most frequently used method in surface science studies. STM has been used to explore the surface with the atomic resolution for a long time. Later on, spin-polarized scanning tunneling microscopy (SP-STM) was developed for the investigation of magnetic structures on the atomic scale too [44]. In general, W tips are used, which are electrochemically prepared. In an SP-STM measurement, FM and AFM tips are being used. For FM tips, Fe, Ni, Co, or Fe-coated W tips are being used. For AFM tips, MnNi, MnPt, Cr, and Cr-coated or Mn-coated W tips are being used [45].

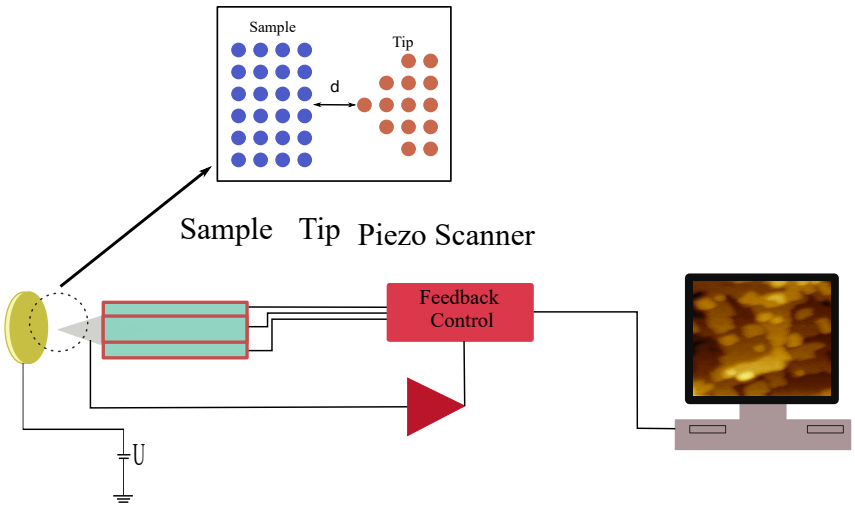

Figure 2.12: A sketch for the basic principle of an STM setup.

The STM consists of a sharp or ring metal tip. In the sharp tip case, it has a single apex. It is depicted in Fig. 2.12. A piezo-scanner can move it in three dimensions to scan the surface and adjust the tip-sample distance. Tunneling is a quantum effect that occurs only when the tip is close enough (in the range of a few Å) to the sample. Then electrons can tunnel through the vacuum barrier from the tip into the sample or vice versa. In the case of applying a positive bias to the sample, tunneling happens from tip to sample, as shown in Fig. 2.13. In the case of

negative bias, tunneling happens from sample to tip. The data collection was done by a LabVIEW program. The STM can be employed in air and vacuum. However, for a clean surface or to prevent contamination, the STM generally is operated in UHV.

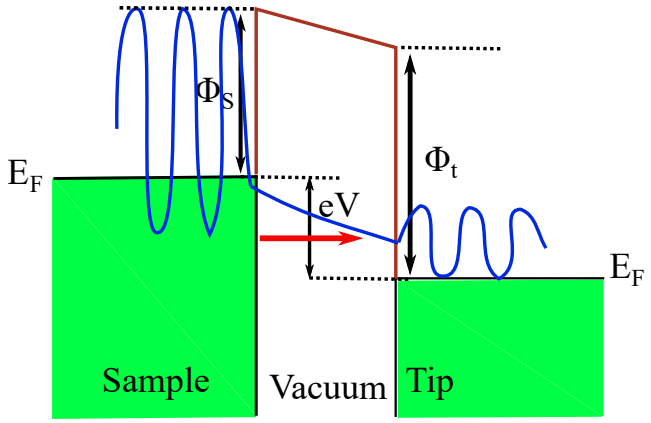

Figure 2.13: The sketch view of negative bias applied to the sample, tunneling occurs from sample to tip.

As it is already mentioned above, the STM is based on the quantum tunneling effect. An electron can move through a barrier as a quantum effect in that they behave as a wave-like feature. Because classically, an electron should not move through a barrier or wall. The tunneling through a vacuum barrier between two metal electrodes was first reported by Young et al. [46].

In this work, an Omicron STM1 was used for surface structure examination in UHV, with a base pressure around 2×10^{-10} mbar at RT [47]. The STM was controlled by a Labview program. The samples were scanned by an Fe-ring tip which is mounted vertically. The Fe-ring tip was prepared as described by Wu et al. [48]. The samples were prepared in the preparation chamber, and without breaking the vacuum, the samples were transferred to the STM chamber by a transfer rod. There is a valve between the STM and the preparation chambers to prevent high pressure in the STM chamber during sample preparation. The STM chamber vacuum is sustained by an ion getter pump and monitored by a cold cathode. The samples and tips can be stored in a carousel in the STM. In Fig. 2.14, we show the STM topography of clean Cu(001) and a related line scan of it.

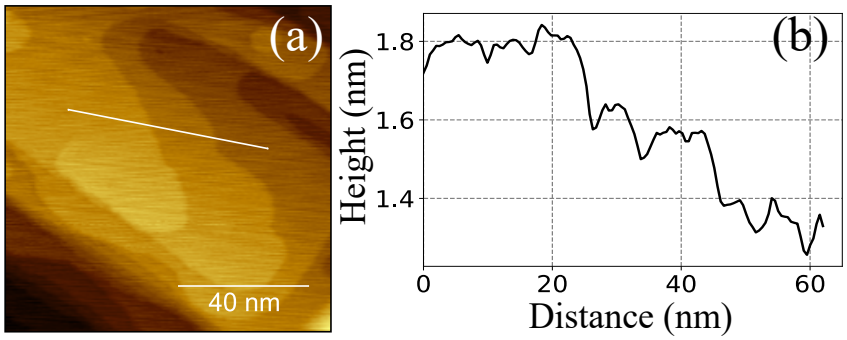

Figure 2.14: (a) STM topography image of Cu(001). STM feedback parameter for (a) is 0.7 nA$\times$1 V, (b) is a line scan of (a) along the white line.

2.3 Magnetic Property Analysis Methods

In this part, methods to analyze the magnetic properties of the prepared samples will be discussed. L-MOKE is being used to investigate the magnetic properties of the films.

2.3.1 Magneto-Optic Kerr Effect

By magneto-optic Kerr effect (MOKE), the magnetic phenomena of the samples were studied. The Kerr effect was discovered after the Faraday effect. Faraday discovered the latter when he measured the polarization of light transmitted through a magnetic film. Faraday discovered that when a linearly polarized beam of light is propagated through a magnetized medium, the plane of polarization and the ellipticity of light change. This effect results from the two circularly polarized components having a different propagation velocities [49]. This difference in dielectric constants of left- and right-circularly polarized light accounts for the Faraday rotation [50]. Later, Kerr discovered the same phenomenon on reflected light in a polished iron bar. The polarization of polarized light changes during reflection from a magnetic medium [51]. This phenomenon was called the magneto-optic Kerr effect [52]. The photon energies of the laser are used for MOKE measurement are typically of the order of a few eV involving the excitations of electrons from occupied to unoccupied valence states in the absorbing medium [53].

The complex Kerr rotation ϕ_s and ϕ_p for s (perpendicular)- and p (parallel)-

polarized lights are given by:

$$\phi_s = \phi'_s + i\phi''_s s = \frac{r_{ps}}{r_{ss}} \tag{2.12}$$

and

$$\phi_p = \phi'_p + i\phi''_p = \frac{r_{sp}}{r_{pp}} \tag{2.13}$$

where r_{ss}, r_{sp}, r_{ps}, r_{pp} are Fresnel reflection coefficients.

Magneto optics is explained by either macroscopic or microscopic quantum theory. Macroscopically, magneto-optic effects arise from the antisymmetric, off-diagonal elements in the dielectric tensor. Microscopically, the coupling between the electrical field of the light and the electron spin within a magnetic medium occurs through the spin-orbit interaction [54]. MOKE is one of the most common methods to study the static or dynamic magnetic properties of magnetic thin films. MOKE is a non-destructive method that is performed by a shining laser on the material and detecting the reflected light by a diode. The polarization of the light changes by the magnetic property of the magnetic film. MOKE is a surface-sensitive technique whose light penetration depth is around 20 nm. This simple technique got popular after 1985, when the first experiment has been done on Fe on Au(100) [55].

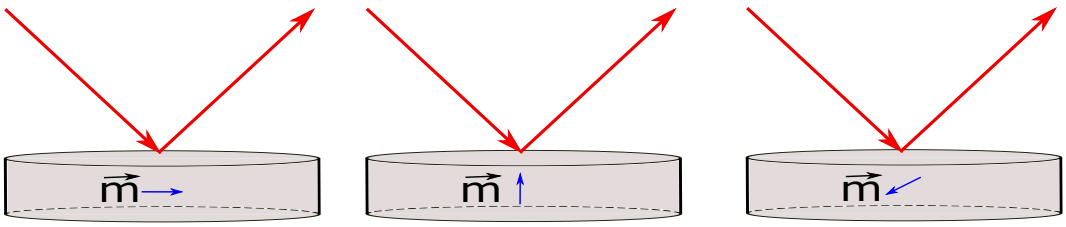

Figure 2.15: Longitudinal, polar, transversal MOKE geometry from left to right.

MOKE has an essential effect on the study of magnetic ultra-thin films due to its local probing simplicity. In the MOKE experiment, the longitudinal and polar MOKE are investigated by a rotation of the plane of polarization of linearly polarized incident light upon reflection from the surface of a ferromagnetic material [54]. The rotation in the light is related to the magnetic property of the thin film. It basically detects light polarization changes when light interacts with the films in an

applied field. There are three geometrical setups of MOKE, which are longitudinal (L-MOKE), polar (P-MOKE), and transverse (T-MOKE), as depicted in Fig. 2.15. P-MOKE involves the magnetization perpendicular to the surface of a sample; T-MOKE measures the magnetization perpendicular to the applied magnetic field (in T-MOKE, the magnetization is parallel to the surface and perpendicular to the plane of incidence as you can see in Fig. 2.15). L-MOKE involves the magnetization of the sample in the direction of the plane of incidence and the applied magnetic field. The polar and longitudinal Kerr effects are linear in Q (Voigt vector [54]) and yield a complex rotation ϕ of the polarization of the light. The polar signal is typically an order of magnitude greater than the longitudinal signal due to optical factors. The transverse Kerr effect requires a second-order expansion in Q and manifests itself by a small reflectivity change for p-polarized incident light [50].

In this work, a MOKE system and Labview program are employed to measure the magnetization of a sample versus the applied magnetic field. Hysteresis loops were taken, and the coercivity and exchange bias could be measured. The experimental setup is displayed in Fig. 2.16. It includes a diode laser source of monochromatic light (at 632 nm), two polarizers, lenses, and an electro-magnet powered by a Kepco bipolar power supply to create our external magnetic field. The polarized laser light is incident on the sample in the magnetic field, as shown in Fig. 2.16. The reflected light is detected by a Thorlabs silicon photodiode. A second analyzer (is also a polarizer) is aligned close to perpendicular to the first one. It detects any changes in polarization in the reflected beam. In Fig. 2.17, the setup we used to measure the hysteresis loops of Co/Mn_xAu_{1-x} on Cu(001) bilayer samples is shown. In this chamber, we could cool the sample down to around 100 K and apply a higher field (around 400 mT).

2.3.2 XAS and XRMR Measurements

We employed the X-ray resonant magnetic reflectometry (XRMR), and X-ray absorption spectroscopy (XAS) for the investigation of element-resolved magnetic

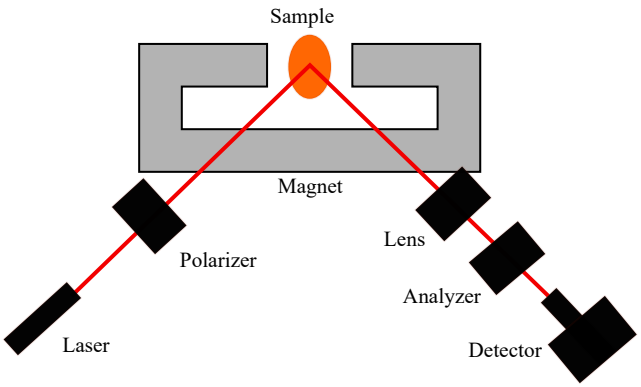

Figure 2.16: Sketch of the L-MOKE setup in the preparation chamber.

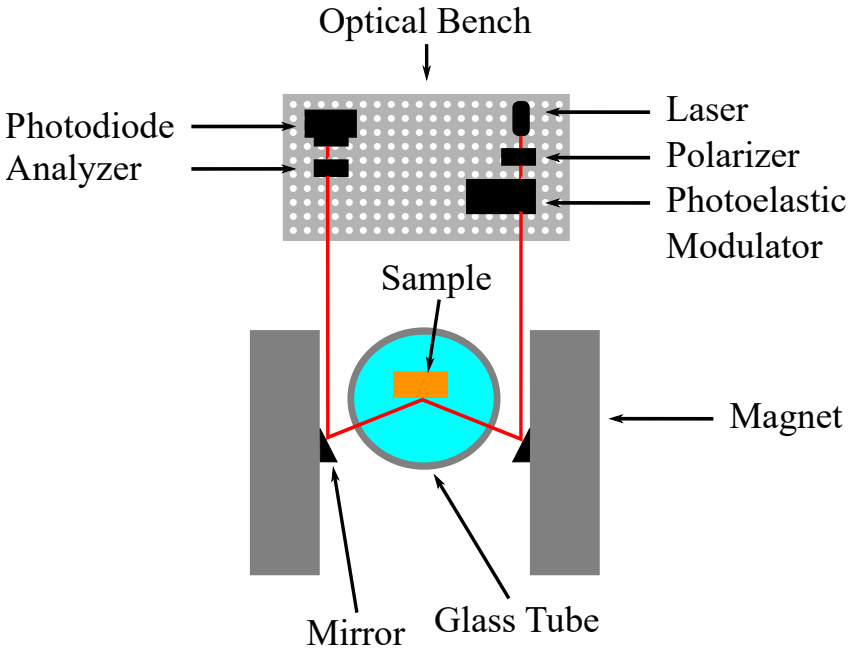

Figure 2.17: Sketch of the MOKE setup in another chamber used for Co/Mn_xAu_{1-x} on Cu(001) bilayer samples' measurement.

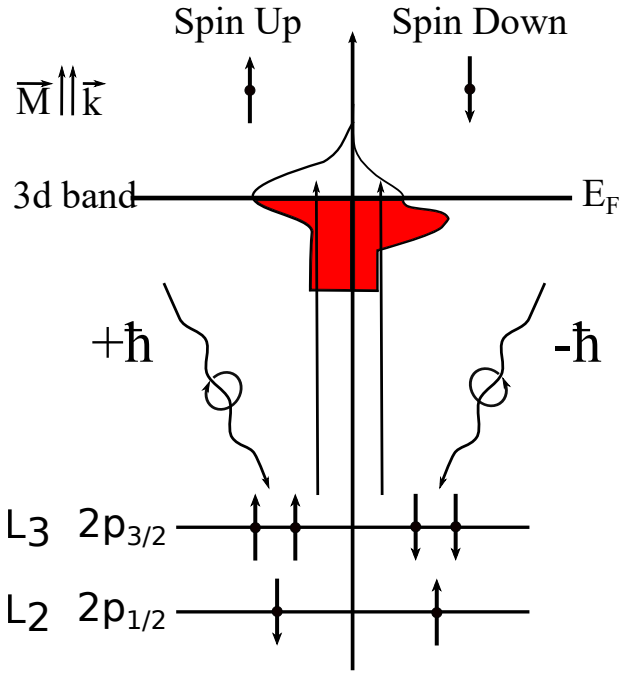

Figure 2.18: The illustration of XMCD effect for 3d transition metals. The spin-polarized electrons are excited by right or left circularly polarized light for L-edge absorption. Reprinted with permission from [56] by Elsevier and Copyright Clearance Center.

properties of Co and Mn (soft X-ray regime) at the PM2-VEKMAG end station at BESSY II, Helmholtz-Zentrum Berlin (HZB) [57].

X-ray magnetic circular dichroism (XMCD) gives the magnetic properties of samples. XMCD is a magneto-optical effect, like MOKE, but XMCD is an element- and shell-selective method. XMCD results because spin-up and spin-down electrons are excited more by left and right circularly polarized light, respectively. This difference gives information about the spin polarization of the empty states and, thus, the magnetic state of the absorber. By using sum rules, spin and orbital magnetic moments can be calculated from XMCD absorption spectra around an absorption edge [58, 59]. XRMR provides information about the optical, structural, and magnetic element-selective depth profile of the films [60, 61]. In contrast to MOKE, XRMR gives the opportunity to obtain element-selective hysteresis loop. XRMR combines XRR and XMCD that measures the specular reflection for different (parallel or antiparallel) polarization [62]. In XRMR and XRR, besides the absorption, also the dielectric properties of the sample enter and all the diffraction.

The scattering vector q_z is the difference between the incident wave vector k_i and scattered wave vector k_f as shown in Fig. 2.19. The magnitude of q_z is defined

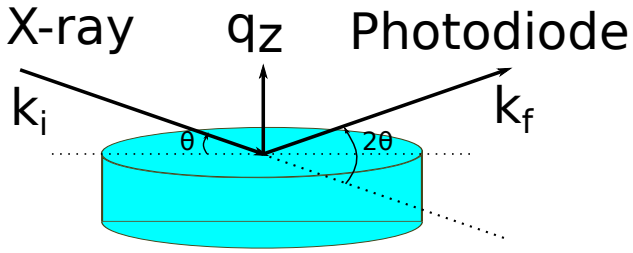

Figure 2.19: The illustration of the XRR geometry. The polarized light hits the sample with angle θ and is detected by a photodiode at 2θ.

$$q_z = |k_i - k_f| = \frac{4\pi}{\lambda} sin(\theta) \tag{2.14}$$

where k_i and k_f are the incident and reflected light wave vectors, respectively, and θ is the angle between the incident light and the sample surface. We employed the XRR as illustrated in Fig. 2.19. The soft X rays have a very high absorption, especially at the absorption edge, compared to hard X rays. The penetration depth of soft X rays is around 1000 nm, which depends on the reflection angle and incident photon energy. Moreover, in the θ-2θ measurement, the Bragg peaks' positions depend on the incident photon energy [63].

We measured the XMCD; instead of changing the helicity of light, the direction of magnetization is changed. Reversing the direction of magnetization or the helicity of light are equivalent due to time reversal [64, 65]. We measured the XAS and XRR of $L_{2,3}$ edges of 3d Co and Mn (soft X-ray regime). XAS is measured by the total electron yield (TEY), which is proportional to the absorption cross section times the photon energy [53]. The TEY consists of photoelectrons, Auger electrons, and secondary electrons [53]. These emitted electrons can be measured by a picoamperemeter. The photoabsorption coefficient μ is proportional to the absorption cross section σ_{abs}, which is equal to the transition probability per unit time P_{tp} and the photon flux I_{photon} [65].

$$\mu \propto \sigma_{abs} = P_{tp}/I_{photon} \tag{2.15}$$

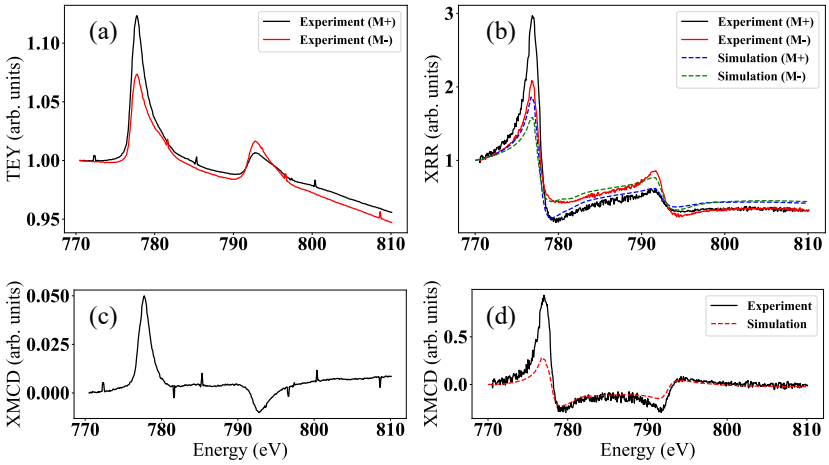

Figure 2.20: (a) XAS and (c) XMCD of Au(14)/Mn(6)/Co(5) on Cu(001). (b) and (d) are the XRR and XMCD, respectively, with experiment and simulation by UDKM1DSIM. The experimental XRR data were obtained at θ=15.5°. The simulation parameters are Au(20)/Mn(6)/Co(5) on Cu(001), the optical constants are from another sample which was studied by Ivar Kumberg for Mn and Co around the $L_{2,3}$ edges [66]. The numbers in brackets are the film thicknesses in ML.

The experimental data, as shown in Fig. 2.20 are normalized to the pre-edge for XAS and XRMR. Then we obtain XMCD by subtracting (2.16) both XRMR or XAS intensity for the helicity of the X-ray parallel (M^+) or antiparallel (M^-) with the applied magnetic field as shown in Fig. 2.20 and described as

$$XMCD = M^+ - M^- \tag{2.16}$$

As shown in Fig. 2.20, we simulate our experimental XRR data by UDKM1DSIM [67]. UDKM1DSIM is a software toolbox to simulate X-ray reflectivity of multilayered films from the lattice constants, the film thicknesses, and the optical constants of all constituents. We simulate the XRMR results by using ReMagX ([68, 62, 69]), which are going to be shown and discussed in detail in Chapter 4.

CHAPTER 3

Theoretical Background

In this thesis, we studied the magnetic properties of AFM-FM bilayer films by MOKE. One can obtain the exchange-bias field and the coercivity from hysteresis loops by MOKE measurement. Therefore, in this part, we will explain the exchange bias effect and some models which describe it.

3.1 Exchange Bias

Exchange bias (EB) is one of the phenomena that reveal the AFM/FM exchange coupling. Exchange bias occurs when a material with FM and AFM interface is field-cooled through the Néel temperature (T_N), which is lower than T_C of the FM layer. When the temperature is above T_N, the AFM spins are disordered. When the sample is below T_N, the AFM spins are ordered. The ordered spins of AFM and FM will have an exchange coupling that leads to the shift of the hysteresis loop, as it is shown in Fig. 3.2. An enhancement of the coercivity in a field-cooled hysteresis study compared to the corresponding zero field-cooled (ZFC) case can be seen. The exchange bias sometimes reduces with an increasing number of loop cycles in a cyclic hysteresis loop study called the training effect [9]. The exchange anisotropy is the interaction between FM and AFM, FM and FIM (ferrimagnetic) [70], or AFM and FIM [71, 72]. In Fig. 3.1, we show the ordering of FM and FIM spins ordering aligned parallel in a magnetic domain below T_C. AFM spins are aligned antiparallel in magnetic domains below T_N. Paramagnetic spins are randomly oriented above T_C or T_N [73]. Exchange bias was first discovered by Meiklejohn and Bean [74]. They found exchange bias in nanoparticles consisting of FM Co and AFM CoO (T_N 291 K) materials after field-cooling the sample from 300 to 77 K in a constant saturating magnetic field.

Exchange bias occurs due to magnetic coupling between a ferromagnetic and

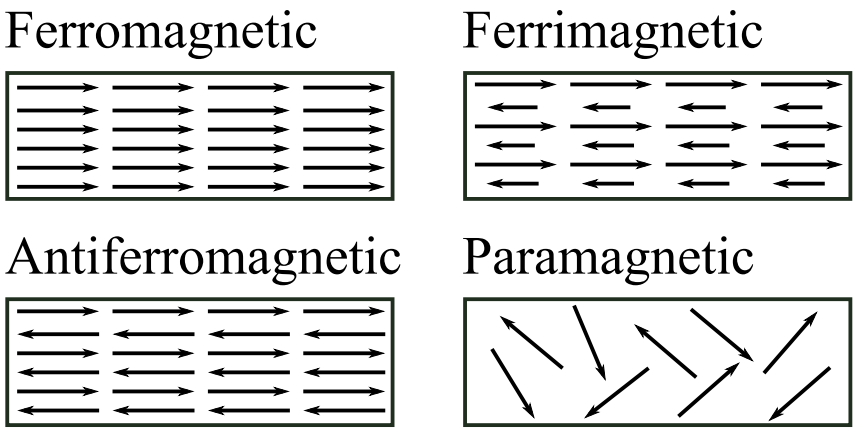

Figure 3.1: The illustration of the ordering of spins in ferromagnetic, antiferromagnetic, ferrimagnetic, and paramagnetic samples.

an antiferromagnetic material after field cooling. The hysteresis loop of the FM is not centered around zero magnetic field anymore but shifted by a certain field, the exchange-bias field [75]. In an exchange-bias system, the FM is pinned by the AFM. Therefore, when the applied field is not bigger than H_{C1} (right coercive field) or H_{C2} (left coercive field), as shown in Fig. 3.2, the FM will not reverse. This exchange bias property is being used in spin valves and magnetic tunnel junctions.

The magnetic properties of the films were studied by obtaining hysteresis loops via MOKE. From a hysteresis loop, we can obtain exchange bias and the coercive field (H_C) of the films as shown in Fig. 3.2. In Fig. 3.2, we display a schematic diagram of the spin configuration for an FM-AFM bilayer hysteresis loop. When a sample (FM-AFM bilayer) heats above T_N and below T_C, the FM spins will align with the applied field direction, but the AFM spins will stay at random. When a sample (FM-AFM bilayer) field cooled below T_N, the FM spins will align with the applied field direction, and the AFM spin next to FM the FM align in same direction of FM spin, and next next neighbor AFM spins will align oppositely so there will be no net magnetization. When the applied field is reversed, the FM spins are also rotated, but not AFM spins. The FM spins' anisotropy is unidirectional. To reverse FM, the applied field needs to be larger enough due to the interface interaction of FM-AFM spins. When the field is reversed to its original direction, the FM spins will rotate with a very small field because of FM-AFM interaction; that is the reason

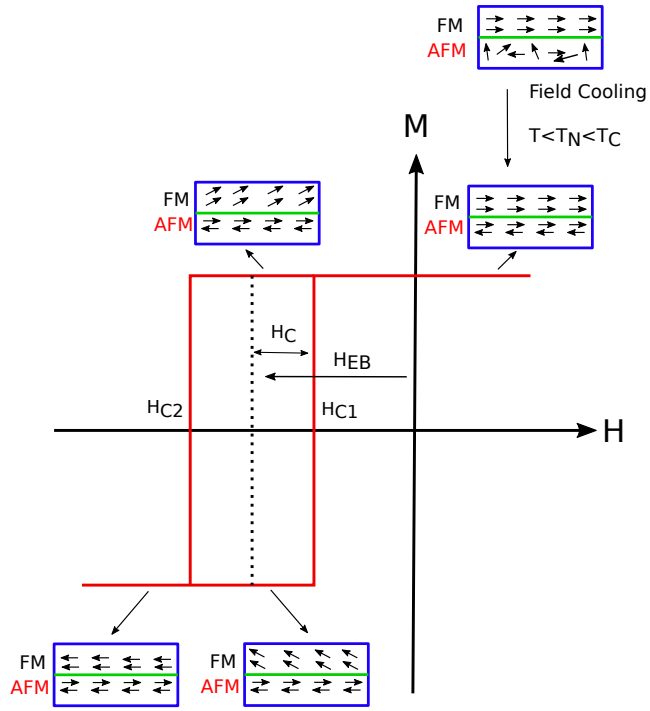

Figure 3.2: FM/AFM bilayer's atomic moments relative orientations are depicted in schematic way for a model explaining the exchange bias effect. In the figure, the coercive field H_C and exchange bias field H_{EB} are defined. This schematic shows the spin alignments for AFM-FM coupling, which does not need to be an accurate rotation. Reprinted with permission from [9] by Elsevier and Copyright Clearance Center.

of the exchange bias [9].

H_{EB} and H_C are values obtained from a hysteresis loop. In the case of an FM hysteresis loop, H_C is the reverse applied magnetic field needed to reduce the magnetization to zero. If H_{C1} and H_{C2} are the values of the applied field at which the magnetization of the sample is zero and also where the magnetization changes its sign during descending and ascending, respectively, [76]. The H_{EB} and H_C can be calculated from a hysteresis loop as

$$H_{EB} = \frac{H_{C1} + H_{C2}}{2}, \tag{3.1a}$$

$$H_C = \frac{H_{C1} - H_{C2}}{2} \tag{3.1b}$$

A significant factor affecting H_{EB} and H_C is the thickness of the magnetic layer in the thin films. H_{EB} typically has a linear dependence on the inverse of the ferro-

magnetic film thickness, t_{FM} [77]. The relation between them is:

$$H_E \sim 1/t_{FM} \tag{3.2}$$

The study of the exchange bias is important because it is assumed that the hysteretic processes are taking place in the AFM material. The exchange bias field is an indication of how much energy ΔE is contained in the spin disorder and the spin interactions at the interface between the AFM and FM layers of the magnetic system and in which direction the exchange bias is anisotropically oriented:

$$\Delta E = M_{FM} t_{FM} H_{EB} \tag{3.3}$$

where M_{FM} and t_{FM} are the saturation magnetization and thickness of the ferromagnet and H_{EB} is the exchange bias magnitude [9]. In Nogués and Schuller's

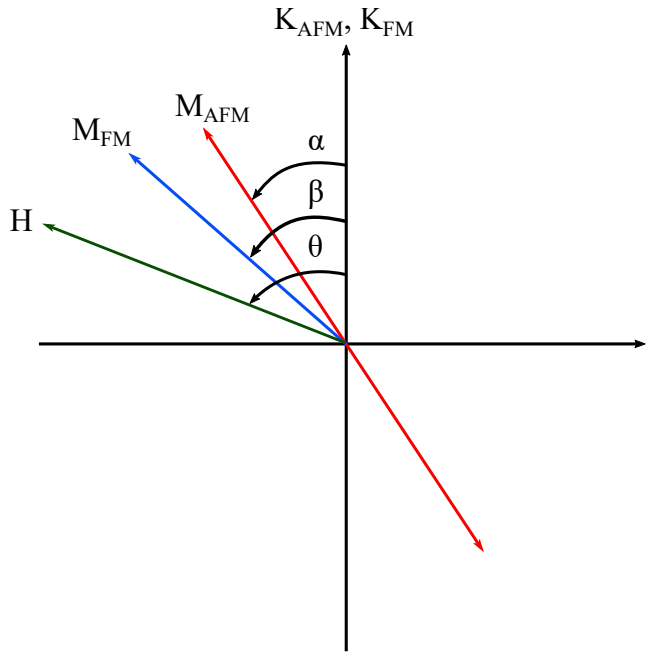

Figure 3.3: A schematic diagram of angles being used in exchange bias [9].

work, for explaining the origin of exchange bias, they defined E (energy per unit

area for exchange bias system) for a coherent rotation of the magnetization as [9]:

$$\begin{aligned} E = &- HM_{FM}t_{FM}\cos(\theta-\beta) + K_{FM}t_{FM}\sin^2(\beta) + K_{AFM}t_{AFM}\sin^2(\alpha) \\ &- J_{INT}\cos(\beta-\alpha) \end{aligned} \tag{3.4}$$

where H is the applied field, M_{FM} the saturation magnetization, t_{FM} the thickness of the FM layer, t_{AFM} the thickness of the AFM layer, K_{FM} the anisotropy of the FM layer and J_{INT} the interface coupling constant. β, α, and θ are the angles between the magnetization and the FM anisotropy axis, the AFM sublattice magnetization (M_{AFM}) and the AFM anisotropy axis, as can be seen in Fig. 3.3. The first term in Eq. (3.4) accounts for the effect of the applied field on the FM layer; the second term is the effect of the FM anisotropy, the third term takes into account the AFM anisotropy, and the last term considers the interface coupling. Although this energy function takes into account the main parameters involved in exchange bias, it assumes the absence of AFM and FM domains, that the AFM and FM anisotropy axes are parallel and ferromagnetic coupling at the interface [9, 72].

In a further simplification, the FM anisotropy is assumed to be negligible for the energy. Then, Eq. (3.4) becomes Eq. (3.5):

$$E = -HM_{FM}t_{FM}\cos(\theta-\beta) + K_{AFM}t_{AFM}\sin^2(\alpha) - J_{INT}\cos(\beta-\alpha) \tag{3.5}$$

When this energy is minimized with respect to α and β, the loop shift is found to be:

$$H_{EB} = \frac{J_{INT}}{M_{FM}t_{FM}} \tag{3.6}$$

The requirement for the exchange anisotropy is shown in Eq. (3.7):

$$K_{AFM}t_{AFM} \geq J_{INT} \tag{3.7}$$

If the interface coupling relation with the AFM anisotropy and the AFM thick-

ness is like in Eq. (3.8):

$$K_{AFM}t_{AFM} << J_{INT}, \tag{3.8}$$

then $\beta \approx \alpha$, as a conclusion of this situation, the AFM and FM spins rotate together. Therefore, there is no exchange bias, i.e., no loop shift.

3.2 Theoretical Models

There is no single model to explain the exchange bias [78, 9]. Here we will explain the ”Meiklejohn–Bean” and ”Malozemoff” models that describe the exchange bias phenomenon.

3.2.1 Meiklejohn–Bean Approach

Because exchange bias was first discovered by Meiklejohn and Bean, we start with their model to describe the EB [74, 72] to explain the reasons behind the shift in the hysteresis loop after field cooling. And, of course, for EB, the interface interaction between FM and AFM is needed. Meiklejohn and Bean explained the exchange bias by a large anisotropy in the AFM, and a weak exchange coupling between FM and AFM [75]. When starting to field-cool from above T_N, where the AFM spins are in a paramagnetic state, the FM spins will be aligned with the field direction. During the field cooling, the spins of the AFM material in contact with the FM will start to align in the same direction as the FM spins, and the nearest-neighbor spins will align oppositely. After finishing the field-cooling, this keeps the FM spins in the field-cooling direction. When the FM-AFM system field-cools to below T_N, the AFM spins will not rotate out of their alignment because of a very high AFM magnetocrystalline anisotropy [79].

In their model, the H_{C1} and H_{C2} can be found from the system energy [75]

$$E = -HMt_f \cos\theta - J\cos\theta + K_f \sin^2\theta \tag{3.9}$$

where H is the applied field, M the saturation magnetization of the ferromagnet,

t_f the thickness of the FM film, J the interlayer exchange coupling between the FM and AFM spins, and K_f a uniaxial anisotropy in the FM layer. θ is the angle between M and K_f. This yields energy extrema at θ = 0 and π directions. Stability of θ = 0 and θ = π are possible if $J + H + K_f > 0$ and $2K_f - J - H > 0$, respectively. From these, the coercive fields for right and left are

$$H_{C1} = -\frac{2K_f + J}{Mt_f}, \tag{3.10a}$$

$$H_{C2} = \frac{2K_f - J}{Mt_f}, \tag{3.10b}$$

Substituting the Eq. 3.10 into Eq. 3.1b, then the exchange bias for this model becomes

$$H_{EB} = \frac{J}{M_F t_F}. \tag{3.11}$$

From Eq. 3.11, we can see that the EB depends on FM and AFM interface exchange coupling, saturation magnetization, and thickness of the FM layer.

3.2.2 Malozemoff Model

The Meiklejohn–Bean model cannot explain the training effect, which after each cycle of hysteresis loops' measurement exchange bias and coercivity decrease, and also cannot give information about the compensated AFM configuration [80]. Malozemoff's model is another model to describe the hysteresis loop shift [80, 81]. Meiklejohn–Bean model predicted interfacial exchange J_i hundred to a thousand times smaller than for experimental bulk FM, and AFM exchange parameters [80]. The model describes the loop shift based on a rough interface between the AFM and the FM and structural defects [79]. Therefore, the random field at the interface causes AFM domains, which is the reason for the exchange-bias shift. The exchange bias shift is then described as

$$H_{EB} = \frac{\Delta\sigma}{2M_F t_F} \tag{3.12}$$

where M_F and t_F are the FM magnetization and thickness, respectively. $\Delta\sigma$ is an energy difference per area of the interface of the FM-AFM, between the two principal time-reversed FM directions [80].

$$\frac{\Delta\sigma}{2M_F t_F} = \frac{f_i J}{aL} \tag{3.13}$$

$\frac{f_i J}{aL}$ is average random-field energy per area, where $f_i = \frac{J}{J_i}$ and $J_i = A_A$.

Substituting Eq. 3.13 into Eq. 3.12, the loop shift is described as

$$H_{EB} = \frac{f_i J}{2M_F t_F aL} = \frac{f_i \sqrt{A_A K_A}}{M_F t_F} \tag{3.14}$$

where A_A and K_A are AFM exchange stiffness and uniaxial anisotropy per unit volume. a is lattice constant, and L is lateral dimension.

3.3 Magnetism and Structure of Mn_2Au

The advantage of using AFM materials in spintronics is that they are fast [82], robust against external fields [83, 84], and do not have a stray field [84]. The AFM can be used in future spintronic devices because they can lead to a smaller size and a faster and more energy-efficient device [84]. Mn_2Au is a bimetallic and collinear AFM that receives large attention due to its unique properties.

Mn_2Au has a bct structure with lattice parameters of a = 3.328 Å and c = 8.539 Å [85, 86, 21]. It has a very strong exchange coupling and shows Néel spin-orbit torques by applying a current [87, 88, 89, 90, 85]. Mn_2Au is a two-sublattice AFM that each has broken inversion symmetry and generates inversion partners [91, 89, 92]. Mn_2Au can be a good candidate for memory applications because it is metallic conductive and has a high T_N above 1000 K [17, 91, 84, 85] which makes it more thermally stable, because thermal fluctuations can affect the dynamics [84], exchange bias and coercivity [75]. The easy axis of Mn_2Au is [110] [93]. The

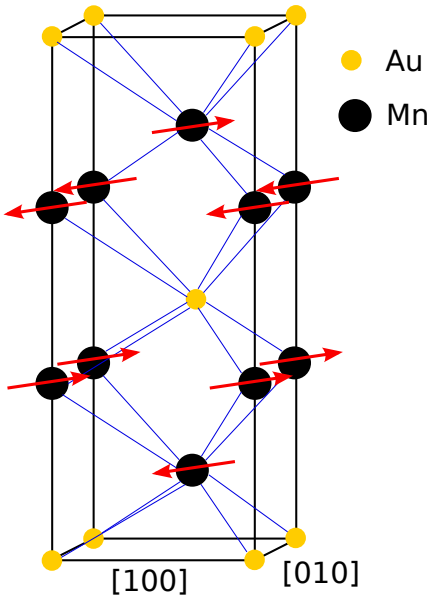

Figure 3.4: Crystal structure of Mn_2Au. The magnetic moments are shown by red arrows. Reprinted with permission from [85] by the American Physical Society and SciPris.

crystal structure of Mn_2Au is shown in Fig. 3.4. The magnetic moments of the Mn atoms align along the easy [110] direction [87, 94]. The magnetic state of Mn_2Au can be controlled by an electric current and can be read out by large anisotropic magnetoresistance measurements [84, 87, 95]. Several methods have been used to study Mn_2Au AFM. Chen et al. used ferroelastic strain from piezoelectric materials to switch the uniaxial magnetic anisotropy in Mn_2Au films with an electric field of only a few kV per cm at room temperature [25]. Wu et al. prepared a spin-valve structure of Fe(10 nm)/MgO(3 nm)/Fe(10 nm)/Mn_2Au(10 nm) on a MgO single-crystal substrate where they used the Mn_2Au as a pinning layer for bottom Fe layer [96]. While Wu et al. observed the exchange bias for their Mn_2Au/Fe bilayers [96], Sapozhnik et al. also revealed the exchange bias for Mn_2Au/Fe bilayers for different Mn_2Au thickness and different growth temperature for Mn_2Au [76], while they kept Fe thickness at 3 nm for all samples. For two of their samples, for which they kept the growth temperature at 600 °C and deposited have 4 and 7 nm Mn_2Au, they did not observe any exchange bias but a coercivity increment for 10 K compared to 300 K. For other two samples, they increased the Mn_2Au thickness to 10 nm and for growth temperatures at 500 and 450 °C, they observed exchange bias. In the

work of Jourdan et al. the MOKE hysteresis loops of an rf sputtered sample of 5 nm Fe on 7 nm $Mn_2Au(001)$ on $Al_2O_3(1\bar{1}02)$ and capped by 5 nm Al showed a coercivity enhancement, but no clear exchange bias [27]. In another work, Sapozhnik et al. studied the spin reorientation in Mn_2Au by applying a high magnetic field (70 T) to observe an X-ray Magnetic Linear Dichroism (XMLD) signal to investigate the domain orientation, and the respective Néel vector [97]. Sapozhnik et al. also observed a spin-flop transition by applying a 70 T. Arana et al. found magnons in 100 nm Mn_2Au by inelastic Brillouin and Raman light scattering [91]. Bodnar et al. imaged the current-induced modification of the AFM domain structure of 80 nm $Mn_2Au(001)$ on $Al_2O_3(1\bar{1}02)$ and capped by 1.8 nm Al by means of XMLD-PEEM and also they found the large AMR effect [88]. The AMR effect of 2.5 % Mn_2Au has been shown by Wu et al. [90]. Jin et al. measured the temperature-dependent sheet conductivity of 5, 10, and 15 nm thick $Mn_2Au(103)$ films (Mn_2Au prepared by magnetron sputtering at 300 °C) on 500 µm single-crystal MgO(100) substrates by THz time-domain spectroscopy as well as the time-resolved photoconductivity of these samples by optical pump-THz probe spectroscopy [98]. Singh and Bedanta studied spin pumping and the inverse spin Hall effect in a Co-Fe-B(5 nm)/Mn_2Au(10 nm) bilayer on MgO(100) capped by 2 nm TaO_x (the sample prepared by dc magnetron sputtering) by ferromagnetic resonance and found a large spin Hall angle (0.22) [99]. Jia et al. studied Néel order switching in the HM/Mn_2Au bilayer and HM/Mn_2Au/HM trilayer (HM, heavy metal), and found a robust picosecond switching of the Néel order in the HM/Mn_2Au/HM trilayer [29]. Zhou et al. showed current-induced AFM moment switching in $Mn_2Au(103)$ and $Mn_2Au(103)$/Pt on a single-crystal MgO(100) substrate, where the samples were prepared by magnetron sputtering [92].

CHAPTER 4

Au, Mn, and Co Growth on Cu(001)

In this chapter, we study the Au, Mn, and Co growth on Cu(001). The samples are prepared by electron beam evaporation. The growth mode is monitored by MEED. The films' structure and magnetic properties are studied. The structure of the samples is analyzed by LEED, XRMR, and STM. The magnetic property of the sample is explored by XMCD in reflectivity resonant.

4.1 MEED Results of Au/Mn/Co/Cu(001)

In Figs. 4.1, 4.2, and 4.3, we show the MEED oscillations of Co growing on Cu(001), Mn on Co, and Au on Mn/Co, respectively. We can see from Fig. 4.1 that the Co MEED curves do not start from the maximum intensity. There might be several reasons for that. It could be that the substrate is rough, as mentioned in Ref. [100]; this could be a reason why the intensity starts low and then increases. We can see this behavior for several thicknesses of Co from 3.6 to 14.3 ML, as shown in Fig. A.1. However, we can see that the LEED patterns of Cu(001) after sputtering and annealing (around 900 K) are sharp, which confirms the crystallinity of Cu(001). Another reason could be that the adjustment of the Cu(001) crystal for the MEED (00) spot is not in the maximum diffraction intensity. Therefore, the MEED curves start from low and then increases. The intensity of the MEED curves for most Mn films on Co/Cu(001) starts from maximum intensity, then they drop. The Co films' thicknesses are shown in the legend in Figs. 4.1 and A.1. The Mn films' thicknesses are also shown in the legend in Fig. 4.2. We can see from the Co thickness they are not completed layers; therefore Mn starts to fill empty/uncovered parts.

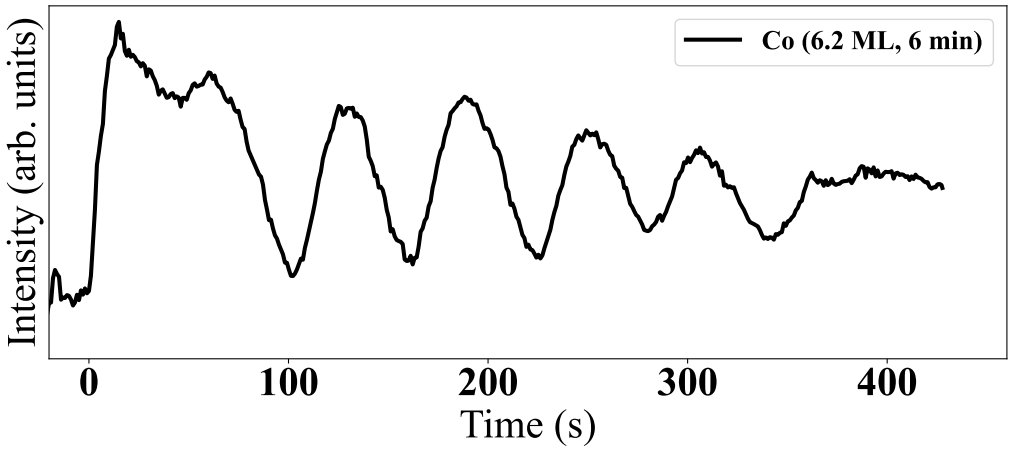

Figure 4.1: The MEED oscillations of 6.2 ML Co growth on Cu(001). Time "0" defines the shutter open and the closing time is defined in the legend in the bracket.

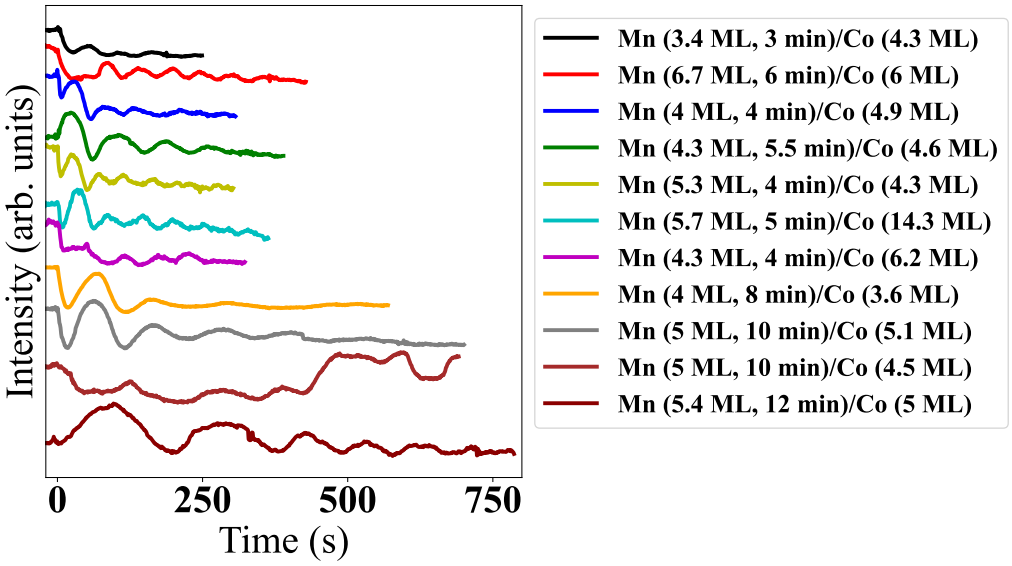

Figure 4.2: The MEED oscillations for Mn growth on Co/Cu(001) from 3.4 to 6.7 ML. The "0" defines the shutter open, and the closing time is defined in the label in the bracket.

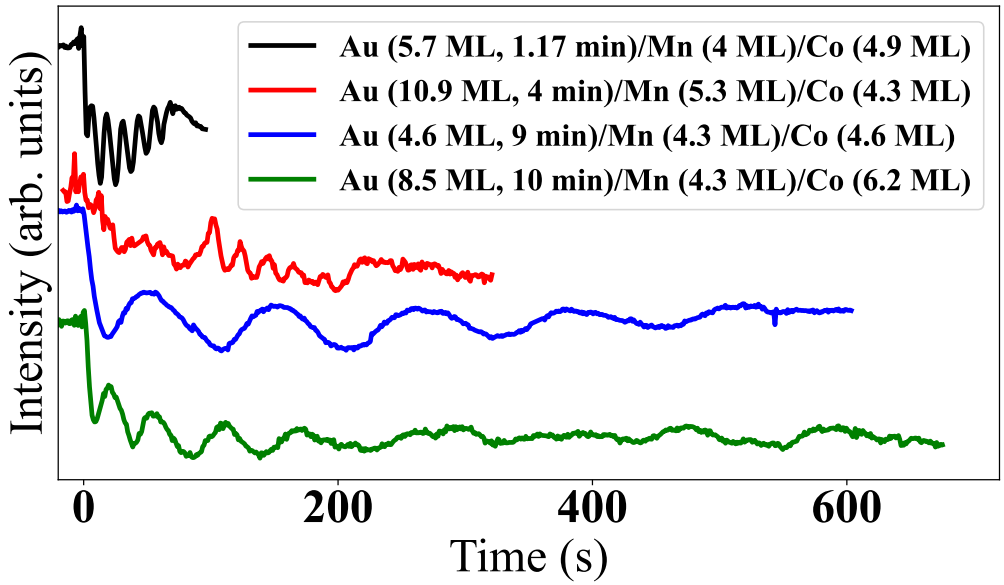

Figure 4.3: The MEED oscillations for Au growth on Mn/Co/Cu(001) from 4.9 to 10.9 ML. Time "0" defines the shutter open, and the closing time is defined in the legend in the bracket.

4.2 LEED and LEED-I(V) Results of Au/Mn/Co/Cu(001)

After film preparation, we employed LEED and LEED-I(V) to investigate the structure of the films. In Fig. 4.4, we show the LEED pattern of clean Cu(001) at 125 eV. In Fig. 4.5, we see LEED patterns after Co growth on Cu(001) and subsequently, after Mn growth on this Co/Cu(001). The LEED pattern of Co on Cu(001) displays a p(1×1) structure. Mn films on Co/Cu(001) display p(1×1) as Co films. In some samples, the (01) spot is visible; in some of them, the spots are not visible at a beam energy of 117 eV. In Fig. 4.6(a), (b), and (c), we show LEED patterns after Co growth on Cu(001), Mn growth on Co/Cu(001), and Au growth on Mn/Co/Cu(001) films for samples of Au(5.7)/Mn(4.0)/Co(4.9)/Cu(001), Au(4.6)/Mn(4.3 ML)/Co(4.6)/Cu(001) and Au(4.3)/Mn(5.3)/Co(10.9)/Cu(001), respectively. In Fig. 4.6(a) and (b), samples display p(1×1) patterns after Co and Mn growth. However, the Au films on Mn/Co/Cu(001) display LEED patterns, but it is not clear enough to define the pattern structure as shown in Fig. 4.6(a).

Contracted face-centered tetragonal (c-fct) Co films grow on Cu(001) and ex-

panded face-centered tetragonal (e-fct) Mn(001) films grow on Co(001)/Cu(001) [101]. The Co films grow fcc on Cu(001) as tetragonally compressed due to films and substrate lattice mismatch [102]. Fig. 4.7 (a) shows the LEED-I(V) curves for the (00) spot for the substrate, Co, and Mn films deposited subsequently. From these, we can calculate the vertical interlayer spacing for the substrate and the films. In Fig. 4.7 (b), we show the interlayer spacing extracted from Fig. 4.7 (a) from the kinematic approximation. We can see that d_p for Cu(001) is 1.85 Å. The bulk fcc Cu(001) vertical layer spacing is 1.808 Å [41]. After Co growth on Cu(001), d_p gets lower. When we grow Mn films on Co/Cu(001), the d_p gets bigger. Our experimental d_p for Co on Cu(001) and Mn on Co/Cu(001) are shown in Fig. 4.7 (b) and tabulated in Tab. 4.1. In the work of Offi et al. they show that for 6.0 ML Co on Cu(001) d_p is around 1.74 Å [102], when the film thickness of FeMn films increases on Co/Cu(001), the d_p after FeMn film thicknesses get bigger. We also observe the same behavior for pure Mn thin films deposited on Co films of different thicknesses on Cu(001). In the work of Wu et al., they observed the layer distance of 2.01 Å in a 2.8 ML Mn film on 4.5 ML Co/Cu(001) from STM topography images [48]. In the work of Hsu et al. they observed the vertical layer distance of 1.74 Å and 1.89 Å for 5.5 ML Co/Cu(001) and 3.5 ML Mn film on 5.5 ML Co/Cu(001), respectively. The vertical interlayer distance for 10 ML Co on Cu(001) is around 1.73 Å and 16.7 ML Mn on 10 ML Co/Cu(001) show 1.88 Å [103]. The results of d_p from measurement and literature are summarized in Tab. 4.1, we can see that our measurement d_p result for Co thin films on Cu(001) and Mn films on Co/Cu(001) are comparable. Up to 8-9 ML Co grown on Cu(001) shows a p(1×1) LEED pattern [104]. The Mn film grown on Co/Cu(001) shows a p(1×1) LEED pattern, too. A low coverage of Mn films on Co/Cu(001) (around 0.3-0.8 ML) displays a c(2×2) superstructure LEED pattern [104]. Mn grows up to about 10-15 ML in a layer-by-layer mode onto strained Co(001), when Mn films get thicker, the film becomes rougher, and surface topography moves disordered [105]. Due to the lack of LEED patterns of Au films deposited on Mn/Co/Cu(001), we could not do LEED-I(V) measurements.

Table 4.1: d_p from LEED-I(V) results comparisons for Mn/Co/Cu(001) and Co/Cu(001) thin films experimental and literature values. The errors in thicknesses are 0.2 ML. The error in vertical interlayer distances are shown in Fig. 4.7.

Co (ML)	d_p (Å)	Mn (ML)	d_p (Å)	Method
14.3	1.75	5.7	1.94	LEED-I(V)
4.3	1.77	5.3	2.00	LEED-I(V)
4.6	1.77	4.3	1.95	LEED-I(V)
5.1	1.77	5	1.96	LEED-I(V)
6	1.74	-	-	LEED-I(V) [102]
5.5	1.74	3.5	1.89	LEED-I(V) [101]
10	1.73	16.7	1.88	LEED-I(V) [105]
4.5	-	2.8	2.01	STM [48]

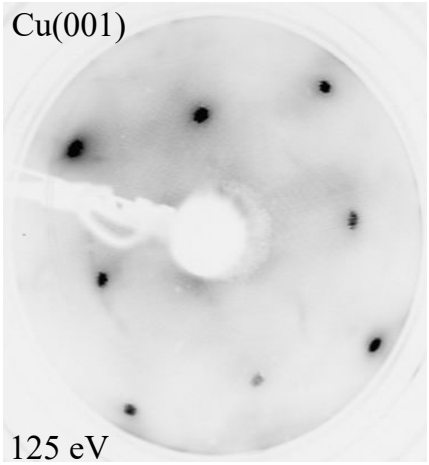

Figure 4.4: The LEED pattern of clean Cu(001) at beam energy 125 eV.

4.3 STM of Au/Mn/Co/Cu(001)

We also employed STM to investigate the morphology of Au (4.6 ML)/Mn (4.3 ML)/Co (4.6 ML)/Cu(001) at room temperature. We can see the formation of islands from the STM topography image in Fig. 4.8. The step height of this film is between 0.2 and 0.6 nm (from the scan along the white line in Fig. 4.8). The LEED patterns of this sample are shown in Fig. 4.6 (b) after the deposition of Co, Mn, and Au, respectively. We can see that there is no clear LEED pattern after deposition of 4.6 ML Au on Mn(4.3 ML)/Co(4.6 ML)/Cu(001). Therefore, we are not expecting a full covered surface from the STM image. The layer height is quite in a reasonable range which is between 2 to 6 Å. We also can see that the surface is

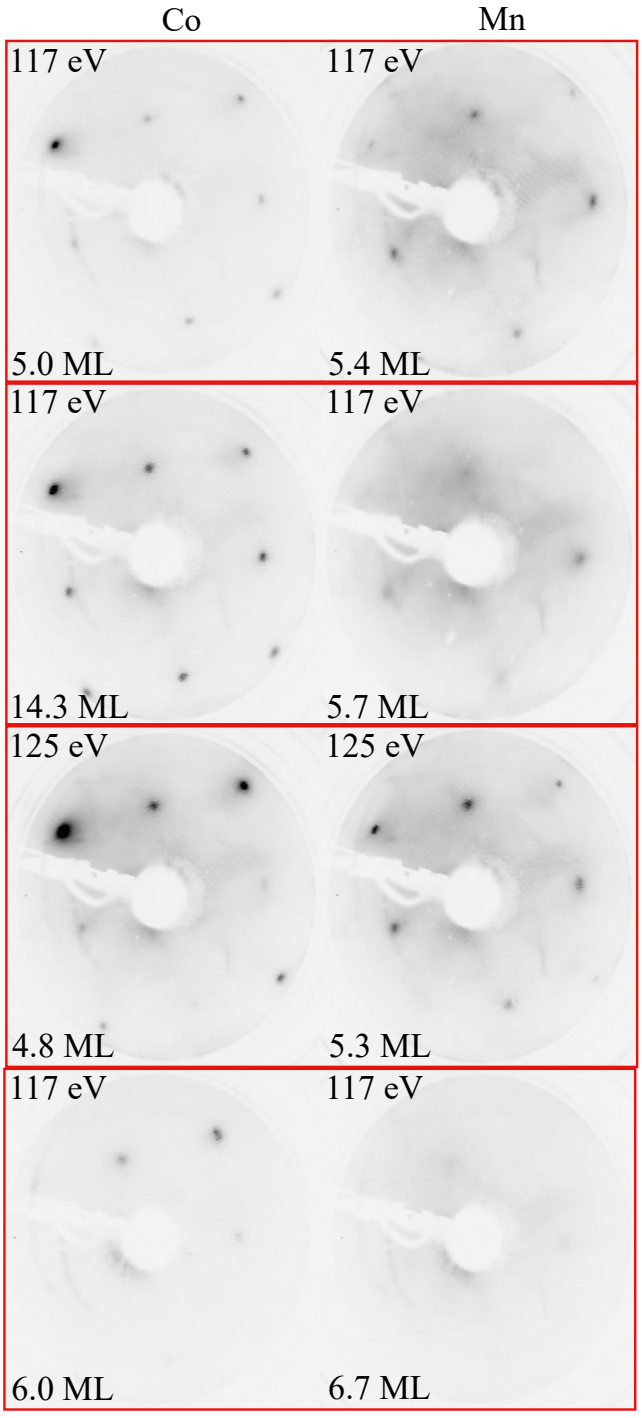

Figure 4.5: Left: The LEED patterns of several Co thin films on Cu(001) and, right: Mn thin films on Co thin film. The beam energy and film thicknesses are mentioned in the images.

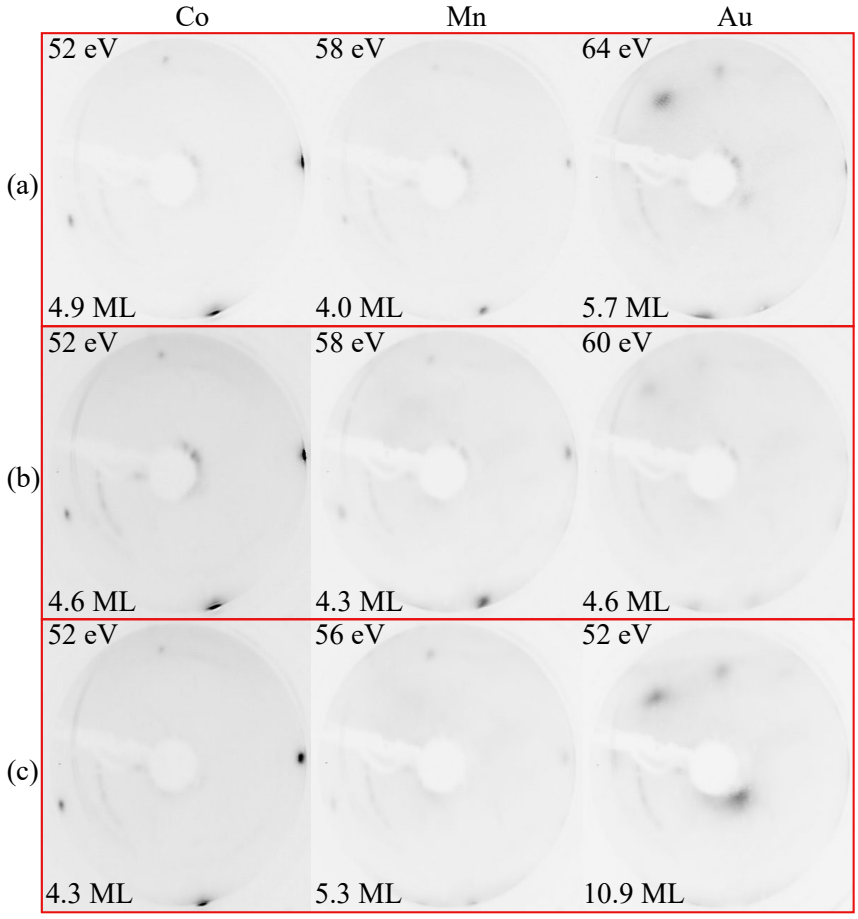

Figure 4.6: The LEED patterns of Au/Mn/Co/Cu(001) for three different samples in (a) Au (5.7 ML)/Mn (4 ML)/Co (4.9 ML)/Cu(001), (b) Au (4.6 ML)/Mn (4.3 ML)/Co (4.6 ML)/Cu(001), and (c) Au (10.9 ML)/Mn (5.3 ML)/Co (4.3 ML)/Cu(001). The beam energy and film thicknesses are mentioned in the images.

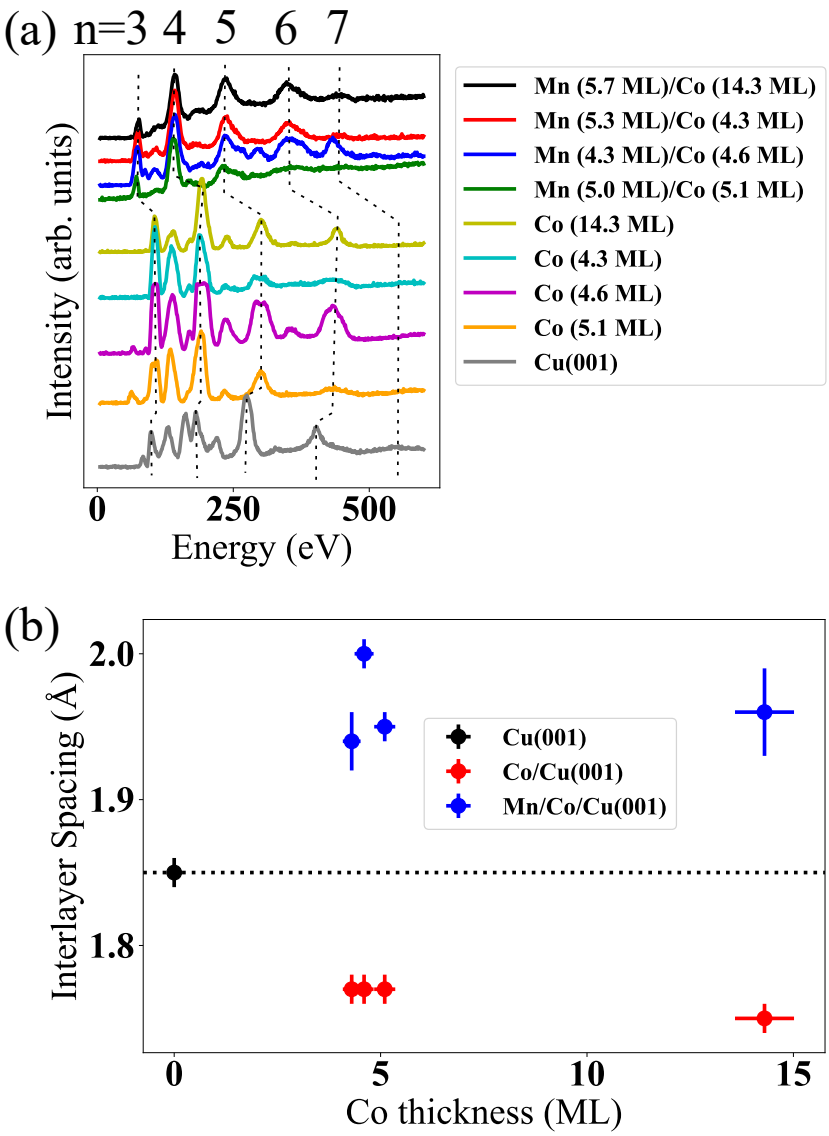

Figure 4.7: (a) The LEED-I(V) curves of the (00) spot clean Cu(001), Co (from 4.3 to 14.3 ML) on Cu(001), and Mn (from 4.3 to 5.7 ML) on Co/Cu(001). (b) Vertical interlayer spacing from (a), which is calculated from the kinematic approximation.

not very rough.

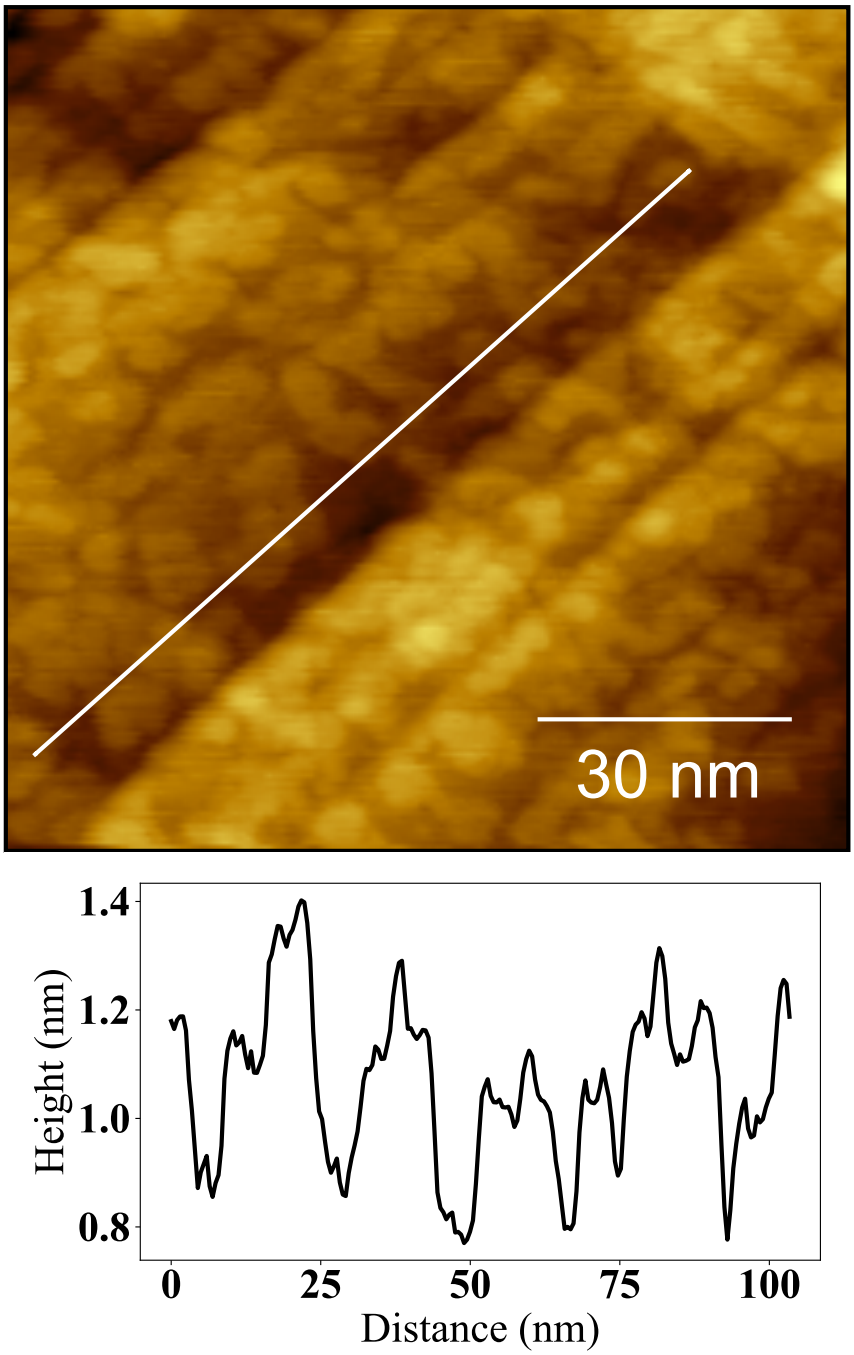

Figure 4.8: The top image is an STM image of Au (4.6 ML)/Mn (4.3 ML)/Co (4.6 ML)/Cu(001) at constant-current mode at RT. The feedback parameters are 0.48 nA and 1.0 V. The bottom image is a line scan along the white line of the top image.

4.4 XRMR-XMCD of Au/Mn/Co/Cu(001)

We investigated the magnetic properties of ultra-thin films by employing X-ray resonant magnetic reflectivity (XRMR) measurements at BESSY-II at the Mn and Co L_3 absorption edges at 639.1 and 778 eV, respectively. XRMR is an elemental- and depth-selective measurement technique that measures the reflectivity vs. θ and 2θ. The θ refers to the angle between sample surface and incoming x-ray beam, while 2θ is the angle between incoming and reflected beam. A schematic view of the XRMR measurement geometry is shown in Fig. 2.19. XRMR curves are shown in Fig. 4.9 (a), (b) for Mn and Co, respectively. The XRMR reflectivity curves are plotted for intensity vs. scattering vector q_z. The sample consisted of 5.3 ML Co on Cu(001), then 5.7 ML Mn and finally 14 ML Au. The growth of the film was monitored by MEED. Au first displayed MEED oscillations (7.0 ML), then, in a second cycle with the same parameters, another 7.0 ML of Au was evaporated on top.

In this work, we obtained experimental XRMR data and simulated the data by ReMagX simulation [68, 62, 69], as shown in Fig. 4.9. We simulated the thin films' XRMR curves, by introducing the films' thickness, roughness, and optical constants. We set the incoming and analyzer polarizations to circular (+/-) and unpolarized, respectively. The thickness values for Co and Mn as obtained from MEED curves were used, while the Au thickness was adapted manually, consistent with an estimate from the MEED curve of the initial Au deposition step (the second deposition step did not yield a usable MEED curve). Fig. 4.9 (a) and (b) show the experimental data and their simulation results of the 11.7 Å Mn/8.85 Å Co bilayer with 40 Å Au capping at the Mn (639.1 eV) and Co (778 eV) L_3-edges, respectively, for both polarization directions. We can see that there is no difference for XRMR spectra at the Mn $L_{2,3}$-edges for opposite circular polarization. However, there is a clear XMCD difference at the Co L_3-edge for opposite circular polarization. The roughness value for the best fit and optical constants that we used for the XRMR simulation are summarized in Tab. 4.2 and 4.3, respectively. The optical constants for Mn and Co around their respective $L_{2,3}$ absorption edges are taken from another

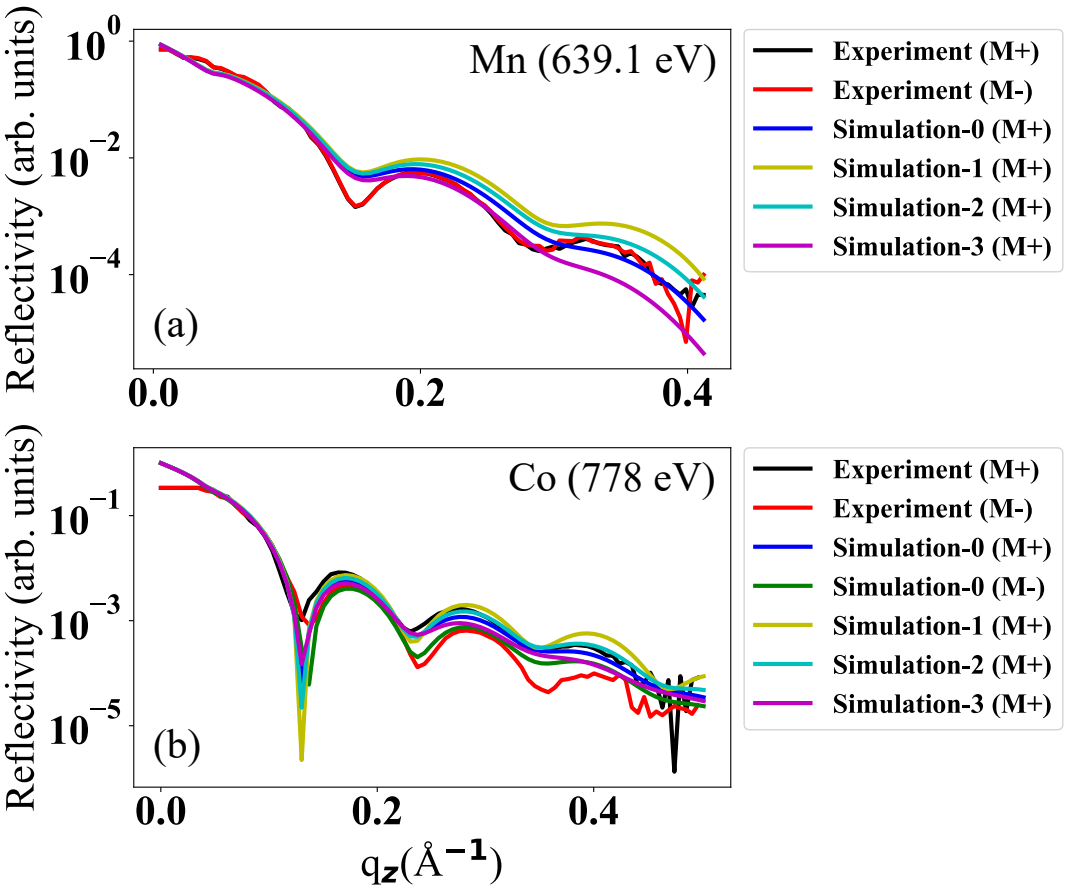

Figure 4.9: XRMR curves of Au (14 ML)/Mn (5.7 ML)/Co (5.3 ML)/Cu(001). Dichroic measurement and simulation of samples at (a) 639.1 eV and (b) 778 eV. The simulations have been done for 38, 11.7, and 8.85 Å of Au, Mn, and Co, respectively. The measurement has been done by applying a magnetic field of −1 and 1 T for the curves labeled "M+" and "M-", respectively. The optical constants and roughnesses are summarized in Tabs. 4.2 and 4.3, respectively.

sample which was studied by Ivar Kumberg [66]. The optical constants for Au and Cu as well as for Mn and Co outside the $L_{2,3}$ absorption edges are taken from the Henke tables [106, 107]. In Fig. 4.9, we compare different roughnesses for Co and Mn L_3-edges to investigate the effect of roughness on the XRMR curves. We summarized these different roughness parameters in Tab. 4.3. When we use the intensity at higher values of q_z as a criterium for a good fit, then at the interface, the roughness is very low for a good fit at the Co (778 eV) L_3-edge, about 2 Å. But the roughness is higher when comparing the simulations at the Mn (639.1 eV) L_3-edge to the experiment, about 3 Å. Because the roughnesses do not depend on which edge it is measured, we can say that the interface roughnesses are in the range of 2-3 Å.

We call spectra of the X-ray reflectivity vs. photon energy "XRR". In XRR simulations, we used the same optical constants as for the XRMR simulations. We set the incoming and analyzer polarizations to circular (-) and unpolarized, respectively. The reflected intensity as a function of $\hbar\omega$ is calculated by the second approach to simulate the reflectivity that has been done by UDKM1DSIM. The values of the parameters are introduced manually to obtain the best fit. Vertical lattice constants and film thicknesses are taken as obtained from LEED-I(V) and MEED experiments, respectively.

Table 4.2: The optical constants used for simulations of the XRMR of Au (38 Å)/ Mn (11.7 Å)/Co (8.85 Å)/Cu(001) by ReMagX at 639.1 eV and 778 eV, which are shown in Fig. 4.9.

Films	Energy (eV)	δ	β	δm	βm
Au	639.1	3.73E-3	3.01E-3	0	0
Mn	639.1	-6.80E-3	1.03E-2	0	0
Co	639.1	2.02E-3	3.60E-4	0	0
Cu	639.1	2.72E-3	5.60E-4	0	0
Au	778	2.95E-3	1.95E-3	0	0
Mn	778	1.54E-3	1.49E-3	0	0
Co	778	-7.3E-4	6.3E-3	-7.28E-5	-9.4E-4
Cu	778	1.65E-3	2.98E-4	0	0

We show absorption spectra measured by total electron yield (TEY) and X-

Table 4.3: The different roughnesses (σ(Å)) that are used for simulations of Au (38 Å)/Mn (11.7 Å)/Co (8.85 Å)/Cu(001) by ReMagX at 778 eV, which are shown in Fig. 4.9.

Simulations	Au (Å)	Mn (Å)	Co (Å)	Cu (Å)
Simulation-0 (M+)	4	3	3	0
Simulation-1 (M+)	0	0	0	0
Simulation-2 (M+)	3	2	2	0
Simulation-3 (M+)	5	4	4	0

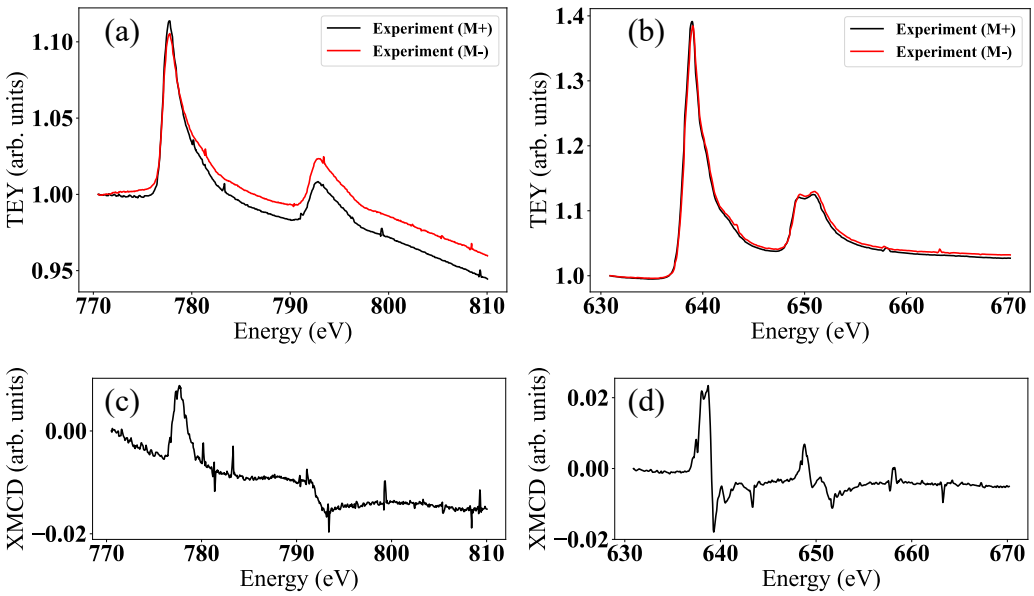

Figure 4.10: X-ray absorption measured by TEY at the (a) Co, (b) Mn $L_{2,3}$ edge. (c) and (d) are the corresponding XMCD spectra (the difference between −1 and 1 T) of (a) and (b), respectively, obtained for normal incidence for the sample of Au (14 ML)/Mn (5.7 ML)/Co (5.3 ML)/Cu(001). The TEY spectra are normalized to the pre-edge.

ray magnetic circular dichroism (XMCD) spectra for Mn and Co in Fig. 4.10. In Fig. 4.10 (a) and (b), we show spectra of TEY and XMCD, respectively, at the Co $L_{2,3}$ edge at normal incidence. In Fig. 4.10 (c) and (d), we show TEY and XMCD spectra, respectively, at the Mn $L_{2,3}$ edge at normal incidence. Fig. 4.10 (c) shows a very clear XMCD of Co (XMCD is obtained by subtraction of reversed magnetized spectra). Fig. 4.10 (d) shows a very weak XMCD of Mn. In Fig. 4.11, we display XRR and XMCD of Co under different angles (θ=9° and 15.5°) together with related simulations. In Fig. 4.11, the XRR shows opposite sign of peaks at the two angles as well as good qualitative agreement of experiment and simulation.

There is a clear XMCD at both angles as shown in Fig. 4.11 (b) and (d).

We used XRMR to obtain hysteresis loops for Co at a photon energy of 778 eV for angles θ=9° and θ=17.5°. There is a clear hysteresis for Co films, as shown in Fig. 4.12. Fig. 4.12 (a) has a higher magnetic dichroism than the one in Fig. 4.12 (b). We can see that the signs for these two hysteresis loops are opposite. This agrees with XRMR (Fig. 4.9 (b)), that the sign changes between these two θ angles. The q_z values for θ= 9° and 17.5° are 0.12 Å^{-1} and 0.23 Å^{-1}, respectively.

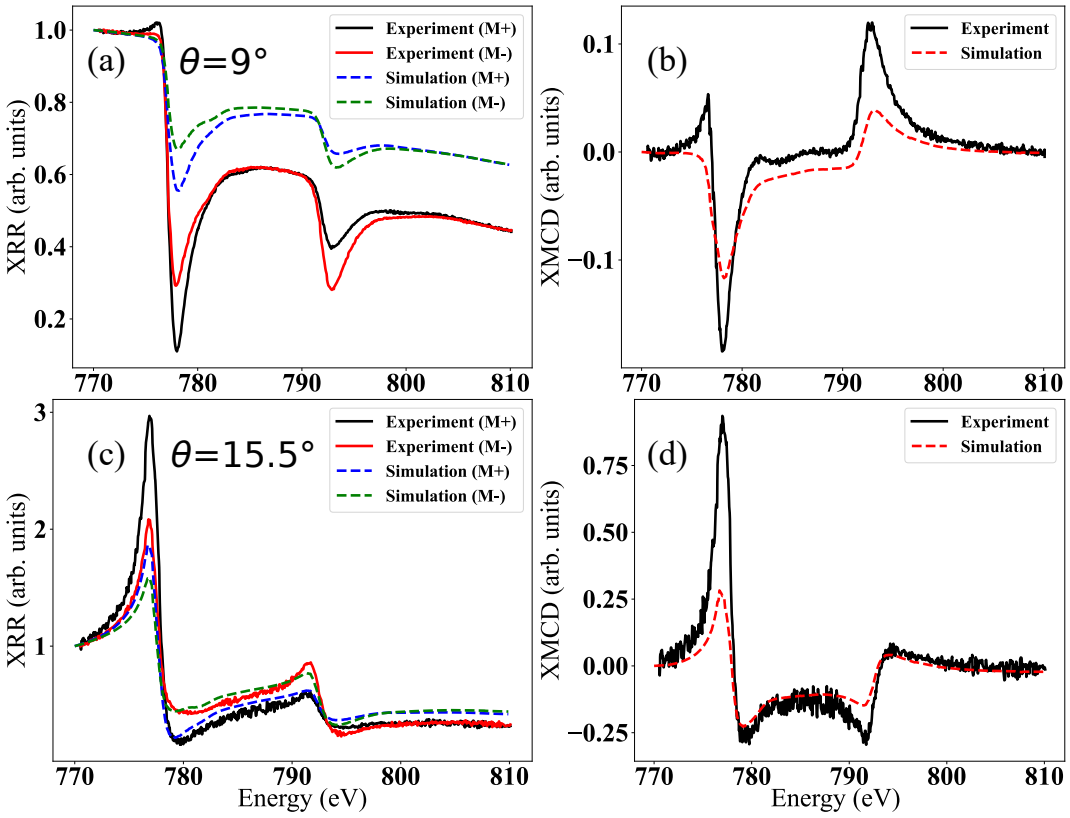

Figure 4.11: X-ray reflectivity at the Co $L_{2,3}$ edge at (a) θ=9° and (c) θ=15.5°. (b) and (d) are the corresponding XMCD spectra (the difference between -1 and 1 T) of (a) and (c), respectively. The XRR spectra are normalized to the pre-edge.

4.5 Summary

This work aimed to define the Au, Mn, and Co growth rate and the film quality and interlayer diffusion. XAS and XRMR were employed to investigate interlayer diffusion, the film thickness, and the magnetic properties of Mn/Co bilayers. MEED oscillations were observed for all three materials (Au, Mn, Co) on Cu(001), which

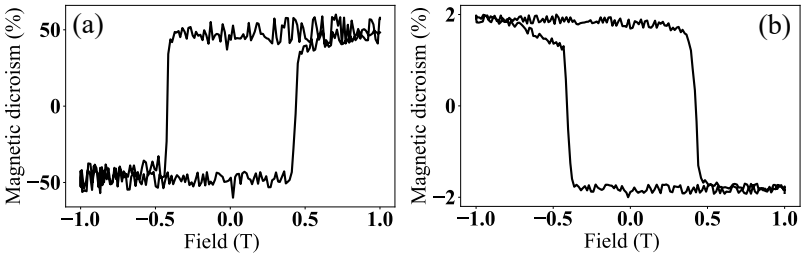

Figure 4.12: Hysteresis curves of the Co L_3 edge at 778 eV for angle (a) θ=17.5°and (b) θ=9 °.

demonstrates layer-by-layer growth. For the crystal structure, the sample is also checked by LEED, which displays p(1×1) patterns for Co on Cu(001) and Mn on Co/Cu(001), as displayed in Figs. 4.5 and 4.6. However, we could not see any LEED pattern for the Au overlayer on Mn/Co/Cu(001). STM reveals the Au growth morphology on Mn/Co/Cu(001), which shows a two-layer islands growth mode instead of a uniform/full surface coverage. XRMR is being used to investigate the trilayer films grown on Cu(001) and shows that the sample grows nicely without a very high interlayer diffusion/roughness. XRMR Co and Mn simulations yield thicknesses close to the thickness values that were obtained from MEED. However, the Au thickness was higher. For the gold deposition, we got MEED oscillations for the first deposition. However, when we tried to deposit Au a second time to increase the Au capping-layer thickness, we could not see any oscillations, although we tried to keep the same conditions. That shows that growing Au by wrapping an Au piece with a tungsten wire would not be easy. Therefore, we suggest that in case of working with Au, it would be better to use a QCM (quartz crystal microbalance) for monitoring the deposited thickness and also an electron beam evaporator, if possible with a PBN (pyrolytic boron nitride) crucible to be able to achieve a more precise Au growth rate. Besides that, we also observed a clear XMCD of Co and a weak XMCD of Mn by XAS and XRMR.

CHAPTER 5

STM Study of Initial Growth of Mn_xAu_{1-x} on Cu(001)

5.1 Growth of Mn_xAu_{1-x} on Cu(001)

In this work, Mn_xAu_{1-x} grown on Cu(001) from sub-ML up to some few ML was studied in-situ by MEED, LEED, AES, and STM to investigate the growth, structure, and morphology of the films.

What we studied for Mn_xAu_{1-x} alloy films from LEED images has already been studied for Au and Mn growth on Cu(001) separately. The Mn atomic radius (1.365 Å) is similar to the one of Cu (1.276 Å) and smaller than for Au (1.442 Å) [108]. Au and Cu intermix in the topmost surface layer, then they form a checkerboard array 1 ML thick [109]. Depending on the amount of Au deposited on Cu(001), it displays a different structure. In the case of a sub-ML Au on Cu(001), up to 0.5 ML ML coverage of Au on Cu(001) displays the p(1×1) substrate pattern [30]. At 0.5 ML Au grown on Cu(001) at room temperature, the LEED pattern displays a real-space c(2×2) unit cell [109, 110]. But also, the growth temperature plays a role for the Au structure on Cu(001). 0.5 ML Au on Cu(001) prepared at 173 K shows a p(1×1) LEED pattern, but when heated to room temperature, a c(2×2) LEED pattern appeared [109]. Besides studying the structure of Au by LEED, Tobin et al. studied 0.5 ML Au on Cu(001) also by photoelectron diffraction and observed a c(2×2) structure [111]. 1 ML Au on Cu(001) prepared at 173 K shows a c(14×2) LEED pattern, when returned to room temperature, the c(2×2) LEED pattern appeared [109]. In the case of a high coverage, a pgg(4×2) structure above 1 ML coverage at 370 K [110] appeared. In another work, above 1 ML coverage of Au, the surface develops into a Au(111)-like structure [109]. In Yamada et al., they investigated the stable c(2×2) MnAu(001) alloy layers by growing the Au on bct Mn(001) film at room temperature [19, 112]. Besides the structural changes of Au grown on Cu(001), also the binding energy of Cu changes.

From 0.5 ML to 1 ML Au, the alloy surface state shifts to higher binding energies compared to the value of the original Cu(001) $\overline{M}$ surface state [109].

Mn on Cu(001) displays a surface alloy with a long-range alloy compositional order. In 0.5 ML, it shows a c(2×2) superstructure. The c(2×2) structure is observed after deposition of approximately 0.5 ML Mn on the Cu(001) surface held above 270 K. This phase is stable upon cooling to 80 K and annealing to 470 K [108]. In the case of growth of Mn below 270 K, Mn grows in a c(8×2) structure up to about the monolayer coverage and rearranges at higher coverage. Above 270 K, Mn forms ordered surface alloys with a c(2×2) superstructure [113]. Mn has a large magnetic moment. For the growth of Mn on Cu(001), the atomic structure is characterized by around 0.3 Å atomic corrugation, in which outward buckling of Mn could be identified by STM [114]. In the work of Huttel, they showed that 0.5 ML Mn was grown on Cu(001) to create a CuMn alloy and a c(2×2) LEED pattern [31]. They observed the X-ray magnetic circular dichroism (XMCD) at low temperature. The long-range magnetic order of the c(2×2) MnCu(100) surface alloy at low temperature ($<$ 50 K) is observed. In their work, the contaminated surfaces showed traces of oxygen in AES spectra and no c(2×2) LEED diagram.

Here, the initial stages of surface-alloy and over-layer formation of Mn_xAu_{1-x} films on Cu(001) were investigated. The thin films were evaporated from the electron beam evaporator on Cu(001). The topographical and structural information obtained in an STM measurement allows us to study the growth in detail in real space. The coverage is determined by STM for low coverages, for thicker films by MEED. The sub-ML coverages, from STM images by measuring the percentage of surface covered by islands in the sub-ML range. In the sub-ML coverage, islands of the first atomic layer of the film get bigger when the coverage increases. In Tab. 5.2, we display the coverage of the films calculated from STM images and the LEED patterns of those samples. 'x', the Mn amount in Mn_xAu_{1-x} alloy, is extracted from AES. For thicker films, the thickness is determined by getting the growth rate from MEED oscillations. As a conclusion, what we observed is that at low coverages

($\leq$ 1 ML) the films grow as epitaxially (in the Frank–van der Merve growth mode), which is seen in STM topography images. Above 1 ML, the films get rougher. Up to 0.5 ML, the LEED image shows the substrate pattern (p(1×1)), then, the images are getting dimmer. Between 0.5 and 1 ML, the LEED images display a c(2×2) structure. Above 1 ML, the LEED patterns get dim and vanish. LEED and STM images do not show sharp patterns and flat surfaces, respectively. However, MEED oscillations are observed up to 9 ML.

5.2 STM, LEED, and AES of Cu(001)

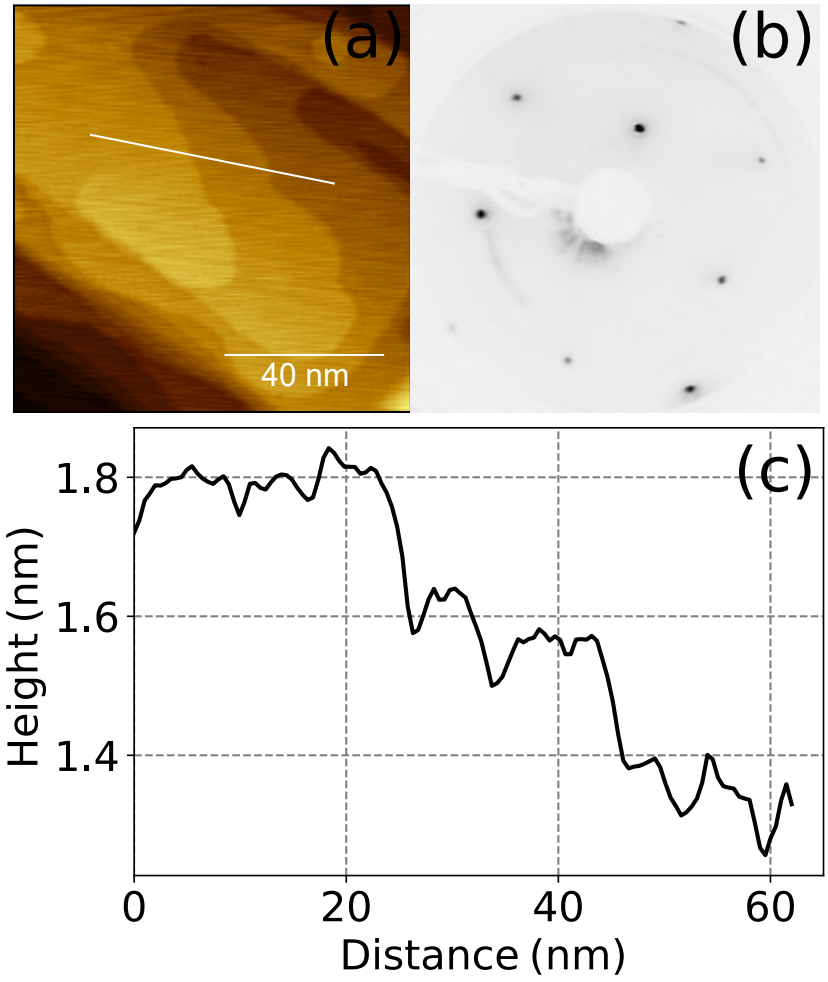

Figure 5.1: (a) STM topography image of Cu(001). STM feedback parameter for (a) is 0.7 nA×1 V, (c) is a line scan of (a) along the white line. (b) LEED image of clean and annealed Cu(001) at 132.5 eV.

In Fig. 5.1, we can see the clean single crystal Cu(001). STM, LEED, and line

scan of the white line in 5.1 (a) are shown in Fig. 5.1 (a), (b), and (c), respectively.

5.3 AES Results

AES is used to investigate the chemical composition and also film thickness. No carbon, oxygen or any other contamination could be detected by AES. Mn and Cu show several Auger transitions in the energy region up to 1 keV. Au has peaks in the low-energy regime. Therefore it makes it harder for a quantitative calculation. At lower energies ($<$ 100 eV), the IMFP (Inelastic Mean Free Path) is very low ($\approx$ 5 Å). Therefore, in this range, AES is very surface-sensitive, while when using higher Cu Auger transitions (920 eV), the attenuation length is longer.

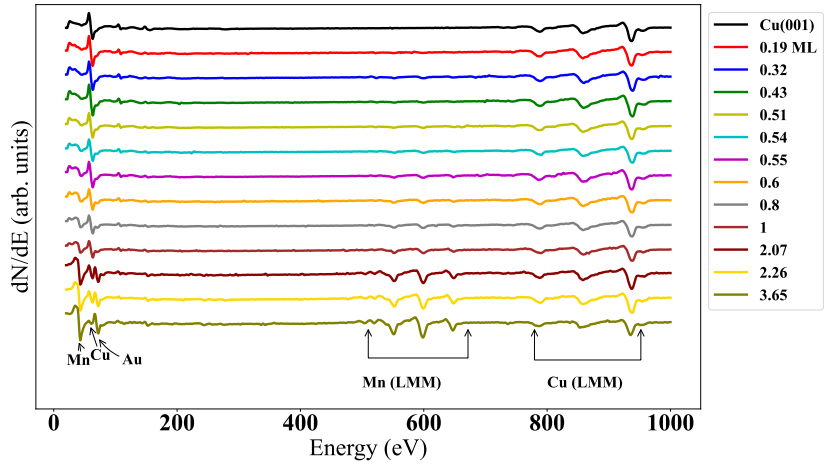

Figure 5.2: Auger survey spectrum of clean Cu(001) and from 0.19 to 3.65 ML Mn_xAu_{1-x} on Cu(001). The y-axis is offset for seeing the spectra clearly.

By AES, we can assure the components of the sample. We display the AES spectra of Mn_xAu_{1-x} (from 0.19 to 3.65 ML) on Cu(001) in Fig. 5.2. They show that the samples are not contaminated. For lower coverages ($<$ 1 ML), the peak heights for Au (69 eV) and Mn (40 eV) are low but already visible. They get bigger for higher film thicknesses. At the same time, the Cu (60 eV) Auger transition is getting smaller.

The sub-ML coverage of Mn_xAu_{1-x} on Cu(001) can be calculated by Eq. 5.1. For thicker films (above 1 ML), Eq. 5.2 are used for ratio and thickness calculation:

$$\frac{I_{Mn}}{I_{Cu}} = \frac{S_{Mn}}{S_{Cu}} \cdot x \cdot \frac{1 - \exp(-1\,\mathrm{ML}/\lambda_{Mn}) \cdot \theta}{\exp(-1\,\mathrm{ML}/\lambda_{Cu}) \cdot \theta + 1 - \theta} \tag{5.1a}$$

$$\frac{I_{Au}}{I_{Cu}} = \frac{S_{Au}}{S_{Cu}} \cdot (1 - x) \cdot \frac{1 - \exp(-1\,\mathrm{ML}/\lambda_{Au}) \cdot \theta}{\exp(-1\,\mathrm{ML}/\lambda_{Cu}) \cdot \theta + 1 - \theta} \tag{5.1b}$$

$$\frac{I_{Mn}}{I_{Au}} = \frac{S_{Mn}}{S_{Au}} \cdot \frac{x}{1 - x} \cdot \frac{1 - \exp(-1\,\mathrm{ML}/\lambda_{Mn})}{1 - \exp(-1\,\mathrm{ML}/\lambda_{Au})} \tag{5.1c}$$

$$\frac{I_{Mn}}{I_{Cu}} = \frac{S_{Mn}}{S_{Cu}} \cdot x \cdot \frac{1 - \exp(-d/\lambda_{Mn})}{\exp(-d/\lambda_{Cu})} \tag{5.2a}$$

$$\frac{I_{Au}}{I_{Cu}} = \frac{S_{Au}}{S_{Cu}} \cdot (1 - x) \cdot \frac{1 - \exp(-d/\lambda_{Au})}{\exp(-d/\lambda_{Cu})} \tag{5.2b}$$

where I, S, d, θ, and λ are Auger intensity, sensitivity, film thickness, alloy film coverage, and effective IMFP, respectively, for Mn, Au, and Cu Auger electron transitions. For thicker films, substrate Auger electrons have to go through a film, so the signal exponentially decays. However, for the 1 ML or partly covered substrate, the Auger electrons of the substrate only go through 1 ML or the uncovered part; therefore, we have two equations for these sub-ML and thicker films as shown in equations 5.1 and 5.2, respectively. The parameters that are going to be used for the calculations are summarized in Tab. 5.1. The parameters in Tab. 5.1 for Mn (40 and 589 eV) were obtained by growing Mn on Cu(001). Sensitivity factors for Au (69 eV) and Cu (60 eV) are obtained from bulk single crystal Cu_3Au. The λ (IMFP) for 40, 60, and 69 eV are obtained from an empirical relation [38].

Table 5.1: Auger thickness calculation parameters.

Auger Peak	S	λ (ML)
Cu(920 eV)	0.97* ($\pm$ 0.04)	4.8* ($\pm$ 0.15)
Mn(589 eV)	1.18* ($\pm$ 0.04)	4* ($\pm$ 0.15)
Au(69 eV)	2.5 ($\pm$ 0.09)	1.76 ($\pm$ 0.06)
Cu(60 eV)	1 ($\pm$ 0.04)	1.69 ($\pm$ 0.06)
Mn(40 eV)	0.8 ($\pm$ 0.04)	1.59 ($\pm$ 0.06)

* S and λ are taken from Y. Shokr, Ph.D. thesis [115]. The λ for low energy is calculated.

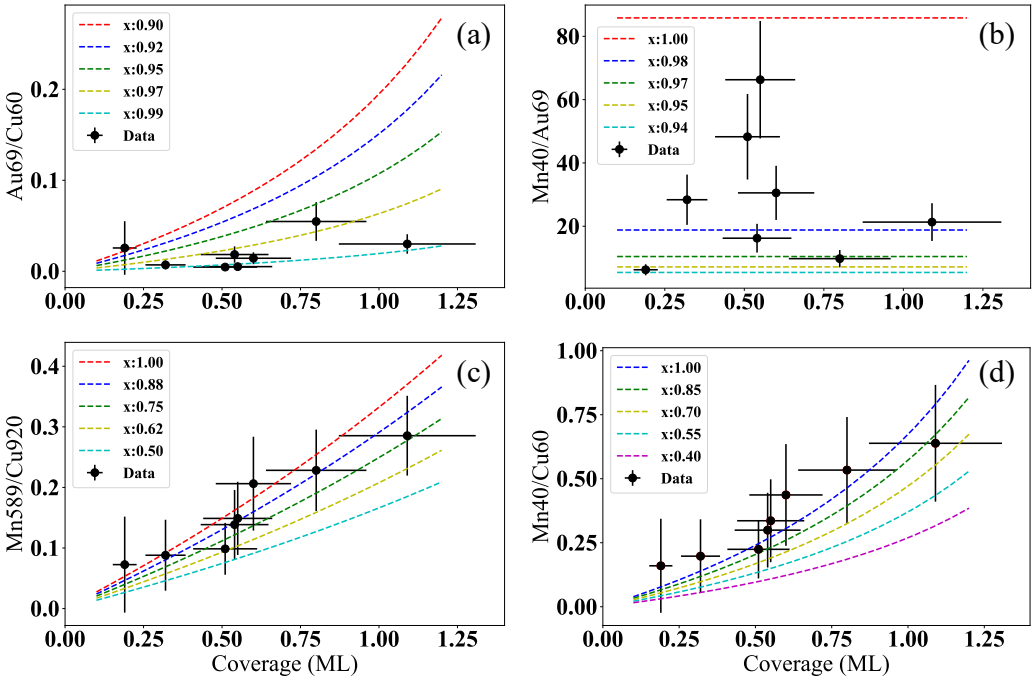

Figure 5.3: Using Eq. 5.1 for obtaining the x and $(1-x)$ for the Mn_xAu_{1-x} alloy. The graphs are plotted for Auger ratio vs. film coverage. The plots are for (a) Au69/Cu60, (b) Mn40/Au69, (c) Mn589/Cu920, and (d) Mn40/Cu60. The Auger ratios' error is calculated from the propagation of the errors in the determination of the peak heights.

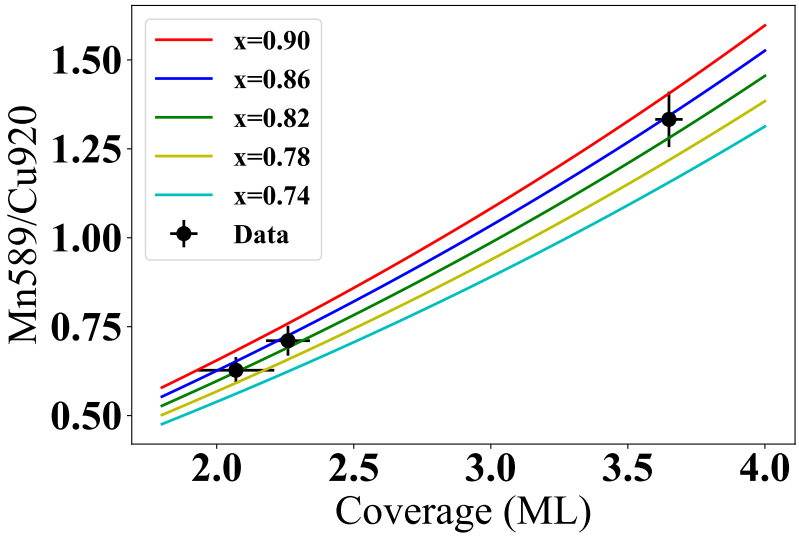

Figure 5.4: Using Eq. 5.1a for obtaining the x (0.82, 0.84, 0.85) for Mn_xAu_{1-x}. The graph is plotted for Auger ratio (Mn589/Cu920) vs. film coverage. The Auger ratios' error is calculated from the propagation of the errors in the determination of the peak heights.

In Fig. 5.3, we plot the ratios of the Auger electron transitions vs. sample thicknesses for sub-ML Mn_xAu_{1-x} on Cu(001) for Au (69 eV)/Cu (60 eV), Mn (40 eV)/ Au (69 eV), Mn (589 eV)/Cu (920 eV) and, Cu (40 eV)/Cu (60 eV). We fit the AES result for the sub-ML Mn_xAu_{1-x} on Cu(001) as shown in Fig. 5.3 by using the Eq. 5.1a to define the x. The fitting parameters (λ, S (sensitivity factor) for related energy) are summarized in Tab. 5.1. It is clear that the ratio increases with film coverage. For the Mn (40 eV) Auger transition, determination of the peak height is not straightforward because another peak from the substrate is close in energy (can be seen in Fig. 5.2). This peak also contributes at the energy of the Mn peak (40 eV); therefore at low coverage Mn (40 eV) seems to be higher and then decreases with increasing coverage. However, from a certain thickness, the effect of this peak can be ignored. We can see that the Cu (60 eV) peak is not seen for coverages of 0.8 and 1 ML. Their AES spectra and AES ratios are shown in Fig. 5.2 and Fig. 5.3, respectively. The Cu (LMM) and Mn (LMM) Auger peaks are not overlapping with any other material Auger peaks that are used in this work. We can see the appearance and increase of Mn (LMM) and Mn (40 eV) in Fig. 5.2, in which the AES spectra are plotted in an ascending way (for film coverage). We find values for x from 0.5 to 0.9. This means we have Mn-rich samples. The average growth time per ML is around 60 s ($\pm$ 20 s) Mn_xAu_{1-x}. Besides the sub-ML regime, we also studied thicker Mn_xAu_{1-x} films grown on Cu(001). We show the AES spectra of (2.07 ± 0.14), (2.26 ± 0.08), and (3.65 ± 0.05) ML of $Mn_{0.82}Au_{0.18}$, $Mn_{0.84}Au_{0.16}$, and $Mn_{0.85}Au_{0.15}$, respectively, in Fig. 5.4.

In Fig. 5.5, we grew (2.07 ± 0.14) ML $Mn_{0.82}Au_{0.18}$ on Cu(001) and did the AES for as-grown and after post-annealing around 440 K for 5 min. What we observed is that after post-annealing, the sample oxidized a little. The oxidation for the sample can be seen from O (503 eV) peak, which is clearly visible for the AES spectrum after post-annealing but not for as-grown as shown in Fig. 5.5. We also observed that the Mn (40 eV)/Cu (60 eV), Au (69 eV)/Cu (60 eV), Mn (40 eV)/Au (69 eV) and Mn (589 eV)/Cu (920 eV) Auger transitions peak height ratio decreases. These

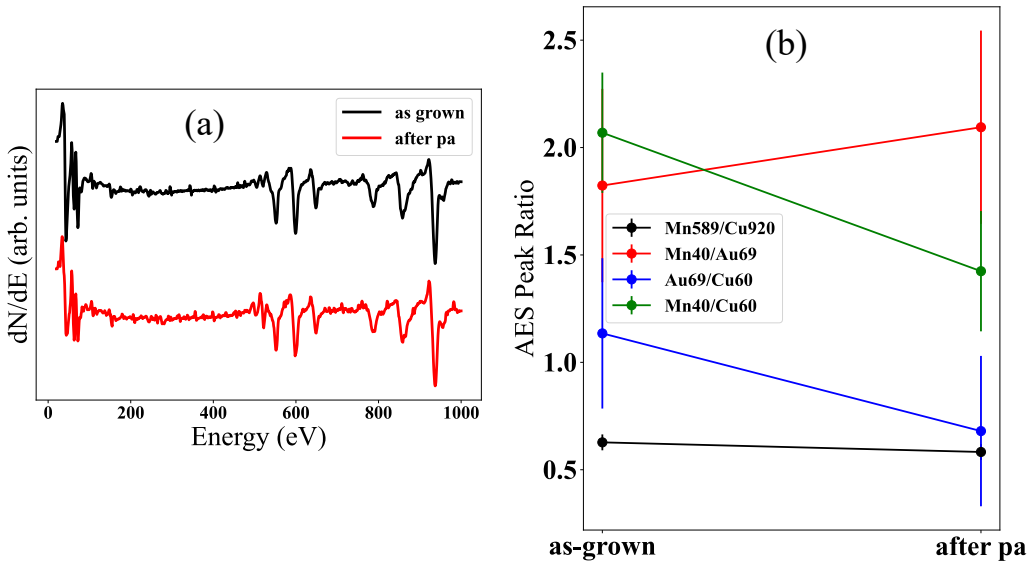

Figure 5.5: (a) AES survey spectrum of 2.07 ML Mn_xAu_{1-x} on Cu(001) for as-grown and after post-annealing. (b) The Auger peak height ratio is shown before and after post-annealing. The Auger ratios' error is calculated from the propagation of the errors in the determination of the peak heights.

decrements in the peak height ratios can be due to either Mn and Au diffusion or Cu segregation. From the increment in Mn (40 eV)/Au (69 eV) peak height ratio, we can deduce that the Au diffuses more than Mn. We also can see a slight increment in the Cu (920 eV)/Mn (589 eV) peak height ratio, and this also confirms the Cu segregation. The less diffusion in the Mn might be due to oxidation.

5.4 STM Results

The samples' morphology is checked by STM; for this, the samples are transferred to the STM without breaking the vacuum. The samples are scanned in constant-current tunneling (CCT) mode by an Fe-ring tip at room temperature [48].

To understand the growth morphology of co-deposited Mn-Au film on Cu(001), we grow very low coverages from 0.2 ML to several ML thick films and different Mn and Au alloy ratios. In Fig. 5.6, we show the result for low coverages, 0.19, 0.32, 0.51, and 0.54 ML of Mn_xAu_{1-x} on Cu(001) for x 0.9, 1.0, 0.95, and 0.9, respectively. The growth starts with very small islands, which become bigger with increasing coverage. While the coverage increases, bigger islands coexist with the

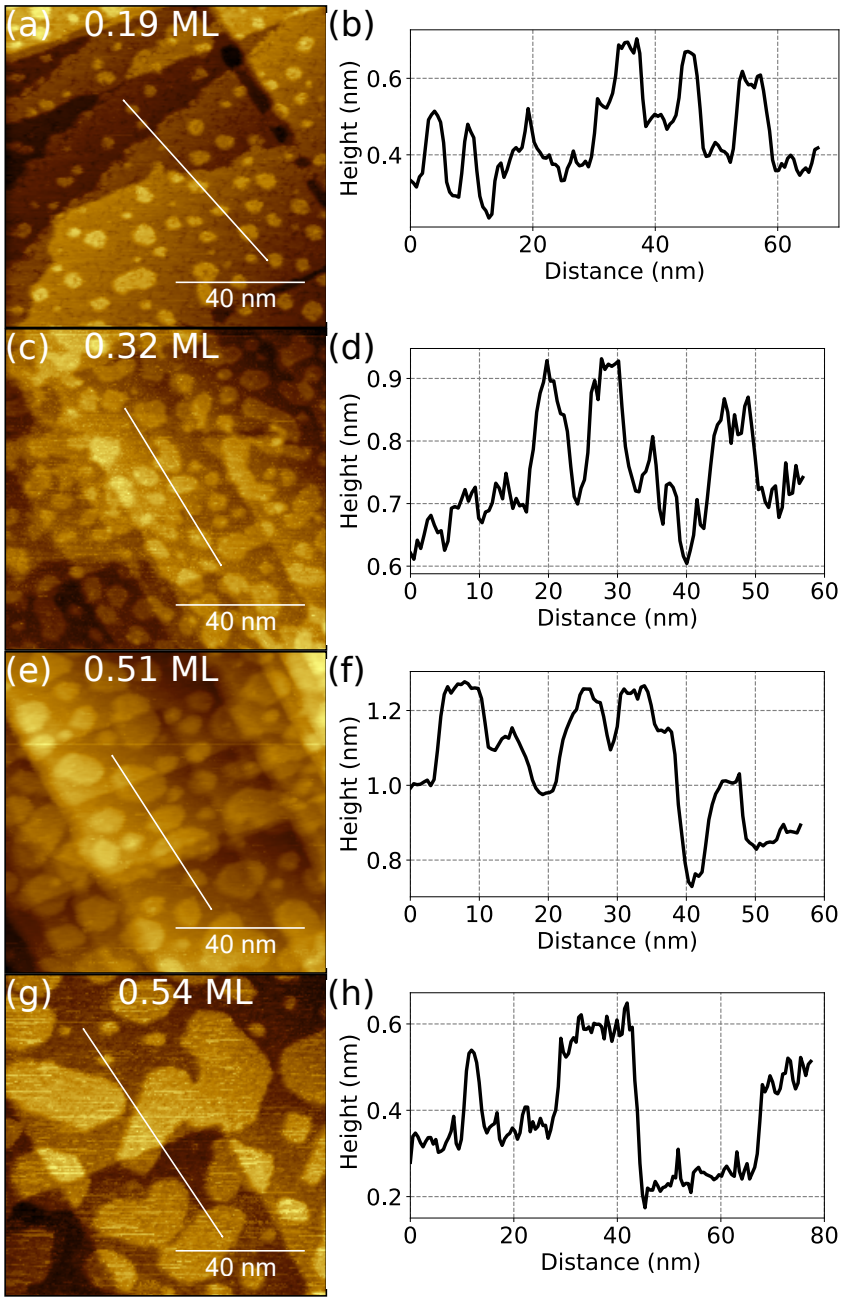

Figure 5.6: (a) STM topography images of (a) 0.19, (c) 0.32, (e) 0.51, and (g) 0.54 ML of Mn-Au alloy on Cu(001). STM feedback parameters for (a), (c), (e), and (g) are 1.15 nA×0.5 V, 1.18 nA×0.5 V, 1.19 nA×0.5 V, and 1.2 nA×0.5 V, respectively. (b), (d), (f), and (h) are line scans along the white lines in (a), (c), (e), and (g), respectively.

small islands. In the low coverages ($\leq$ 0.5 ML), the islands have round shapes. When these islands are merged, they are still round, but more elongated, which shows that two or more islands are merging. Fig. 5.7 shows STM topography images for 0.55, 0.6, 0.8, and 1.0 ML of Mn_xAu_{1-x} on Cu(001) for x 0.65, 1.0, 0.77, and 0.85, respectively. When the islands get bigger, they start to merge and finally cover the whole surface. For coverages $\geq$ 0.5 ML, the islands are round, but with increasing coverage, the round islands merge and create differently shaped islands, as seen in Fig. 5.7 (g).

We also prepared thicker ($>$ 1 ML) Mn_xAu_{1-x} films on Cu(001) for STM topography investigation. In Fig. 5.8 (a), 2.07 ML $Mn_{0.82}Au_{0.18}$ have been deposited on Cu(001) and post-annealed around 440 K ($\pm$20 K) for 5 min. This post-annealed sample as well as 3.65 ML $Mn_{0.85}Au_{0.15}$ (Fig. 5.8(e)) are rougher than 2.26 ML $Mn_{0.84}Au_{0.16}$ (Fig. 5.8 (c)). We do not have the STM topography for the as-grown 2.07 ML $Mn_{0.82}Au_{0.18}$ film; therefore, we cannot say what post-annealing causes to that sample. However, it is rougher than 2.26 ML $Mn_{0.84}Au_{0.16}$ (Fig. 5.8 (c)), which is very close in film thickness and concentration. Furthermore, the films thicker than 1 ML are not flat anymore, they are rougher than the thickness of the film for $\leq$ 1 ML.

Bommanaboyena et al. prepared 45 nm Mn_2Au(001) on 13 nm Ta(001)/ Al_2O_3(1–102) by MBE and rf magnetron sputtering. They investigated by the help of atomic force microscopy that the MBE-grown sample shows a smoother surface than rf magnetron-sputtering grown samples. They found that for annealing temperatures higher than 450 °C, Mn starts to desorb from the film, and this causes a change in the stoichiometry and crystallographic phase [116]. While up to now, nobody has studied Mn_2Au films grown on metallic single crystals, we tried it on single crystal Cu(001). Moreover, we grow the films with an electron beam evaporator. While Bommanaboyena et al. [116] prepared very thick samples, we could prepare a very thin film even below 1 ML. Compared to the work of Bommanaboyena et al. [116], we saw changes in the AES spectrum after

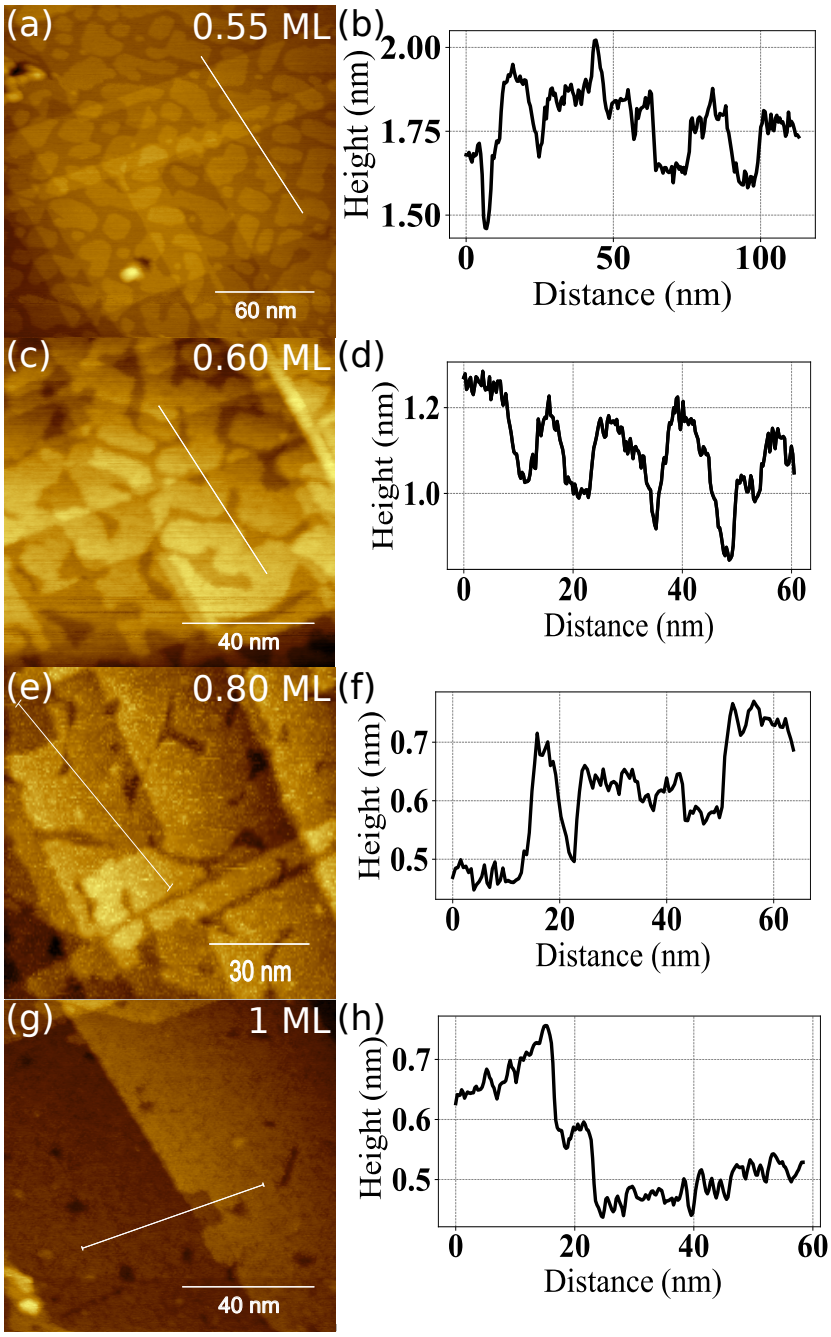

Figure 5.7: (a) STM topography images of (a) 0.55, (c) 0.6, (e) 0.8, and (g) 1 ML of Mn-Au alloy on Cu(001). STM feedback parameters for (a), (c), (e), and (g) are 1.19 nA×0.5 V, 1.14 nA×0.2 V, 1.16 nA×0.5 V, and 1.18 nA×0.2 V, respectively. (b), (d), (f), and (h) are line scans along the white lines in (a), (c), (e), and (g), respectively.

post-annealing around 440 K, as shown in Fig. 5.5.

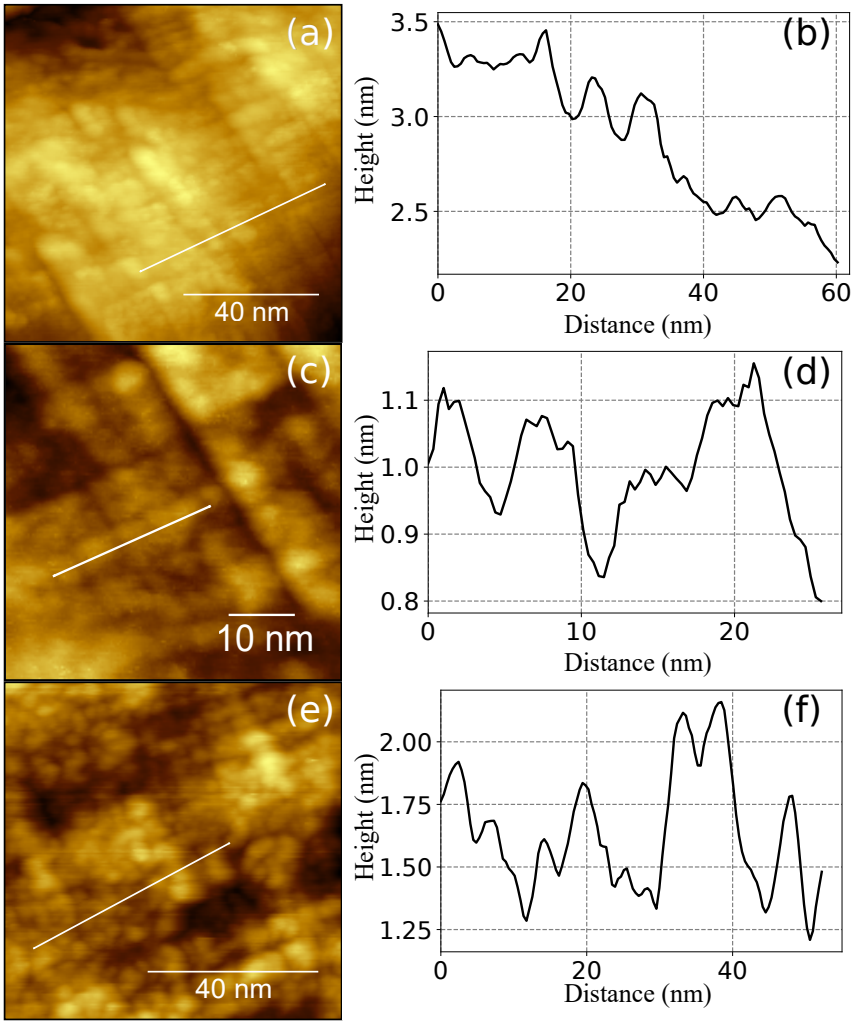

Figure 5.8: (a) STM topography images of (a) after post-annealing around 440 K for 5 min of 2.07 ML, (c) as-grown 2.26 ML, and (e) as-grown 3.65 ML of Mn-Au alloy on Cu(001). STM feedback parameters for (a), (c), and (e) are 0.48 nA×1 V, 1.18 nA×0.5 V, and 1.4 nA×0.5 V, respectively. (b), (d), and (f) are line scans along the white lines in (a), (c), and (e), respectively.

5.5 LEED Results

For studying the structure of the films for the initial growth of Mn_xAu_{1-x}, we employ LEED. In Fig. 5.9, we can see LEED images from 0.19 till 1 ML Mn_xAu_{1-x} on Cu(001). At very low coverage (0.19 ML), the substrate LEED pattern (p(1×1)) is very clear. Then the (01) spots get dimmer and disappear at around 0.5 ML. From 0.55 ML, we see another structure transition. The $(\frac{1}{2}\frac{1}{2})$ LEED spots become visible up to 1 ML. However, this c(2×2) superstructure does not exist in thicker films.

Fig. 5.10 (a) is for as grown 2.07 ML Mn_xAu_{1-x} on Cu(001). It is clear that there is no LEED pattern. After that we did a post-annealing around 440 K ($\pm$20 K) for 5 min. We did another LEED image at room temperature. The post-annealed sample barely shows the p(1$\times$1) substrate structure in Fig. 5.10 (b). To see the substrate structure after post-annealing can be explained by Mn and Au diffusion into the substrate as it was concluded from AES (Fig. 5.5). Fig. 5.10 (c) shows the LEED images for 2.26 ML Mn_xAu_{1-x} on Cu(001) at 180.4 eV. The LEED images in Fig. 5.9 and Figs. 5.10 (a) and (b) are done at 110 eV. However, for Fig. 5.10 (c), the energy is 180.4 eV because below that energy, there was no LEED pattern.

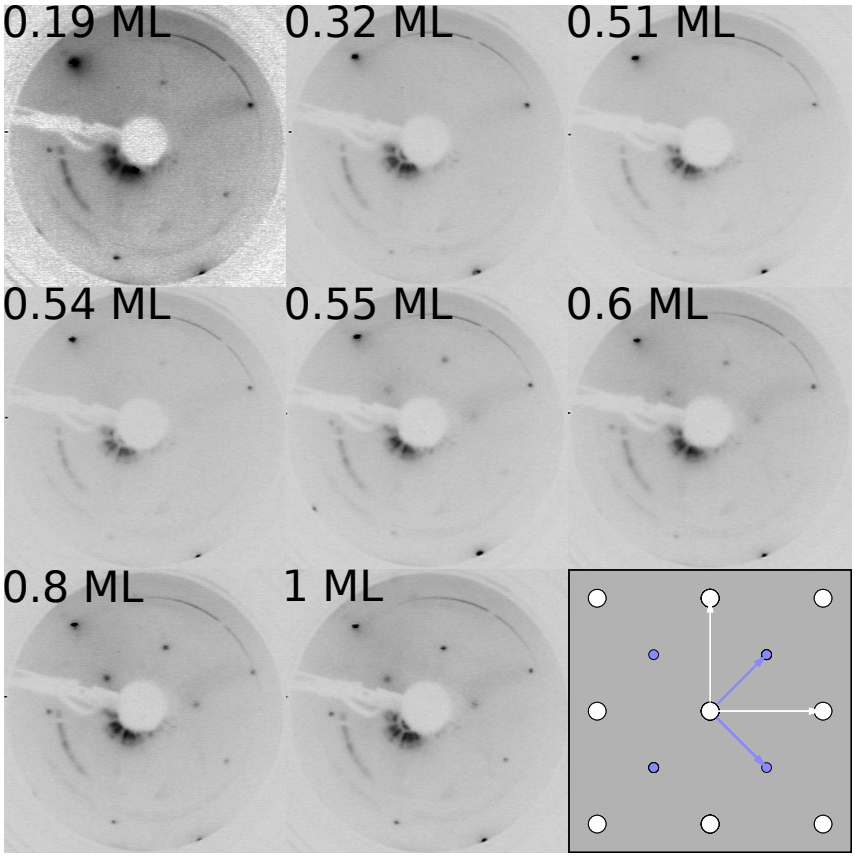

Figure 5.9: LEED images of Mn_xAu_{1-x} on Cu(001) for the same samples as in Figs. 5.6 and 5.7 at 110 eV. The bottom last LEED pattern is a simulation for the c(2$\times$2) superstructure by LEEDpat [117]. White and blue arrows show substrate and superstructure unit cell vectors, respectively.

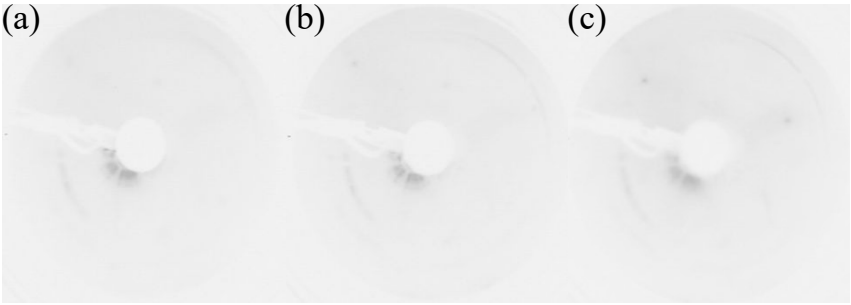

Figure 5.10: LEED images of 2.07 ML $Mn_{0.82}Au_{0.18}$ on Cu(001). (a) after growth, (b) after post-annealing (440 K for 5 min) at room temperature at 110 eV. (c) 2.26 ML $Mn_{0.84}Au_{0.16}$ on Cu(001) at 180.4 eV.

5.6 MEED Results

The growth of the samples is monitored by MEED. In Fig. 5.11, we see the MEED curves for the deposition of 2.07, 2.26, and 3.65 ML Mn_xAu_{1-x} on Cu(001). Even the MEED oscillations refer to layer-by-layer growth. We could detect LEED images around 1 ML and below it. The 0 on the x-axis shows where the shutter is opened. For the 3.65 ML films, we could calculate the thickness with less error than for the other two curves because of the multiple MEED oscillations. They are very periodic. The thickness calculation is done by getting the growth rate from the maximum and minimum peaks periodicity average. That is a sign of growth rate homogeneity for this sample.

In Tab. 5.2, we compare the results of thickness and Mn-Au ratio (x) for Mn_xAu_{1-x} on Cu(001). The sub-ML ($\leq$ 1 ML) coverages are analyzed by Gwyddion software from STM images. For the thick films, the thicknesses are evaluated from MEED oscillations. The x (Mn ratio in Mn_xAu_{1-x}) is extracted from AES.

MEED oscillations are usually interpreted as evidence of layer-by-layer growth. We see clear MEED oscillations for Mn_xAu_{1-x} on Cu(001), but we cannot see the LEED patterns. If we consider pure Mn films, they do not show oscillations when grown on Cu(001), because Mn grows in island mode on Cu(001) above 1 ML [47], but they exhibit clear MEED oscillations when grown on Cu_3Au [14, 118]. When we performed Mn-Au alloy growth on Cu(001), we observed strong MEED oscillations. We think that while Mn creates islands, Au might fill and cause the coales-

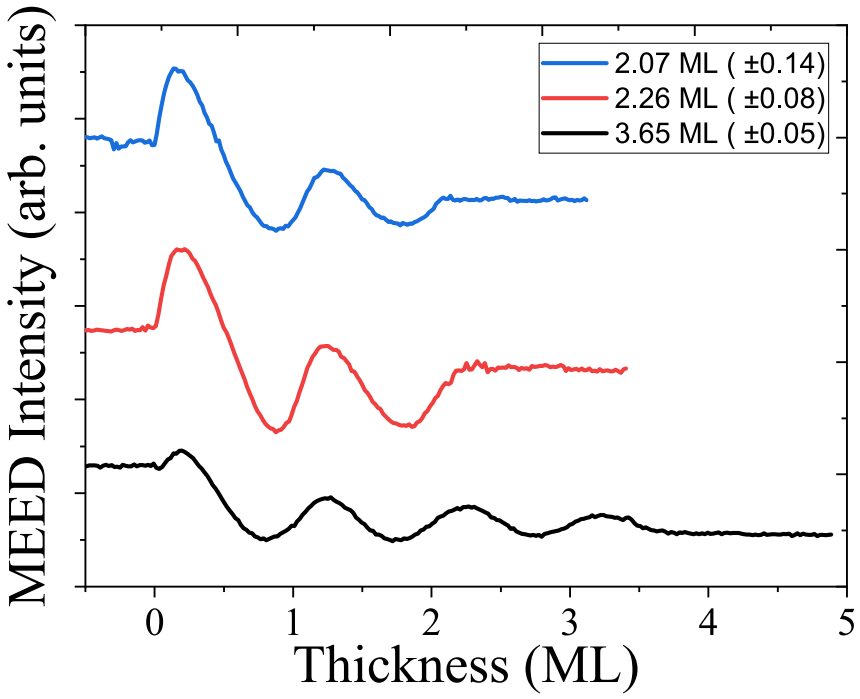

Figure 5.11: MEED specular (00)-spot intensity vs. time, calibrated in thickness for the deposition of 2.07, 2.26, and 3.65 ML Mn_xAu_{1-x} on Cu(001). The curves are shifted vertically for clarity.

Table 5.2: STM, AES, MEED, and LEED results comparison. Below 1 ML coverages are from STM, above they are from MEED oscillations. x is obtained from AES.

Sample	Coverage (ML)	x	LEED
Fig. 5.6(a)	0.19±0.02	0.90	1×1
Fig. 5.6(c)	0.32±0.04	1.00	1×1
Fig. 5.6(e)	0.51±0.07	0.95	1×1
Fig. 5.6(g)	0.54±0.08	0.90	1×1
Fig. 5.7(a)	0.55±0.08	0.65	c(2×2
Fig. 5.7(c)	0.60±0.09	1.00	c(2×2)
Fig. 5.7(e)	0.80±0.12	0.77	c(2×2)
Fig. 5.7(g)	1.08±0.16	0.85	c(2×2)
Fig. 5.8(a)	2.07±0.14	0.82	None
Fig. 5.8(c)	2.26±0.08	0.84	None
Fig. 5.7(e)	3.65±0.05	0.85	None

cence of these Mn islands to form a layer. Or, due to a locally random distribution of the much larger Au and smaller Mn atoms, this could lead to layer-by-layer growth. That the LEED pattern of Mn_xAu_{1-x} is missing could mean that the surface is laterally not long-range ordered enough to produce diffraction even if we are observing MEED oscillations.

5.7 Summary

We study the initial growth of Mn-Au alloys on Cu(001) at room temperature by STM, LEED, MEED, and AES. From the STM topography images, we investigate that in the sub-ML regime, the films create islands, and as the film's coverage increases, the islands start to merge to create big islands. The thicker films (above 1 ML), the surface becomes rough compared to 1 ML Mn_xAu_{1-x} on Cu(001). There are no clear LEED patterns for the thicker Mn-Au alloy on Cu(001) samples, even though there are clear MEED oscillations for thicker films. Our sample for the sub-ML regime shows the same LEED patterns as in the literature for sub-ML Mn on Cu(001) [31]. In the case of Au on Cu(001), it shows c(2×2) around 0.5 ML, above that, turns hexagonal [109, 30]. This could be due to the high Mn concentration in our Mn_xAu_{1-x} thin films. Au-rich Mn_xAu_{1-x} structures also can be studied to investigate further. The magnetic property of Mn in Mn-Au alloy on Cu(001) might be interesting to study.

CHAPTER 6

Co/Mn_xAu_{1-x} Bilayer Growth on Cu(001)

We discussed in the previous chapter the initial growth of Mn_xAu_{1-x} on Cu(001). In this chapter, we study the Co/Mn_xAu_{1-x} bilayer growth on Cu(001) by MEED, LEED, and AES to investigate it chemically and structurally. The magnetic behaviour of the samples is studied by MOKE.

6.1 Co/Mn_xAu_{1-x} Growth on Cu(001)

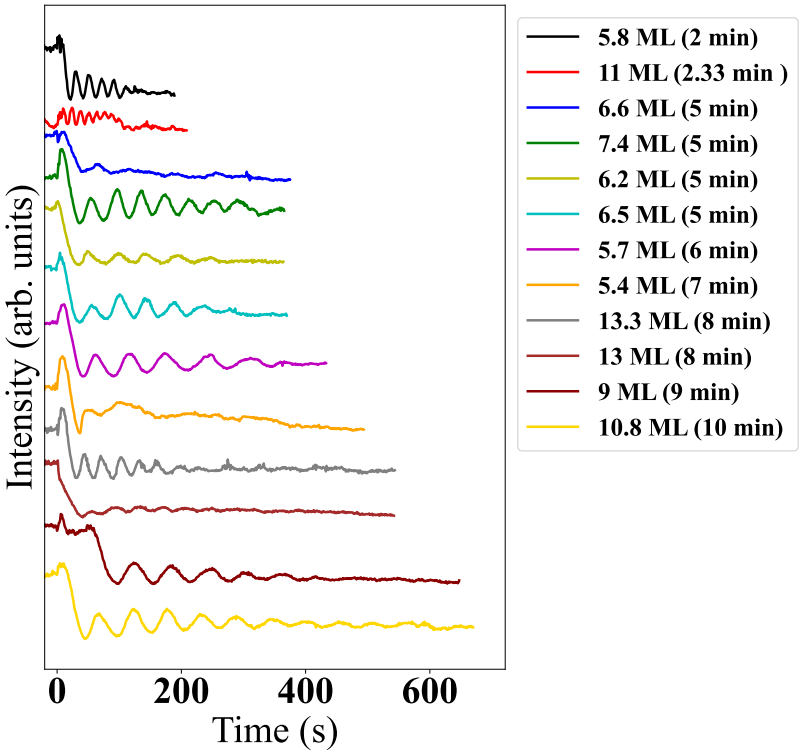

Figure 6.1: MEED intensity curves of Mn_xAu_{1-x} films (from 5.8 to 13.3 ML) on Cu(001). The shutter opened at time 0 and closed at the time mentioned in the legend. x for these samples are shown in Tab. 6.1.

The single crystal and thin films are prepared as mentioned in Chapter 5. We study Co and Mn_xAu_{1-x} bilayer grown on Cu(001) at room temperature in UHV. The Co film is grown layer-by-layer on Cu(001) and Mn grows layer-by-layer on

Co/Cu(001) [36]. Mn does not grow layer-by-layer directly on Cu(001). However, Mn_xAu_{1-x} grows layer-by-layer on Cu(001), at least for x from 0.39 to 0.95, as investigated here. In this work, Co is used as an FM layer to study the magnetic properties of Mn_xAu_{1-x}.

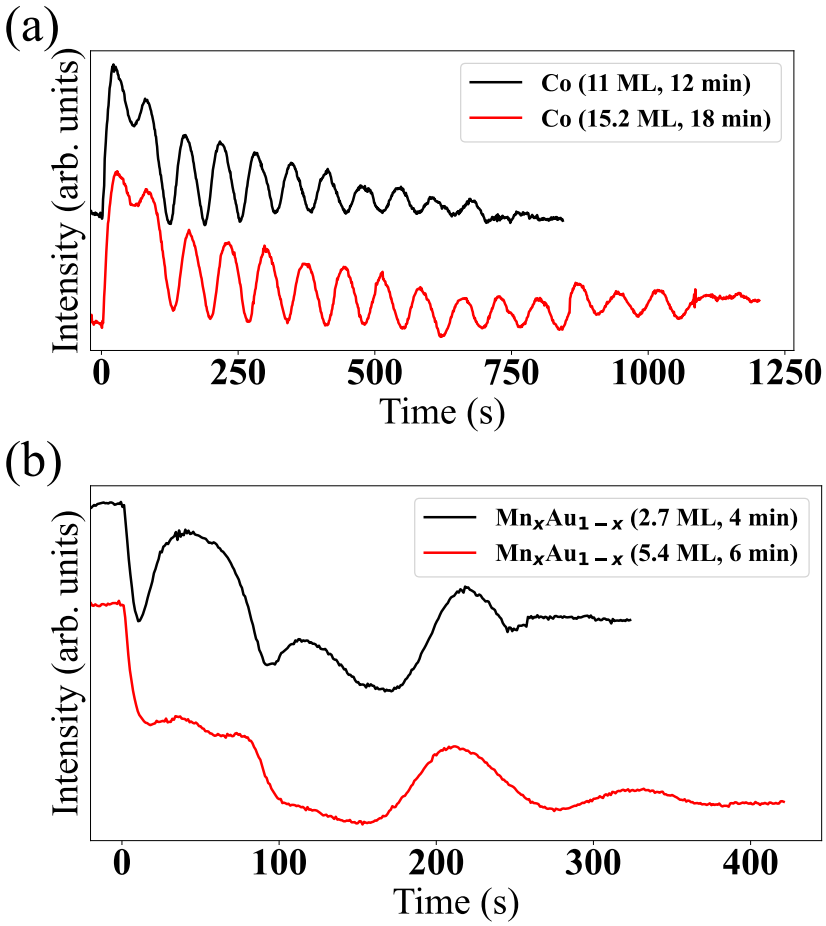

Figure 6.2: MEED intensity curves of (a) 11 and 15.2 ML Co on Cu(001). MEED intensity curves of (b) 2.7 ML $Mn_{0.81}Au_{0.19}$ and 5.4 ML $Mn_{0.72}Au_{0.28}$, grown on 11 and 15.2 ML Co/Cu(001), respectively. The shutter opened at time 0 and closed at the time mentioned in the legend.

In Fig. 6.1, we plot the MEED curves of Mn-Au alloys on Cu(001). From 5.4 to 13.3 ML, Mn_xAu_{1-x} thin-films are displaying MEED oscillations for different Mn-Au alloy ratios (x values are from 0.39 to 0.95), as tabulated in Tab. 6.1. And we also tried to grow Mn_xAu_{1-x} on Co/Cu(001) (Fig. 6.2), where we obtain MEED oscillations for these two samples, too. For Co, it was already known that it shows MEED oscillations on Cu(001), even Mn shows MEED oscillations on Co/Cu(001) [36]. Because we performed the MOKE measurements in another cham-

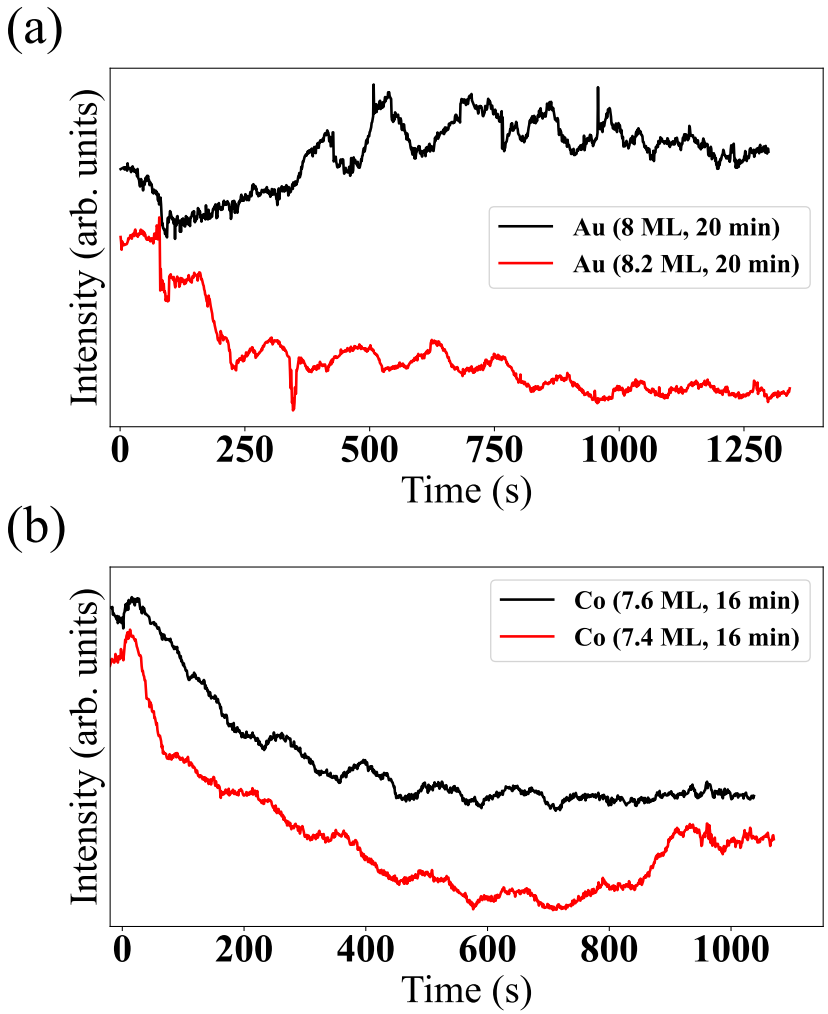

Figure 6.3: MEED intensity curves of (a) 8 and 8.2 ML Au on Co (7.6 ML)/ $Mn_{0.77}Au_{0.23}$ (6.5 ML)/Cu(001) and Co (7.4 ML)/$Mn_{0.72}Au_{0.28}$ (10.8 ML)/ Cu(001), respectively. MEED intensity curves of (b) 7.6 and 7.4 ML Co on $Mn_{0.77}Au_{0.23}$ (6.5 ML)/Cu(001), $Mn_{0.72}Au_{0.28}$ (10.8 ML)/Cu(001), respectively. The shutter opened at time 0 and closed at the time mentioned in the legend.

ber, we capped the sample by Au to prevent oxidation. While capping the bilayer films by Au, we observed MEED oscillations for Au on $Co/Mn_xAu_{1-x}/Cu(001)$, as shown in Fig. 6.3 (a). In Fig. 6.4 (a) and (c), we show LEED images for 11 and 15.2 ML Co grown on Cu(001), respectively, at 117 eV. The LEED images in Fig. 6.4 (b) and (d) are for $Mn_{0.81}Au_{0.19}$ (2.7 ML)/Co (11 ML) and $Mn_{0.72}Au_{0.28}$ (5.4 ML)/Co (15.2 ML), respectively, at 117 eV. 11 and 15.2 ML Co grown on Cu(001) show a clear p(1×1) pattern. When 2.7 ML $Mn_{0.81}Au_{0.19}$ is grown on Co (11 ML)/Cu(001), in Fig. 6.4 (a), and 5.4 ML $Mn_{0.72}Au_{0.28}$ is grown on Co (15.2 ML)/Cu(001), in Fig. 6.4 (c), there is no clear LEED pattern anymore. In another work, we start to grow Mn_xAu_{1-x} (6.2 ML) on Cu(001) and then grow Co (7.6 ML) on top, as shown in Fig. 6.5 (a) and (b). Unfortunately, there are no LEED patterns observed at beam energy 135 eV.

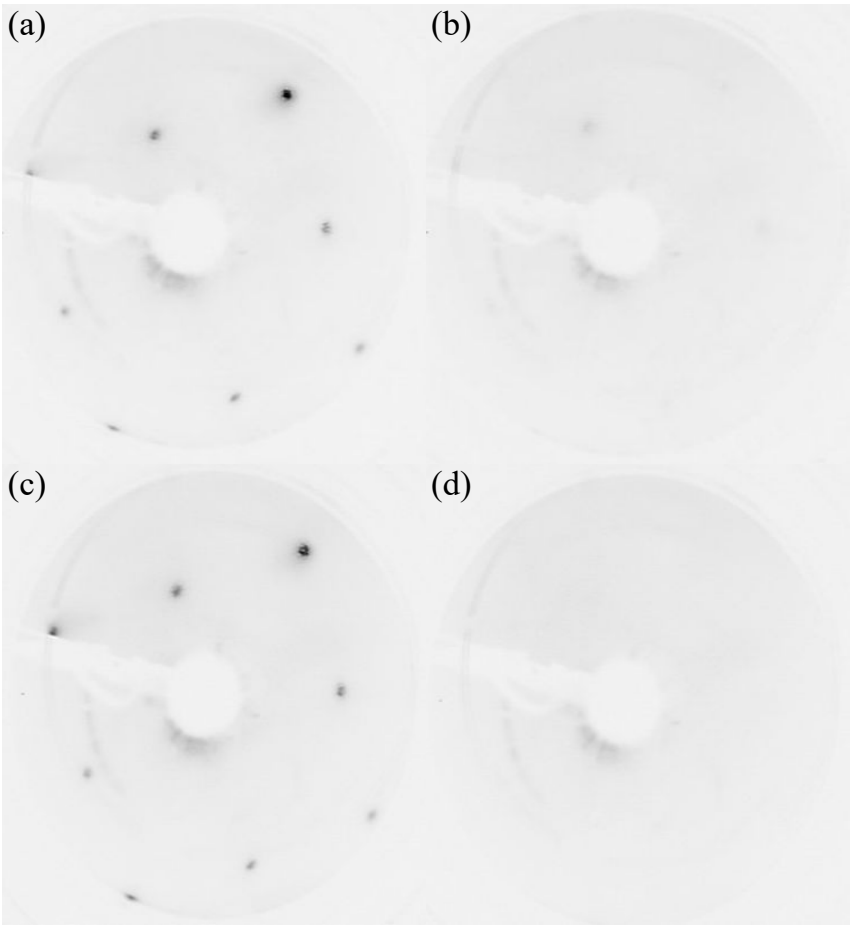

Figure 6.4: LEED patterns of (a) 11 and (c) 15.2 ML Co thin films on Cu(001) at 117 eV. LEED patterns of (b) 2.7 and (d) 5.4 ML Mn_xAu_{1-x} grown on 11 and 15.2 ML Co/Cu(001), respectively, at 117 eV.

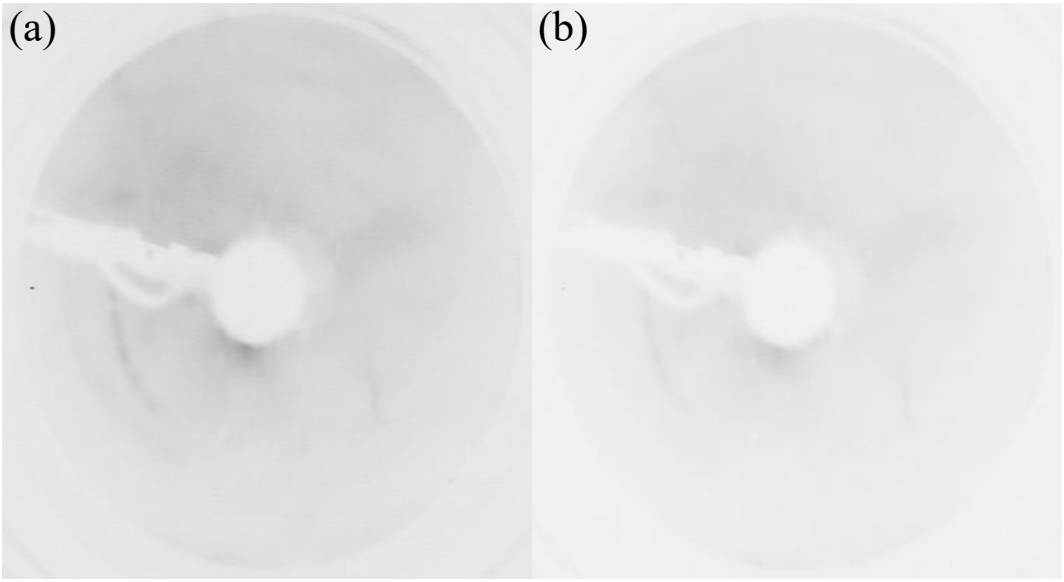

Figure 6.5: LEED patterns of (a) 6.2 ML $Mn_{0.83}Au_{0.17}$ on Cu(001), (b) 7.6 ML Co on $Mn_{0.83}Au_{0.17}$ (6.2 ML) at 135 eV.

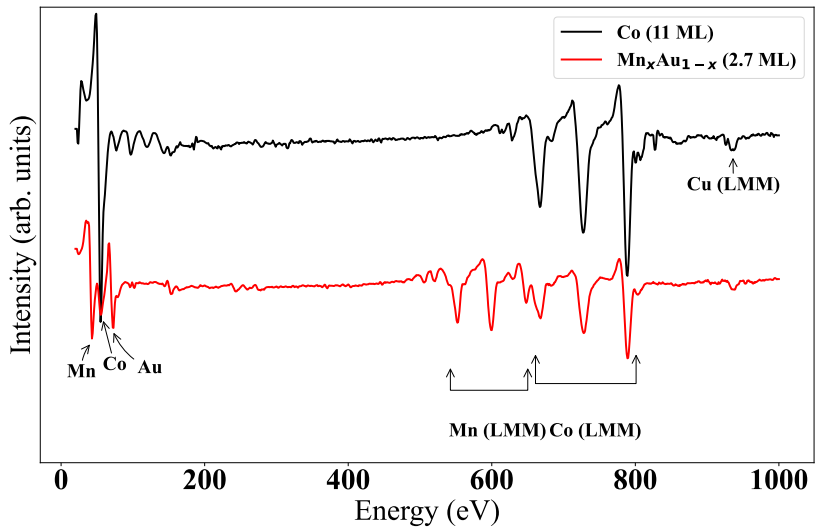

Figure 6.6: AES spectra of 11 ML Co/Cu(001) (black curve) and 2.7 ML $Mn_{0.81}Au_{0.19}$/Co(15.2 ML)/Cu(001) (red curve).

This study involves Mn, Co, and Au. To ensure the presence of these materials in the grown films, we employed AES. We show AES spectra in Fig. 6.6. We can see the Auger transitions of these three materials. The x in Mn_xAu_{1-x} is calculated by Auger exponential decay functions. For the Mn-Au alloy, we use either the Cu(920 eV)/Mn(589 eV) the or Mn(40 eV)/Au(69 eV) Auger peak height ratios. Values for x as obtained in both ways are shown in Tab. 6.1. The AES and curves of the Auger peak ratios can be seen in Fig. B.1, B.2, B.3, B.4, and B.5 of appendix B. We obtained x values from 0.38 to 0.95 from the Cu(920 eV)/Mn(589 eV) Auger peak height ratio. The x which is obtained from Mn(40 eV)/Au(69 eV) is different from the one obtained from Cu(920 eV)/Mn(589 eV). That can be due to the IMFP of Au 69 eV, which is smaller than the one of Mn(589 eV) and Cu(920 eV). If the growth rate of Au varies during deposition, the x can be different for both evaluations.

In this work, we study the growth of Mn_xAu_{1-x} on Cu(001). We investigate that the Mn_xAu_{1-x} grows layer-by-layer on Cu(001) and on Co/Cu(001), as displayed in Figs. 6.1 and 6.2 (b), respectively. While Co grows layer-by-layer on Cu(001), Co grows layer-by-layer on MnAu, too, as shown in Fig. 6.3 (b). The Au also shows MEED oscillations on Co/Mn_xAu_{1-x}/Cu(001), as shown in Fig. 6.3 (a). The MEED intensity reached its first maximum before the first completion of a monolayer for Co/Cu(001) and Mn_xAu_{1-x}/Cu(001), as shown in Figs. 6.1 and 6.2 (b), respectively. This can be due to either a non-perfect surface of Cu(001) [100] or anti-Bragg diffraction [119]. Another possible explanation for why the MEED oscillations start from high intensity can be due to the setting (azimuthal angle) of the single crystal. There is no LEED pattern for Mn_xAu_{1-x} samples neither on Cu(001) nor on Co/Cu(001), as shown in Fig. 6.5 (a) and 6.5 (b), respectively, while Co displays a p(1×1) LEED pattern. There is no LEED pattern for Co grown on Mn_xAu_{1-x}/Cu(001), too, as shown in Fig. 6.6 (b).

The MEED oscillations might not necessarily demonstrate layer-by-layer growth, as mentioned in the works of Li et al. [120]. For example, Evans et al.

explained that RHEED oscillations are based on "downward funneling" [121]. In their simulation, they show that the intensity oscillations may also occur in the absence of layer-by-layer growth when the diffusion of deposited atoms to lower layers is considered if they do not land on a perfectly horizontally flat place. However, the oscillations should still correspond to the deposition of monolayer amounts of material. We think that another possible reason for the absence of LEED patterns in the presence of MEED oscillations could be that a locally random distribution of the much larger Au and smaller Mn atoms could form layer-by-layer growth but that the surface is laterally not long-range-ordered enough to produce diffraction.

Table 6.1: Mn-Au alloy ratios obtained from Cu(920 eV)/Mn(589 eV) and Mn(40 eV)/Au(69 eV) Auger peak height ratios.

Thickness (ML)	x[a]	x[b]
5.7±0.2	0.77±0.09	0.66±0.02
5.8±0.2	0.39±0.05	0.53±0.01
6.2±0.2	0.83±0.1	0.83±0.02
6.5±0.2	0.77±0.09	0.75±0.02
6.6±0.2	0.95±0.1	0.82±0.01
6.8±0.2	0.69±0.08	0.69±0.02
7.4±0.2	0.70±0.08	0.71±0.02
9.0±0.2	0.69±0.07	0.67±0.01
10.8±0.2	0.72±0.07	0.68±0.02
13.0±0.2	0.62±0.06	0.76±0.01
13.3±0.2	0.64±0.06	0.74±0.02
16.8±0.2	-	0.54±0.02

[a] and [b] are for Cu(920 eV)/Mn(589 eV) and Mn(40 eV)/Au(69 eV), respectively.

6.2 L-MOKE of $Au/Co/Mn_xAu_{1-x}/Cu(001)$

The $Au/Co/Mn_xAu_{1-x}/Cu(001)$ samples' magnetic properties are studied by L-MOKE in another chamber. Therefore the samples were capped by Au to prevent oxidation during sample transfer to the other chamber. The samples are measured after zero-field cooling (ZFC) and field cooling (FC) by liquid nitrogen (LN_2). In Fig. 6.7, we show the H_C and H_{EB} results of five $Au/Co/Mn_xAu_{1-x}$/Cu(001) samples. In Fig. 6.7, the left figures are measured before the right figures. In Fig. 6.7

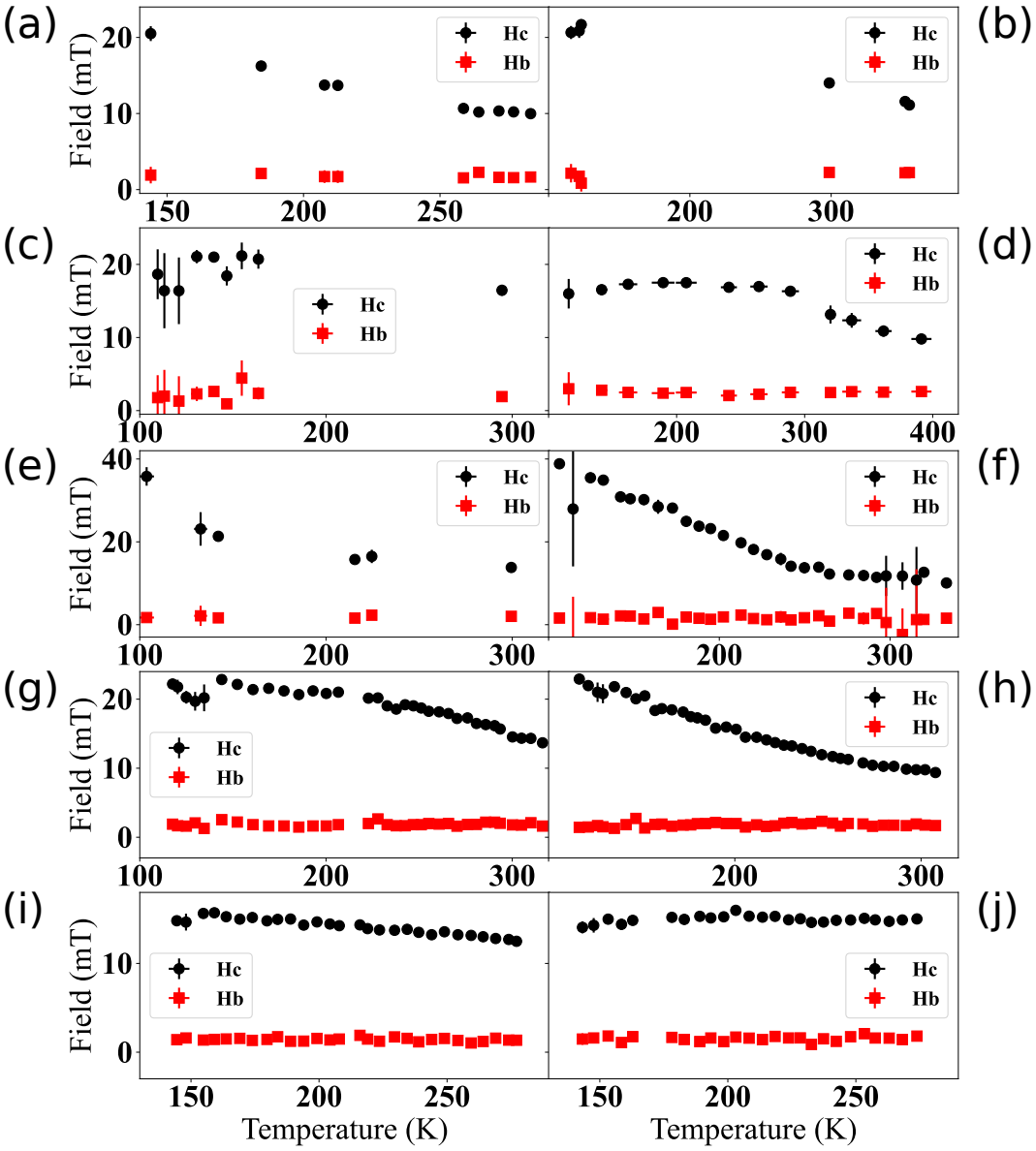

Figure 6.7: The results for H_C and H_{EB} from L-MOKE for (a) Au(8)/Co (7.6)/ $Mn_{0.77}Au_{0.23}$(6.5), (c) Au(7.2)/Co(7.5)/$Mn_{0.69}Au_{0.31}$(6.8), (e) Au(8.2)/Co(7.4)/ $Mn_{0.72}Au_{0.28}$(10.8), (g) Au(7.2)/Co(7.4)/$Mn_{0.64}Au_{0.36}$(13.3), (i) Au(14.4)/ Co(11.1)/$Mn_{0.62}Au_{0.38}$(13.0) on Cu(001). The number in brackets are the thicknesses in ML. (a), (c), (g), (i) are ZFC, and (b), (d), (h), (j) are FC after (a), (c), (g), (i), respectively. (e) and (f) are H_C and H_{EB} for the same sample after FC under the same conditions. FC under (b) −150 mT from 360 K, (d) −110 mT from 400 K, (e) −110 mT from 300 K, (f) −78 mT from 350 K, (h) 80 mT from 350 K, (j) 80 mT from RT. The systematic error in the field is around 2 mT. It is due to calibration of the field to zero. The data is binned for temperature.

.

(a) and (b), we display the H_C and H_{EB} for Au (8 ML)/Co (7.6 ML)/$Mn_{0.77}Au_{0.23}$ (6.5 ML)/Cu(001) for ZFC and FC, respectively. In Fig. 6.7 (a) ZFC from room temperature to around 140 K and (b) FC from 360 K to 115 K under −150 mT. In Fig. 6.7 (c) and (d), we display the H_C and H_{EB} for the Au (7.2 ML)/Co (7.5 ML)/ $Mn_{0.69}Au_{0.31}$ (6.8 ML)/Cu(001) for ZFC and FC, respectively. In Fig. 6.7 (c) ZFC from room temperature to around 110 K and (d) FC from 400 K to 110 K under −110 mT. In Fig. 6.7 (e) and (f), we display the H_C and H_{EB} for the Au (8.2 ML)/ Co (7.4 ML)/$Mn_{0.72}Au_{0.28}$ (10.8 ML)/Cu(001) for FC. In Fig. 6.7 (e) FC from room temperature to around 100 K under −110 mT and (f) FC from 350 K to 100 K under −78 mT. In Fig. 6.7 (g) and (h), we display the H_C and H_{EB} for the Au (7.2 ML)/Co (7.4 ML)/$Mn_{0.64}Au_{0.36}$ (13.3 ML)/Cu(001) for ZFC and FC. In Fig. 6.7 (g) ZFC from room temperature to around 110 K and (h) FC from 350 K to 110 K under 80 mT. In Fig. 6.7 (i) and (j), we display the H_C and H_{EB} for the Au (14.4 ML)/ Co (11.1 ML)/$Mn_{0.62}Au_{0.38}$ (13.0 ML)/Cu(001) for ZFC and FC. In Fig. 6.7(i) ZFC from room temperature to around 115 K and (j) FC from room temperature to 140 K under 80 mT. In all these samples, we did not observe any change in H_{EB} for different Mn-Au alloy and various Mn_xAu_{1-x} thicknesses with several Co thicknesses. We observe H_C as a function of temperature as shown in Fig. 6.7 for ZFC and FC measurements. There are no big changes in H_C remeasuring the sample for FC after the measurement of ZFC. We performed ZFC and FC to deduce the exchange coupling between AFM (Mn_xAu_{1-x}) and FM (Co). If there were an exchange coupling between FM and AFM, we could see changes in H_{EB}, but we could not see any changes, as displayed in Fig. 6.7. This could mean that the Mn_xAu_{1-x} alloy is not in an AFM phase or any other reasons such as a high T_N (T_N of Mn_2Au is very high above 1000 K [17]). Another possible reason could be that the samples have not been post-annealed to sufficiently high temperatures to form the alloy. Another reason might be that at the interface between Co and Mn_xAu_{1-x}, there is no AFM and FM coupling due to the Mn-Au alloy ratio because the Au-rich alloy has an FM phase. If we look deeper into the Mn-Au alloy, we find that there are several

AFM phases. The T_N of MnAu, $MnAu_2$, $MnAu_3$, Mn_3Au_5, and Mn_2Au are 365, 513, 140, 354, and 1600 K, respectively [16]. $MnAu_4$ is FM ($T_C \approx 373$ K) ([20]). Bommanaboyena et al. ([116]) compared the quality of MBE and sputtering-grown samples. The MBE sample is smoother than the sputtered one. They also found that post-annealing a sample above 450 °C, Mn starts to desorb from the films. They grew Mn_2Au on Ta/Al_2O_3. In the work of Sapozhnik et al., they grew Mn_2Au on an Al_2O_3 substrate at 600 °C ([97]), which is a very high temperature for our sample for post-annealing. In our samples, the films already start to diffuse into the substrate around 500 K. In another work, Wu et al. grew Mn_2Au on an MgO substrate at 200 °C and post-annealed at 200 °C for 1 h [96]. They studied the magnetic properties of an Mn_2Au/Fe bilayer, which shows a dependence of H_C and H_{EB} on the thickness with $1/t_{Fe}$ and with temperature increase. t_{Fe} is from 3 to 10 nm, the temperature range is from 300 to 5 K. Magnetic studies employed mostly bilayers of Mn_2Au/Fe. In those works compared to our work, they have thicker films of Mn_2Au and Fe. They measured the samples under a very high field and at a very low temperature to see the exchange bias and coercivity changes.

There can be various causes affecting the temperature dependence of exchange bias and coercivity, such as the size of AFM grains or the interface exchange coupling constants [122]. In the case of FM films, the coercivity changes with film thickness and temperature [123, 124]. The exchange bias originates from interfacial interactions between ferromagnetic and antiferromagnetic layers [9]. In the simple explanation of H_{EB} by Meiklejohn and Bean, simplified as in Eq. 6.1 [125],

$$\mu_0 H_{EB} = \frac{-JS_{AFM}S_{FM}}{M_{FM}t_{FM}} \tag{6.1}$$

$\mu_0 H_{EB}$ (exchange bias) depends on the interface coupling J, FM, and AFM interface magnetization S_{AFM}, S_{FM}, respectively. M_{FM} and t_{FM} are saturation magnetization and thickness of FM film [125]. From Eq. 6.1, we can see that the FM thickness and saturation magnetization play a crucial rule in H_{EB}.

The work of Zhou et al. shows the H_{EB} for Py (5 nm)/Mn_2Au (10 nm) bilayer

films at 20 K after FC at 10 kOe [126]. However, in the work of Jourdan et al., they did not observe any exchange bias shift (there is a negligible shift) for an Fe(5 nm) on Mn_2Au(7 nm) sample measured at temperatures at 300, 170, and 10 K. However, they observed clear coercivity changes for low temperatures (170 and 10 K) [27]. Bommanaboyena et al. performed SQUID for the sample of Mn_2Au (40 nm)/Py (2-10 nm) bilayer in which they did not observe exchange bias, but they show the coercivity decrease with Py thickness increase [87]. Bommanaboyena et al. also observed that H_C increased with increasing Mn_2Au layer thickness.

6.3 Summary

In the present work, we investigate the MEED oscillations for Mn_xAu_{1-x} on Cu(001) and Mn_xAu_{1-x} on Co/Cu(001) as well as for Co on Mn_xAu_{1-x}/Cu(001), which all show a layer-by-layer growth mode. However, no clear LEED patterns were observed for Mn_xAu_{1-x} on Cu(001) and Mn_xAu_{1-x} on Co/Cu(001). This absence of LEED patterns could be due to a missing long-range order of the film. The presence of MEED oscillations could be due to the Mn-Au alloy films' locally random distribution, which might form layer-by-layer growth. We also performed MOKE measurements of the hysteresis loops. The MOKE results of the bilayer Mn_xAu_{1-x}/Co samples do not show any exchange bias after FC for different x, and different Mn_xAu_{1-x} and Co thicknesses. The absence of exchange bias might be due to a low T_N. To create an ordered alloy, mostly post-annealing is necessary. However, we could not perform post-annealing because the post-annealing caused the diffusion of the films into the substrate. Post-annealing could be performed, but only up to a certain temperature, which might not be high enough to form the Mn-Au alloy.

CHAPTER 7

Fe/Mn_xAu_{1-x} Bilayer Growth on Ag(001)

In this work, we study the structure and magnetic properties of Fe and Mn_xAu_{1-x} on Ag(001). The structure of the films was monitored and analyzed by MEED, LEED, AES, and STM. The magnetic properties of the films were studied by L-MOKE.

7.1 Mn Growth on Ag(001)

The films' composition and thickness are analyzed by the help of MEED oscillations and AES. For the thickness calculation, we need the relative sensitivity factors of the Mn (589 eV) and Ag (356 eV) Auger transitions. For the calibration of the AES parameters for Mn on Ag(001), we start with growing Mn by electron beam evaporation on Ag(001) in UHV.

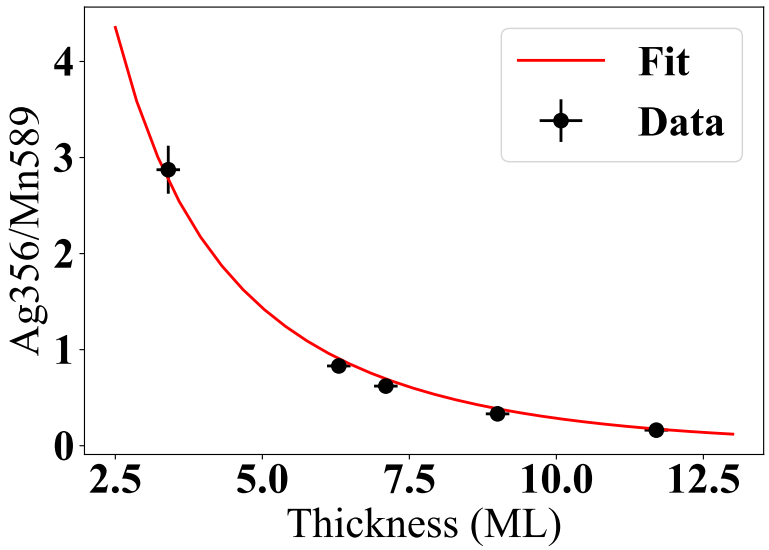

Figure 7.1: The exponential least square fit for Auger peak-to-peak height ratio (Ag_{356}/Mn_{589}) vs. thickness of Mn on Ag(001). The fit parameters are summarized in Tab. 7.1. The Auger ratios' error is calculated from the propagation of the errors in the determination of the peak heights.

In Fig. 7.2, we show two samples; the first one (Fig. 7.2 (b)) was prepared by

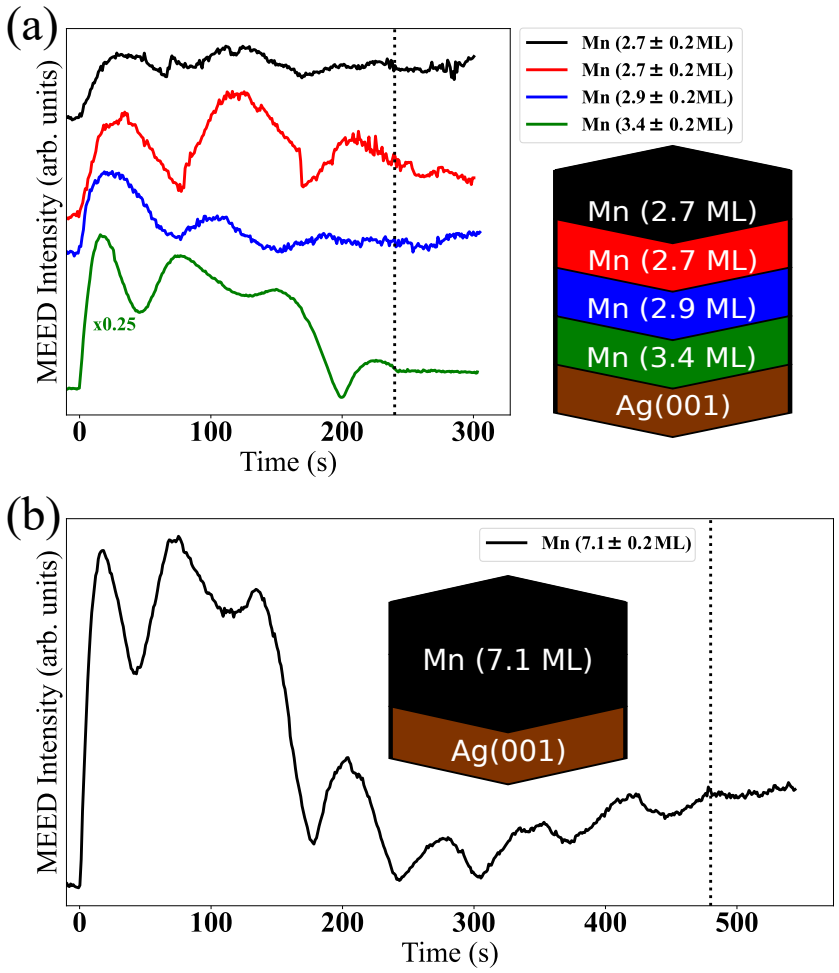

Figure 7.2: The MEED (00)-spot intensity oscillation curves of Mn on Ag(001) vs. time. (a) Starting from 3.4, additional 2.9, 2.7, and 2.7 ML Mn were grown on Ag(001) subsequently. The 3.4-ML Mn MEED curve multiplied by 0.25. (b) The MEED oscillation curves during the growth of 7.1 ML Mn on Ag(001). The detailed sample growth sketch of (a) and (b) are shown next to the figure and in inset, respectively. The shutter was opened at time 0 s and closed at the time defined by vertical dotted line.

Table 7.1: Auger exponential decay function parameters for Mn on Ag(001).

Auger Peak	S	λ (ML)
Mn(589 eV)	1.18* ($\pm$ 0.04)	4* ($\pm$ 0.15)
Ag(356 eV)	4.72 ($\pm$ 0.20)	3.67 ($\pm$ 0.15)

* S and λ are taken from Y. Shokr, Ph.D. thesis [115]. The λ for low energy is calculated.

continuously growing 7.1 ML Mn on the substrate, as monitored from the MEED oscillations. In the second sample as shown in Fig. 7.2 (a), we grew 3.4, 2.9, 2.7, and 2.7 ML Mn on Ag(001) subsequently. After each cycle, we acquired an AES spectrum. Using these films' thicknesses vs. their AES peaks height ratio and fitting with an exponential decay function, we could obtain the relative sensitivity factors S_{Ag356} and S_{Mn589}, which are 4.72 and 1.18, respectively. The effective λ_{356} is taken from the universal curve by an empirical equation in 2.3, which is taken from reference [38]. We consider the take-off angle in the Auger system as 42.3° and convert the IMFP to ML. The AES exponential decay function fitting is shown in Fig. 7.1 and its parameters are summarized in Tab. 7.1. Then the Mn AES fitting parameters can be used to define the x and thickness of Mn_xAu_{1-x} films grown on Ag(001).

From LEED-I(V), we can obtain the vertical interlayer spacing. The interlayer spacing for Mn films is smaller than the one of bulk Ag(001), as shown for different Mn thin films (from 3.4 to 11.7 ML) on Ag(001) in Fig. 7.3 (c). The vertical interlayer spacing of bulk fcc Ag(001) is 2.04 Å [127]. However, the Mn films' vertical interlayer spacing is smaller than the one of the bulk substrate. In Tab. 7.2, we list the interlayer distances for Mn grown on Ag(001), which are between 1.84 and 2.14 Å. The d_p, for 3.4 ML Mn on Ag(001) is 2.14 Å. This is higher than the substrate vertical interlayer spacing (2.08 Å). In the case of thick films, it is smaller (1.84-1.92 Å).

Table 7.2: LEED and LEED-I(V) (vertical interlayer spacing, d_p) results of Mn growth on Ag(001).

d (ML)	d_p(Å)	LEED
0	2.08±0.03	1×1
3.4±0.2	2.14±0.03	1×1
6.3±0.2	1.85±0.03	1×1
7.1±0.2	1.84±0.03	1×1
9.0±0.2	1.92±0.03	1×1
11.7±0.2	1.87±0.03	1×1

The Mn films grow epitaxially and layer-by-layer on Ag(001), as concluded

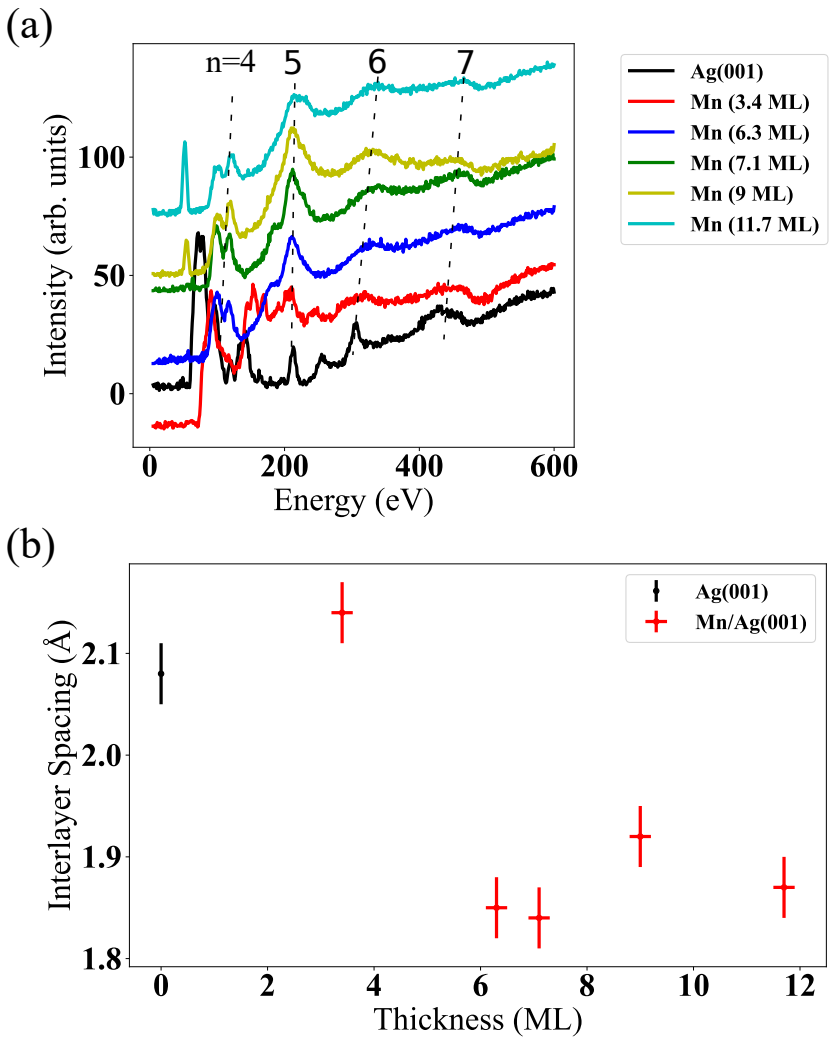

Figure 7.3: (a) LEED-I(V) and (b) vertical interlayer spacing for clean Ag(001), 3.4, 6.3, 7.1, 9.0, and 11.7 ML Mn films on Ag(001). Error bars are derived from least square fit.

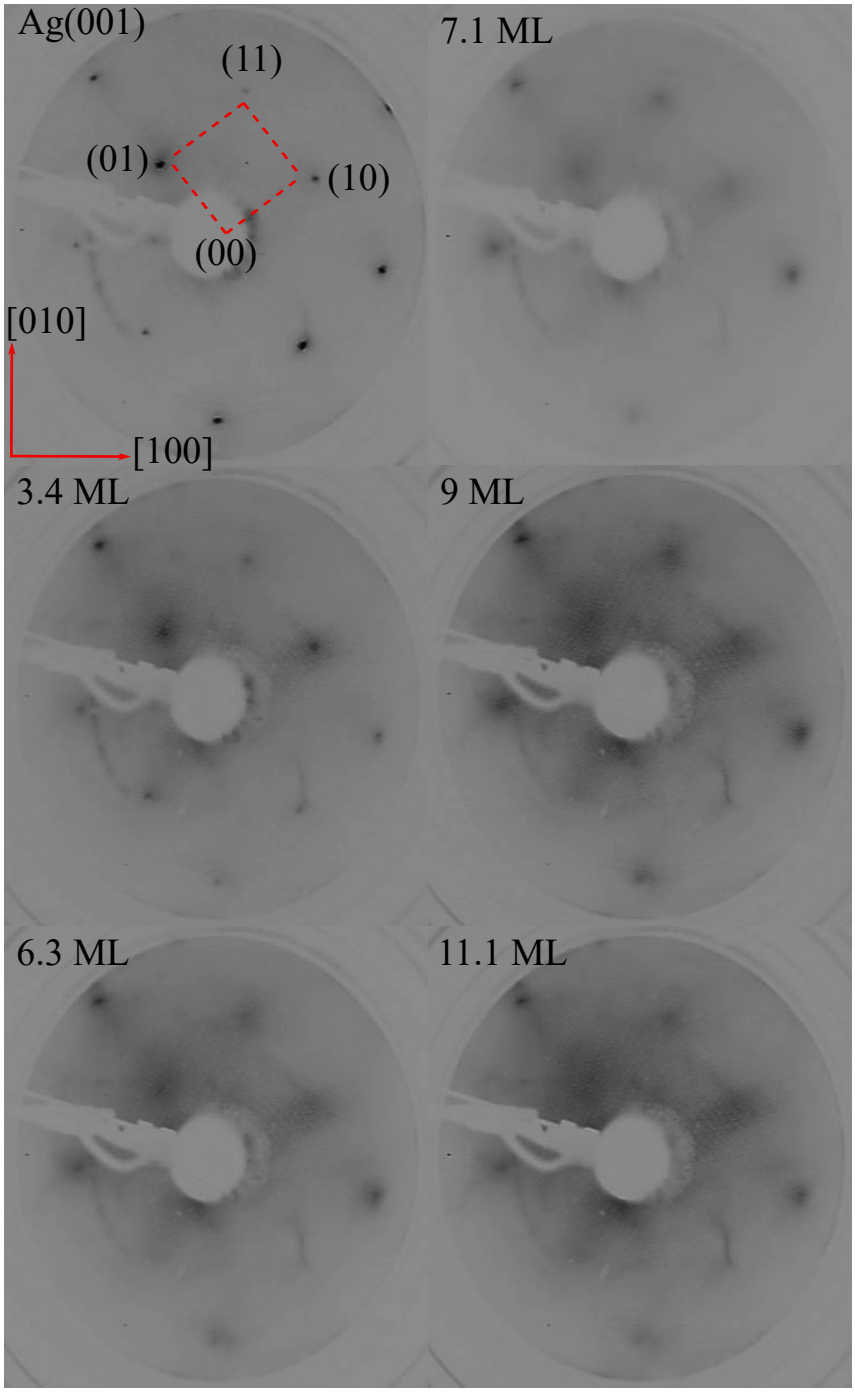

Figure 7.4: LEED patterns of clean Ag(001) and 3.4 to 11.7 ML Mn on Ag(001) at a beam energy of 135 eV.

from the MEED oscillations in Fig. 7.2 and the LEED patterns in Fig. 7.4. The LEED image of clean Ag(001) and for Mn films on the substrate of Ag(001) are shown in Fig. 7.4 at 135 eV. The epitaxial Mn thin films on Ag(001) exhibit a tetragonal structure for film thicknesses $\geq$ 5 ML [128]. The LEED image of clean single crystal Ag(001) shows sharp spots. After the deposition of Mn film on Ag(001), the LEED spots broaden with increasing coverage. But the positions of the spots do not change. A rough surface could cause dimmer and broadened spots. The results of LEED and LEED-I(V) are summarized in Tab. 7.2.

7.2 STM Investigation of Mn_xAu_{1-x} on Ag(001)

A $Mn_{0.83}Au_{0.17}$ film was grown on Ag(001) and analyzed in the preparation chamber. Afterward, the sample was transferred to the STM without vacuum breaking. The film was scanned in CCT mode by an Fe ring, as shown in Fig. 7.5 (a). Fig. 7.5 (c) is a line scan along the white line in Fig. 7.5 (a). 1.7 ML $Mn_{0.83}Au_{0.17}$ grown on Ag(001) displays a fully covered layer, islands, and holes in the STM topography image at RT. The LEED pattern of $Mn_{0.83}Au_{0.17}$ (1.7 ML) shows p(1$\times$1), see Fig. 7.5 (c). The x for Mn_xAu_{1-x} is calculated as 0.83 and 0.95 from the AES spectrum by using the peak intensity ratios of Ag356/Mn589 and Mn40/Au69, respectively. In the work of Bommanaboyena et al. [116], they compared the quality of Mn_2Au thin films grown by MBE and sputtering methods. They grew Mn_2Au (45 nm) on a Ta buffer layer on an Al_2O_3 substrate. They found that the MBE sample is smother than the one prepared by sputtering. Since we have a very thin Mn_xAu_{1-x} film on a single crystal, we have a very smooth surface compared to their samples.

7.3 Mn_xAu_{1-x} Growth on Ag(001) and the Influence of Post-annealing

In this part, we investigate the growth of Mn_xAu_{1-x} on Ag(001) by LEED-I(V) and compare as-grown samples and the effect of post-annealing for different thicknesses and Mn-Au ratios.

In Tab. 7.3, we can see the vertical interlayer spacing for the Mn_xAu_{1-x} sam-

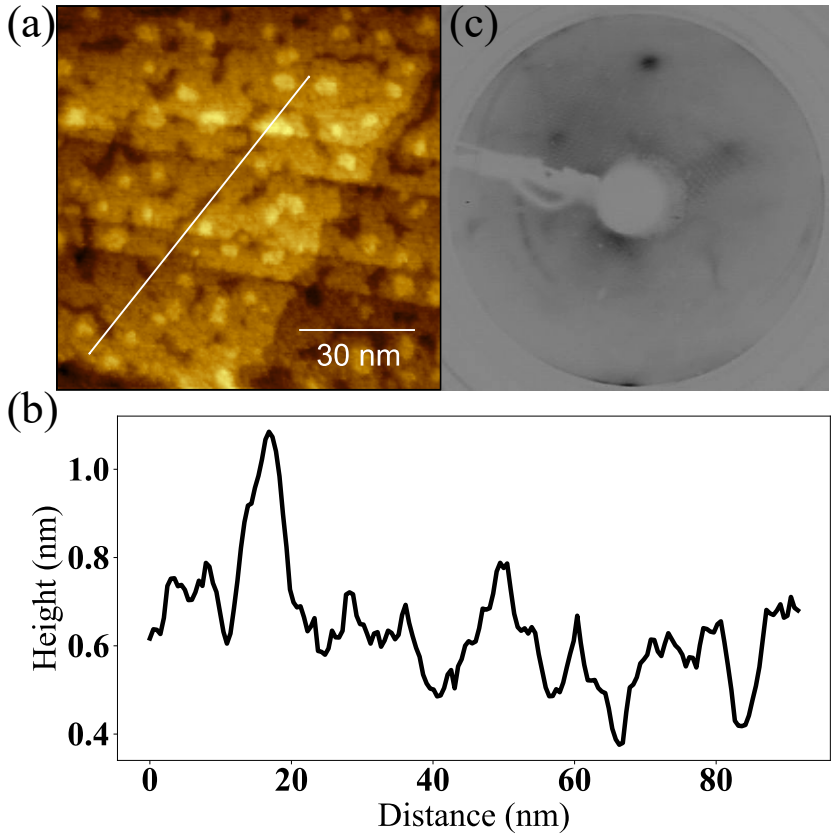

Figure 7.5: 1.7 ML $Mn_{0.83}Au_{0.17}$ grown on Ag(001), (a) STM topography image. STM feedback parameters 0.49 nA×1 V. (b) is a line scan along the white line in (a). (c) The LEED image at 90 eV.

ples as obtained from LEED-I(V). The d_p are in the range from 1.87 to 2.06 Å. The films' vertical interlayer spacings are thus in the range of the substrate bulk Ag(001) vertical interlayer spacing. Overall, the films' interlayer spacing is reduced compared to the substrate. In the case of post-annealed samples, the interlayer spacing is bigger, probably because, for higher temperatures, the films diffuse into the substrate. We can also observe the diffusion of films or segregation of substrate atoms to the surface in AES. In Fig. 7.6 (b), (d) and (f), after post-annealing around 600, 600, and 500 K, respectively, the Au (69 eV) and Mn (40 eV, 589 eV) Auger transitions vanish. However, the Ag (356 eV) Auger peak gets obviously bigger. On the other hand, if the sample oxidized even only very little, as in Fig. 7.6 (h), there is no diffusion or segregation. As displayed in Fig. 7.6 (h), AES spectra for as-grown and post-annealed 10.2 ML Mn_xAu_{1-x} on Ag(001) as well as their Ag356/ Mn589 peak height ratio (inset) do not change at all (change < 0.5 %). The oxy-

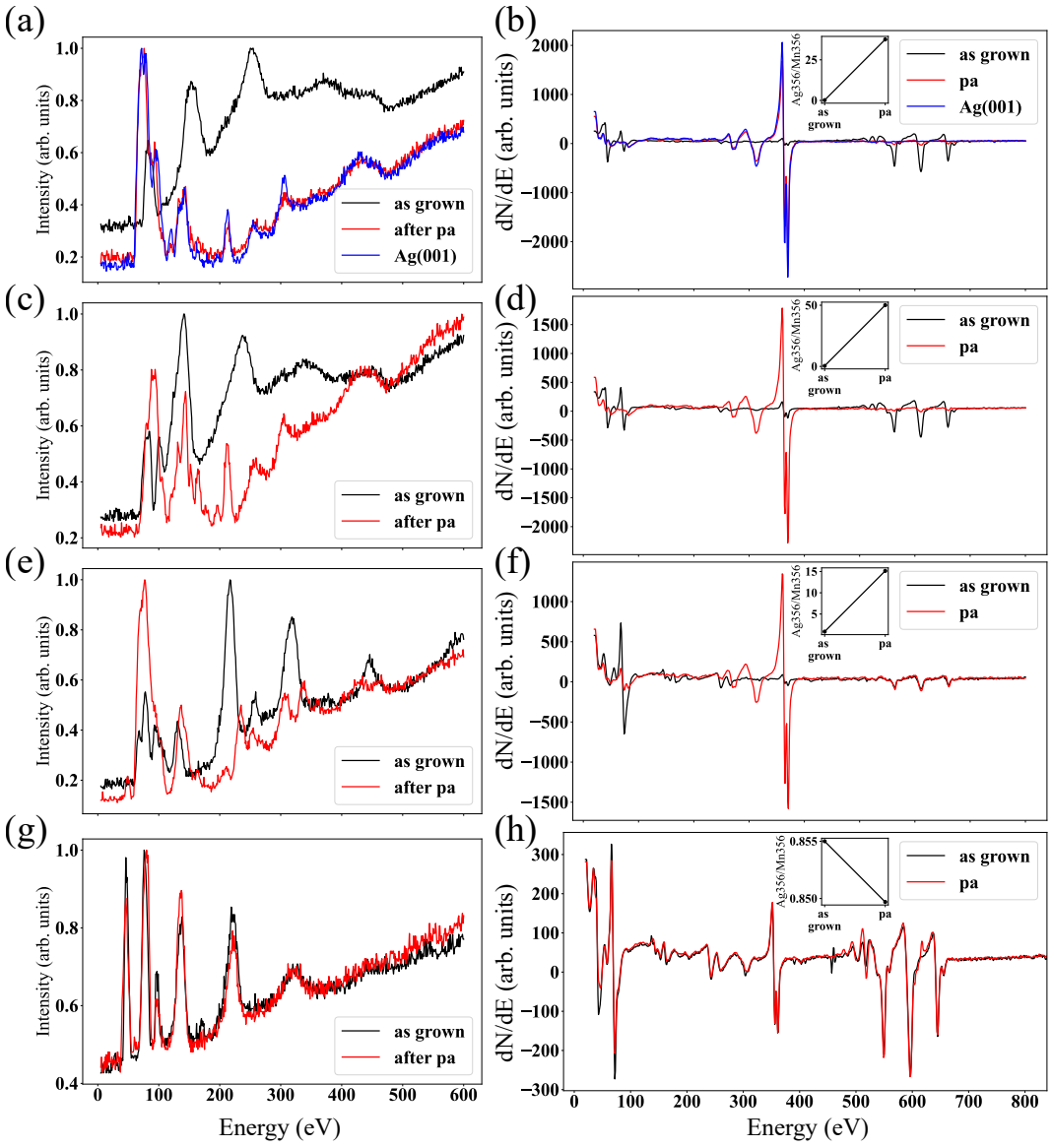

Figure 7.6: LEED-I(V) and AES of MnAu grown on Ag(001). LEED-I(V) of (a) clean Ag(001), 12.9 ML as-grown and after pa (600 K for 3 min), (c) 11.4 ML as-grown and after pa (600 K for 4 min), (e) 10.5 ML MnAu as-grown and after pa (500 K for 3 min), (g) 10.2 ML as-grown and after pa (480 K for 3 min). (b), (d), (f) and (h) are AES spectra of (a), (c), (e), and (g) for as-grown and after pa, respectively. Inset figures in (b), (d), (f) and (h) are the Auger ratio of Ag356/Mn589 for as-grown and after pa.

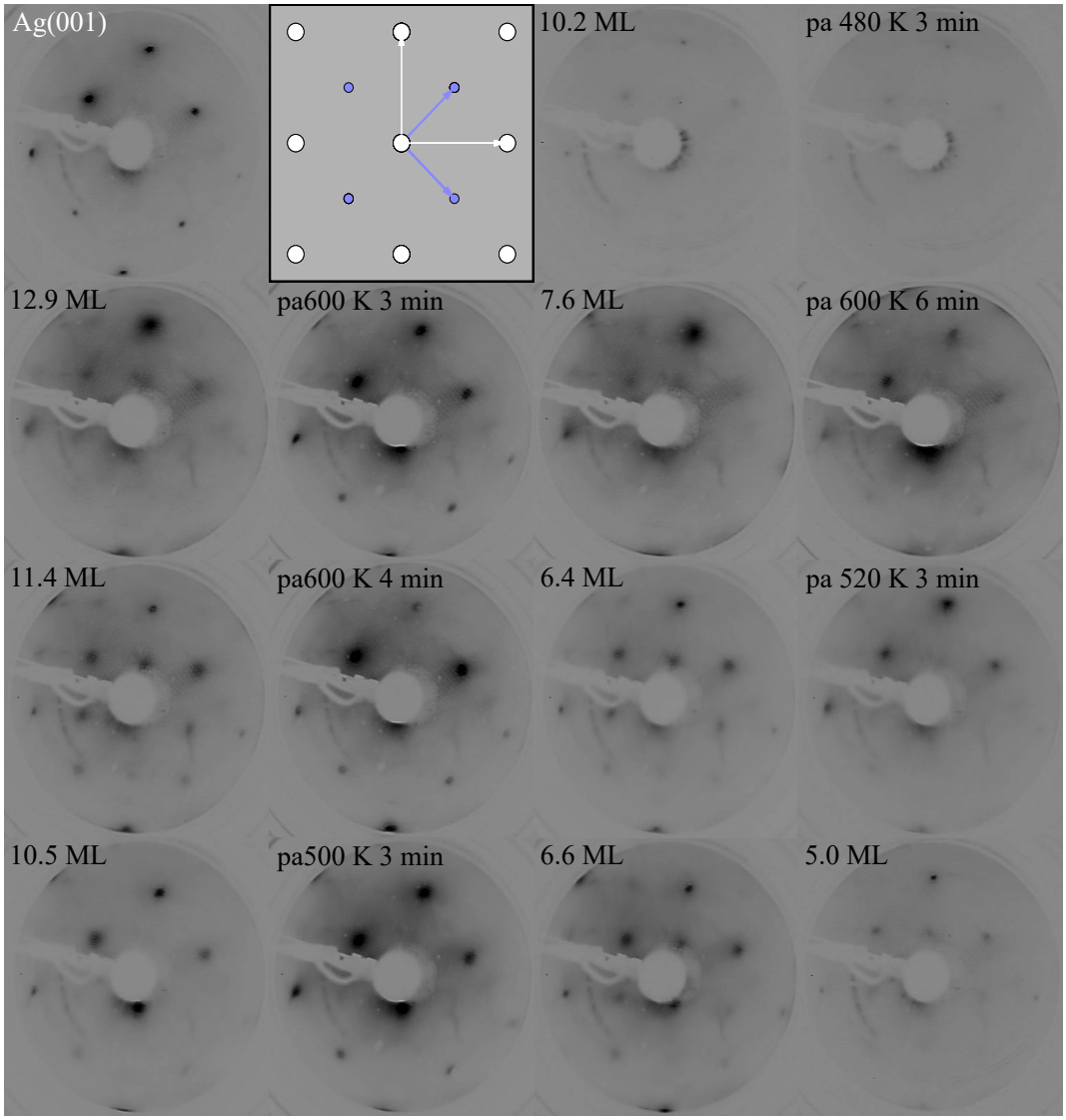

Figure 7.7: LEED images for as-grown and post-annealed Mn_xAu_{1-x} films on Ag(001) at 100 eV, only the ones for 11.4 ML $Mn_{0.43}Au_{0.57}$ on Ag(001) as-grown and post-annealed samples are at 105 eV. The first and third columns are for as-grown, the second and forth are post-annealed image of their next left image, first and third columns, respectively. The top second LEED pattern is a simulation for the c(2×2) superstructure by LEEDpat [117] . White and blue arrows show substrate and superstructure unit cell vectors, respectively.

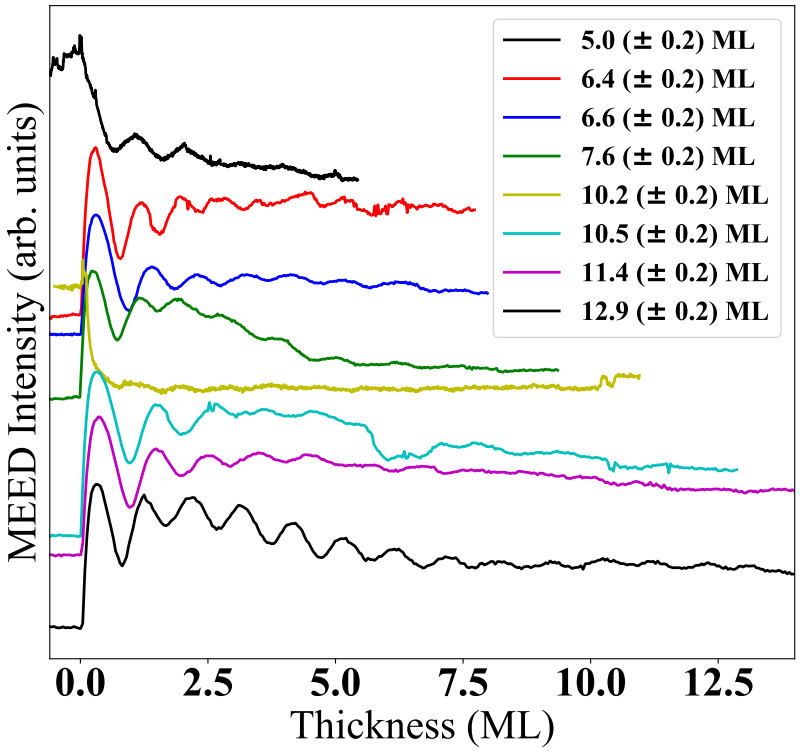

Figure 7.8: MEED oscillations of several Mn_xAu_{1-x} films on Ag(001). x can be seen from Tab. 7.3.

gen Auger (O KVV (503 eV)) peaks are small but obvious compared to the other Auger spectra in Fig. 7.6. The annealing temperature was 480 K, this could also not be high enough to cause diffusion. Even the LEED-I(V) for as-grown and after post annealing match very well as shown in Fig. 7.6 (g) and the d_p for as-grown and after post-annealing are 2.01 and 2.02 Å, respectively. For post-annealing at higher temperatures, the LEED-I(V) is totally matched to the substrate scans. Related LEED images for as-grown and after post-annealing of Mn_xAu_{1-x} films on Ag(001) are displayed in Fig. 7.7 at 100 eV. In Fig. 7.8, we show MEED oscillations of Mn_xAu_{1-x} from 5.0 to 12.9 ML for different x (from 0.3 to 0.98). The results are tabulated in Tab. 7.3 for LEED structure, vertical interlayer spacing (from LEED-I(V)), and Mn-Au alloy ratio. As-grown Mn_xAu_{1-x} films on Ag(001) are showing different LEED patterns (1×1, c(2×2)) in Fig. 7.7. The reason for this could be due to the different crystal forms of Mn-Au alloys on the surface. For example, in the work of Yamada et al., they show that $Mn_{50}Au_{50}$ displays a c(2×2)

pattern [112]. They obtained Mn_2Au by Au grown on top of bct Mn(001) films. At 4th layer of Au films, the structure displays (5×23) Au reconstruction. And Mn_2Au has a bct structure [129, 96]. Furthermore, Au_4Mn, Au_2Mn, and Au_2Mn have Ni_4Mo, bct, and bcc structure, respectively [130]. Different thicknesses of the films could also cause different crystal forms.

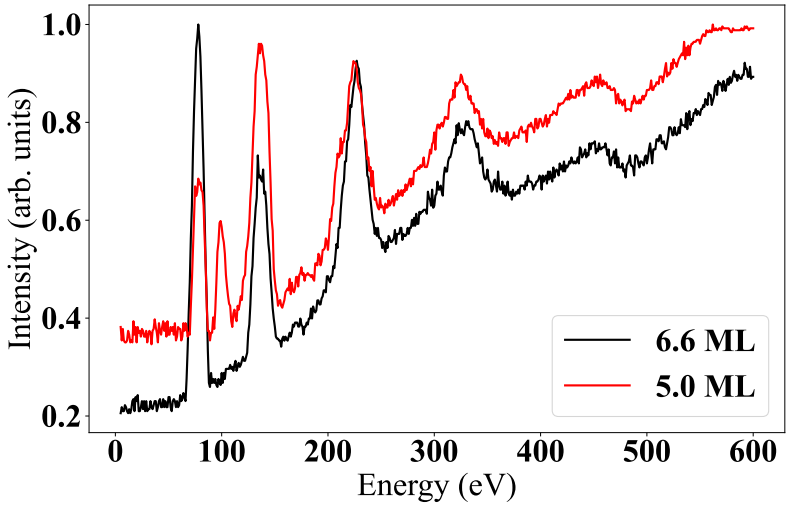

Figure 7.9: LEED-I(V) of 5.0 ML $Mn_{0.53}Au_{0.47}$ and 6.6 ML $Mn_{0.48}Au_{0.52}$ on Ag(001).

In Fig. 7.9, we see LEED-I(V) curves of two samples with 5.0 and 6.6 ML of Mn_xAu_{1-x} on Ag(001) for investigating the thickness dependence of the vertical interlayer spacing. The measured values are 2.02 and 1.99 Å (±0.02 Å), respectively. There is no difference in the vertical layer distance for these two samples with different thicknesses of 5.0 ML $Mn_{0.53}Au_{0.47}$ and 6.6 ML $Mn_{0.48}Au_{0.52}$ on Ag(001) within the error. In Fig. 7.10, we want to check the heating effect on the diffusion of the films into the substrate. However, during heating and continuous measuring by Auger, the samples, after a while, start to oxidize. We can see that the Mn (589 eV) and Ag (356 eV) Auger transition peak heights are not changed up to around 400 K. In Fig. 7.10 (a), we can see the emergence of the O (503 eV) Auger peak. When the oxygen peak emerges (above a temperature of 400 K), the Mn (542, 589, 636 eV) and Ag (356 eV) Auger peaks are visible even after completion of the post-annealing. However, while at low energies, the Mn 40 eV peak stays, the Au

69 eV peak disappears or gets very small. In Fig. 7.10 (b), we can see the trend of Ag(356)/Mn(589), how it increases by the increment of annealing temperature (above a temperature of 400 K). In Fig. 7.10 (c), the Mn(40)/Au(69) ratio increases extensively and abruptly compared to Ag(356)/Mn(589). This can be explained if Au diffuses more than Mn. We think that Mn oxidized, and thereby the Mn diffusion into the substrate stopped, but Au diffuses to the substrate. In Fig. 7.11, we can see that the LEED-I(V) curves are different for the as-grown sample in Fig. 7.10 and after post-annealing. The d_p are 1.87 and 2.15 Å, respectively. In another sample (in Fig. 7.12), we tried another method. We first heat the sample (365 K), let it cool down to RT, and measured the AES. We did this for 410 and 520 K. The sample did not oxidize, and we could see the diffusion of the films into the substrate. When the films diffuse into the substrate, we see only very small Auger peaks of Au and Mn compared to the as-grown films. In Fig. 7.12 (b) and (c), we can see the same trend in Ag(356)/Mn(589) and Mn(40)/Au(69) with substrate temperature increment as in Fig. 7.10 (b) and (c). Fig. 7.12 (b) shows the Mn diffusion into substrate. Fig. 7.12 (c) shows that Au diffuses more than Mn. The LEED-I(V) curves of 6.4 ML Mn_xAu_{1-x}/Ag(001) are displayed in Fig. 7.13. We can see that the LEED-I(V) curve of this sample after post-annealing is almost the same as for the as-grown sample. However, there is a small increment in the d_p, and after post-annealing d_p is 1.99 and 2.02 Å, respectively, as shown in Tab. 7.3.

Table 7.3: LEED-I(V) results for as-grown and post-annealed Mn_xAu_{1-x} on Ag(001).

	as-grown				after pa		
d (ML)	x^a	x^b	d_p (Å)	LEED	pa (K)	d_p (Å)	LEED
12.9	0.72±0.05	0.76±0.03	2.02	1×1	600	2.06	1×1
11.4	0.43±0.02	0.69±0.03	2.06	c(2×2)	600	2.02	1×1
10.5	0.3±0.02	0.63±0.03	1.98	1×1	500	2.06	1×1
10.2	0.32±0.03	0.70±0.03	2.01	1×1	480	2.02	1×1
7.6	0.98±0.03	0.82±0.03	1.87	1×1	600	2.15	1×1
6.6	0.48±0.03	0.74±0.03	1.99	c(2×2)	-	-	-
6.4	0.71±0.05	0.76±0.03	1.99	c(2×2)	520	2.02	1×1
5.0	0.53±0.04	0.84±0.03	2.02	c(2×2)	-	-	-

[a] and [b] are determined from the Ag356/Mn589 and Mn40/Au69 AES intensity ratios, respectively. Error in d_p is ±0.02 Å.

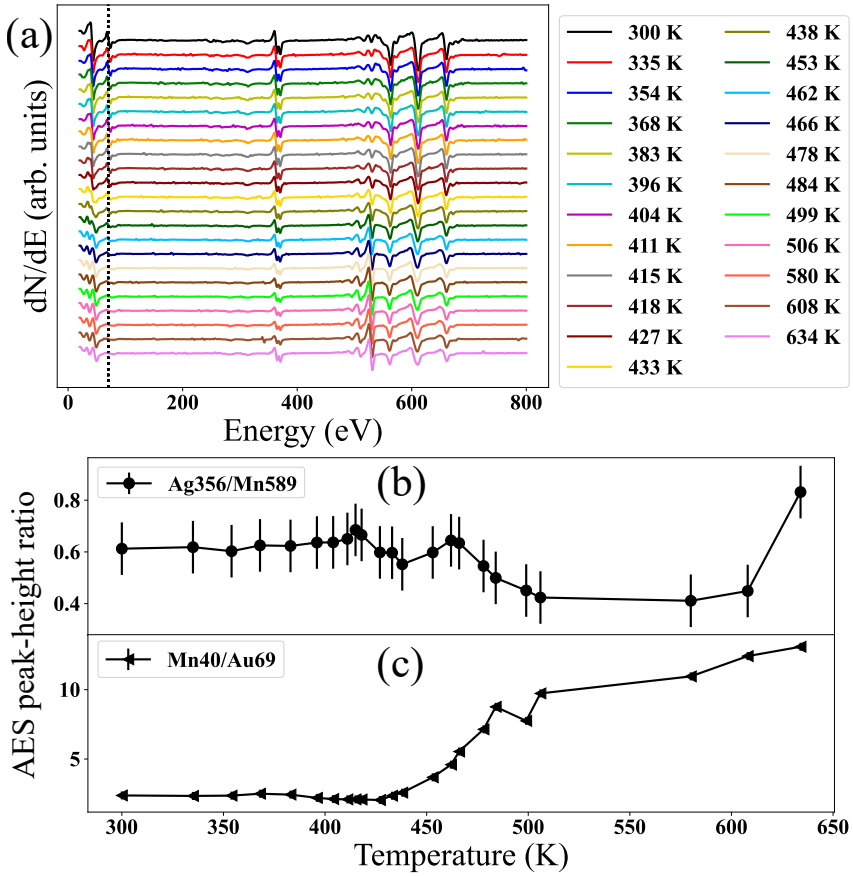

Figure 7.10: 7.6 ML Mn_xAu_{1-x} grown on Ag(001). (a) AES for the as-grown film and after heating the sample until 634 K. d_p = 1.87, 2.15 Å for as-grown and after pa, respectively. Auger ratio vs. temperature for (b) Ag356/Mn589 and (c) Mn40/Au69. The Auger ratios' error is calculated from the propagation of the errors in the determination of the peak heights.

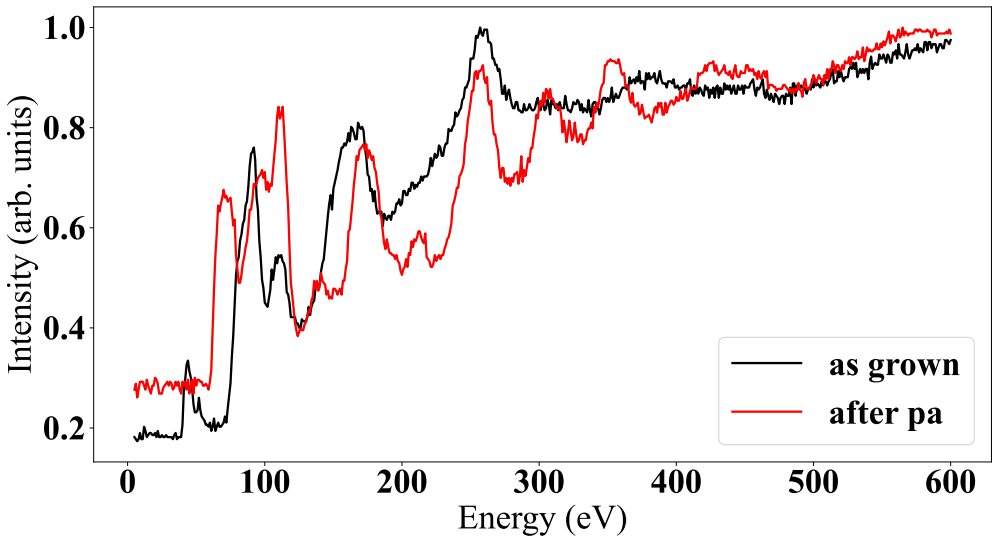

Figure 7.11: (a) LEED-I(V) for as-grown 7.6 ML $Mn_{0.98}Au_{0.2}$ on Ag(001) and after post-annealing (600 K).

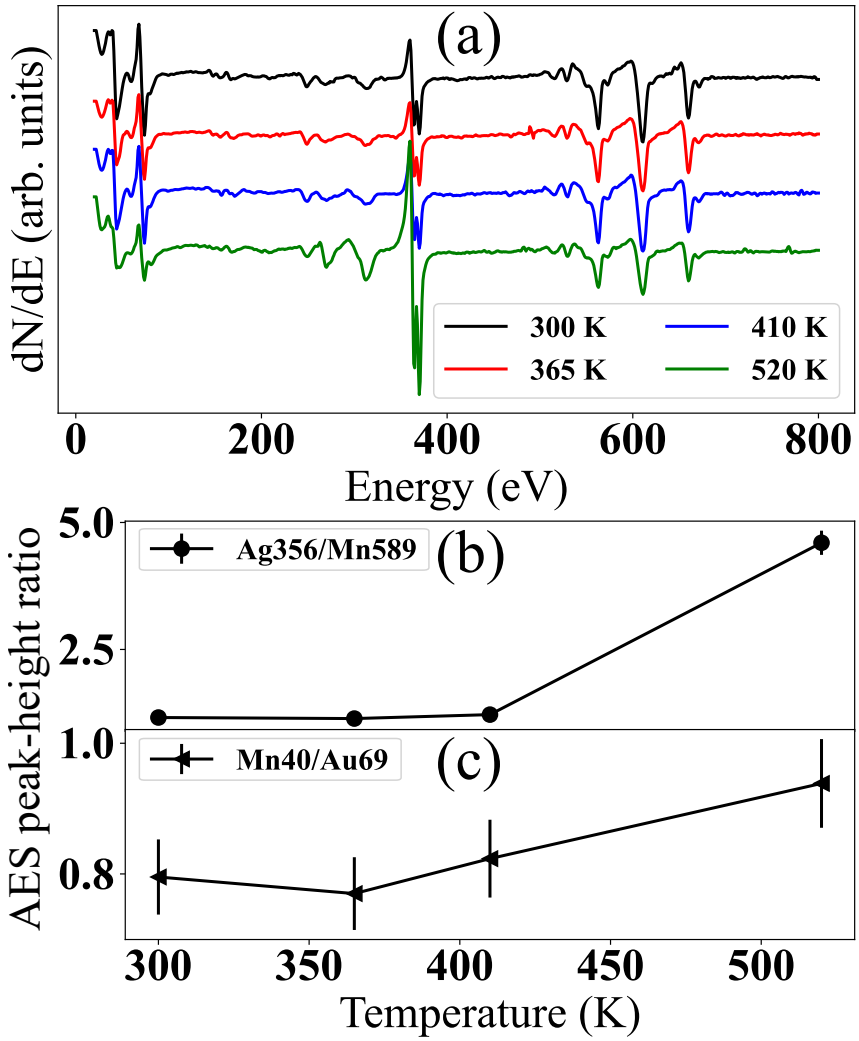

Figure 7.12: 6.4 ML $Mn_{0.71}Au_{0.29}$ grown on Ag(001). (a) AES for the as-grown sample and after post-annealing at 365, 410, and 520 K for 3 min each. d_p = 1.99, 2.02 Å for as-grown and after pa (520 K), respectively. Auger ratio vs. temperature for (b) Ag356/Mn589 and (c) Mn40/Au69. The Auger ratios' error is calculated from the propagation of the errors in the determination of the peak heights.

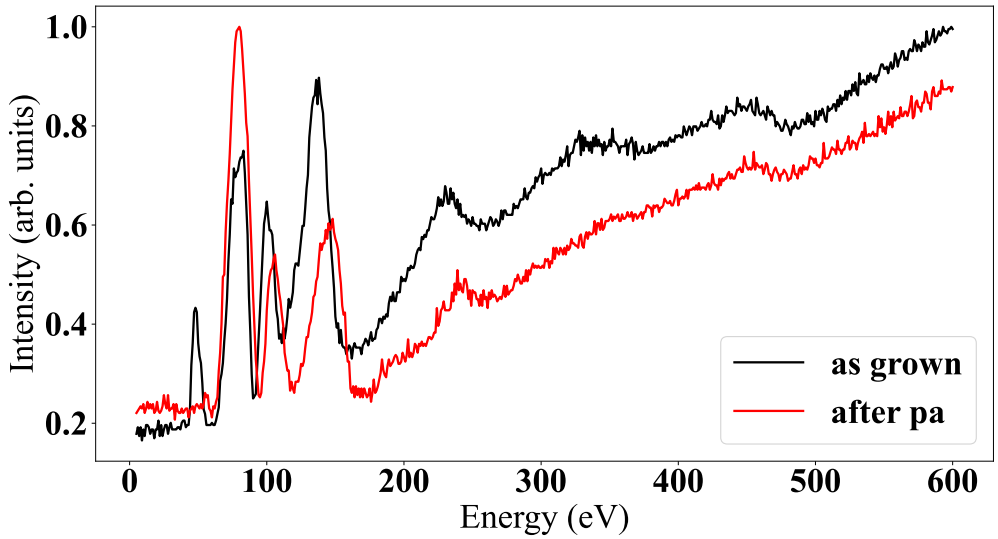

Figure 7.13: LEED-I(V) of 6.4 ML $Mn_{0.71}Au_{0.29}$ grown on Ag(001) for the as-grown film and after post-annealing (520 K for 3 min). The same sample is shown in Fig. 7.12.

To sum up, the thickness and Mn-Au ratio affect the crystal form, which we concluded from LEED patterns as summarized in Tab. 7.3. We see p(1×1) and c(2×2) structures for different thicknesses and x. Post-annealing has a big effect on films. Annealing above or around 400 K causes the films to diffuse into the substrate (Ag(001)). However, when the sample is oxidized, the diffusion stops or is very small. As-grown films have d_p from 1.87 to 2.06 Å. So the films have a lower d_p than Ag(001) except for 11.4 ML (d_p = 2.06 Å). The LEED, LEED-I(V), and AES results are tabulated in Tab. 7.3. When we have more Mn in the Mn-Au alloy, then we have a smaller d_p, which approaches the d_p of pure Mn films. The d_p values for Mn films on Ag(001) are summarized in Tab. 7.2.

7.4 Fe Growth on Ag(001)

Bulk Fe has a bcc phase at room temperature and an fcc γ phase at high temperature ($\approx$ 910 °C) [50]. For bcc Fe, the lattice constant is 2.866 Å and d_{bulk} is 1.43 Å. The Ag(001) lattice constant is 4.08 Å, which has a very big mismatch with Fe. However, when Fe grows on Ag(001) rotated by 45°, this reduces the mismatch to only

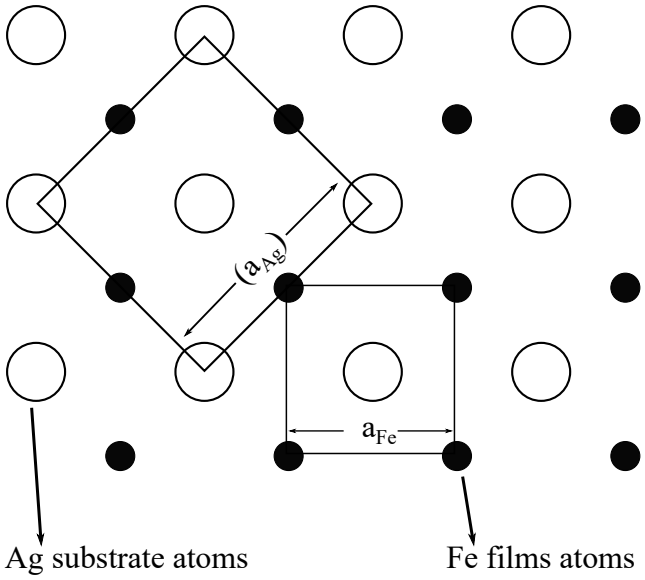

Figure 7.14: Schematic view of bcc Fe(001) growth on the Ag(001) surface by 45° rotation, so Fe(001) matches to Ag(001). The lattice constant is 4.08 Å for Ag(001), 2.87 Å for Fe(001). Therefore, the lattice mismatch is around 0.8 % [127]. The open circles depict Ag substrate atoms and filled circles display Fe film atoms. Image adapted/taken from [127].

0.8% [127, 131]. We can see the schematic view of bcc Fe films on fcc Ag(001) in Fig. 7.14. We grow the Fe on Ag(001) to study the structure and magnetic properties by LEED and MOKE, respectively. Several samples were prepared to investigate the interlayer spacing by LEED-I(V). The films were grown by electron beam evaporation.

In Fig. 7.15, we present LEED images of clean Ag(001) at 100 and 220 eV, along with LEED images for Fe films (from 7.7 to 22.3 ML) at around 100 and 180 eV. The Fe films display p(1×1) patterns like Ag(001) [132]. In Fig. 7.16 (a), the AES spectra of different thicknesses of Fe that have been grown on Ag(001) are shown. And we also obtain the AES parameters for Fe on Ag(001) as shown in Fig. 7.16 (b). From LEED-I(V) scans, we obtain the d_p. The d_p results vary from 1.41 to 1.43 Å, which are shown in Fig. 7.17. The vertical interlayer distances for different thicknesses of Fe films on Ag(001) are almost the same. This could be due to the lattice match of the (001) planes of films and substrate. Urquhart claimed that Fe grows layer-by-layer up to at least 28 ML [127]. We can see that the LEED patterns resemble each other for thinner and thicker films of Fe on Ag(001). The Fe

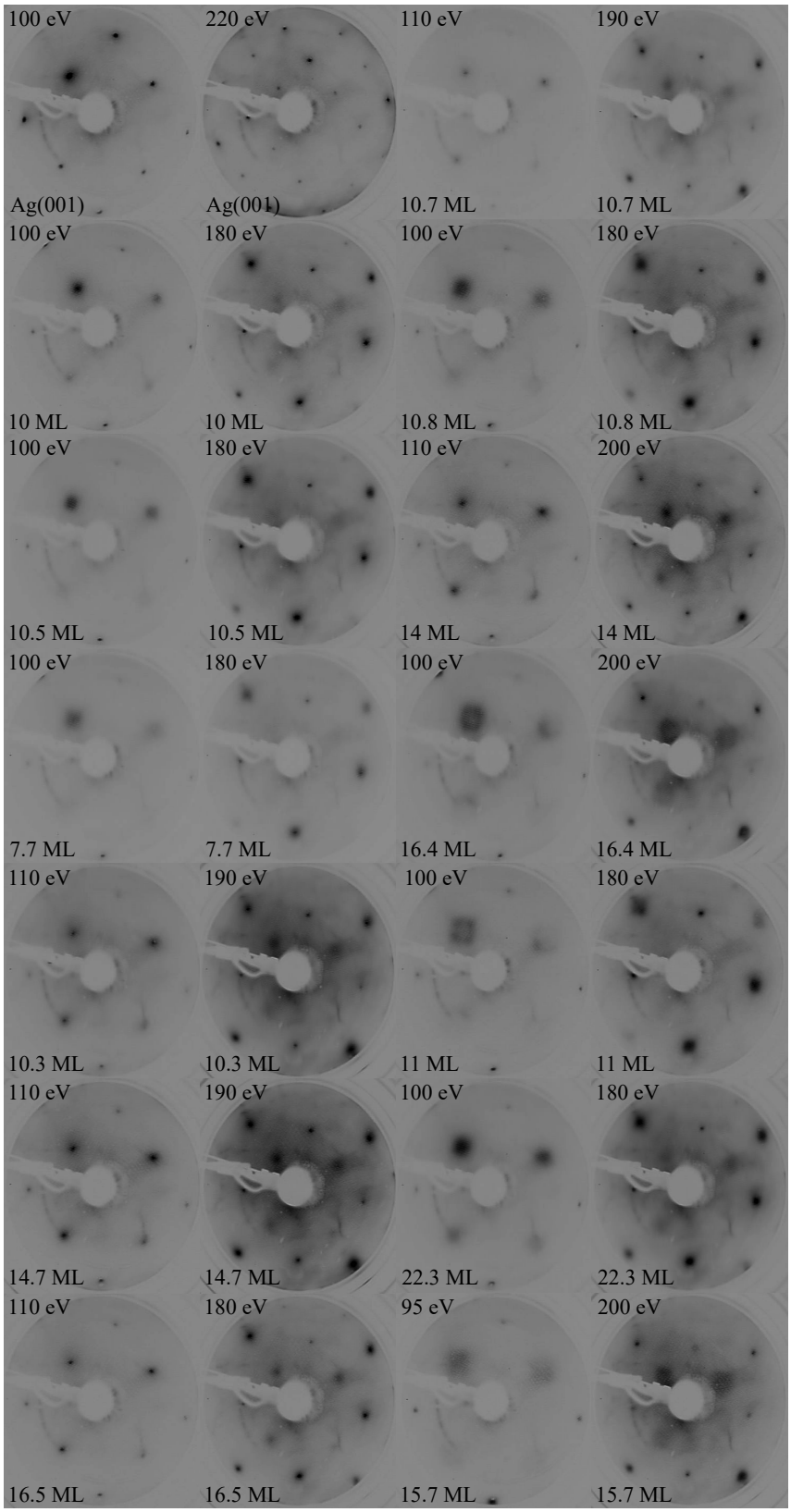

Figure 7.15: LEED images of clean Ag(001) and for Fe films (from 7.7 to 22.3 ML) on Ag(001).

films on Ag(001) are not tetragonally strained; therefore, no strain relaxation occurs for thicker films. The LEED patterns for thicker films are broader, which could be related to the roughness of the surface.

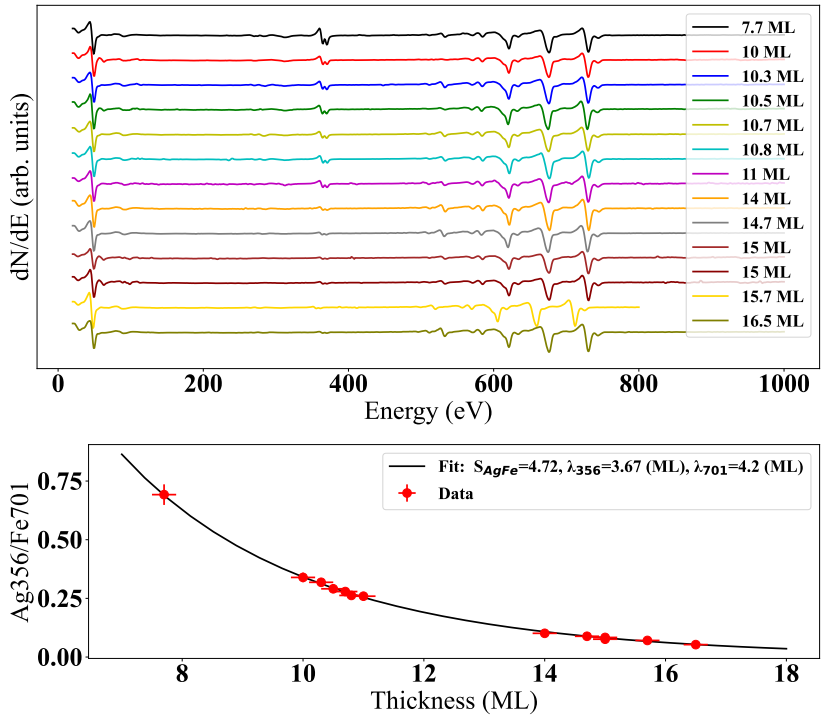

Figure 7.16: (a) AES for Fe films on Ag(001) (from 7.7 to 22.3 ML). (b) The exponential least square fit for Auger peak-to-peak height ratio (Ag_{356}/Fe_{701}) vs. thickness of Fe on Ag(001).

7.5 Fe Growth on Mn_xAu_{1-x}/Ag(001)

In this part, we study the bilayer films on the Ag(001) substrate. The Fe is grown on different post-annealed Mn_xAu_{1-x} films on Ag(001). The Mn_xAu_{1-x} films' thicknesses are calculated from MEED oscillations as shown in Fig. 7.18. These Mn_xAu_{1-x} films (10.3, 12.3, 13.9, and 13.6 ML) are post-annealed at 400, 530, 430, and 470 K, respectively. LEED images of as-grown and post-annealed Mn_xAu_{1-x} on Ag(001) are displayed in Fig. 7.20. The LEED pattern of Mn_xAu_{1-x} at RT show a very dim p(1×1). Post-annealed for 10.3 ML Mn_xAu_{1-x} sample displays c(2×2). The remain post-annealed Mn_xAu_{1-x} films (12.3, 13.9, and 13.6 ML) display p(1×1). The Fe films grown on post-annealed Mn_xAu_{1-x} samples de-

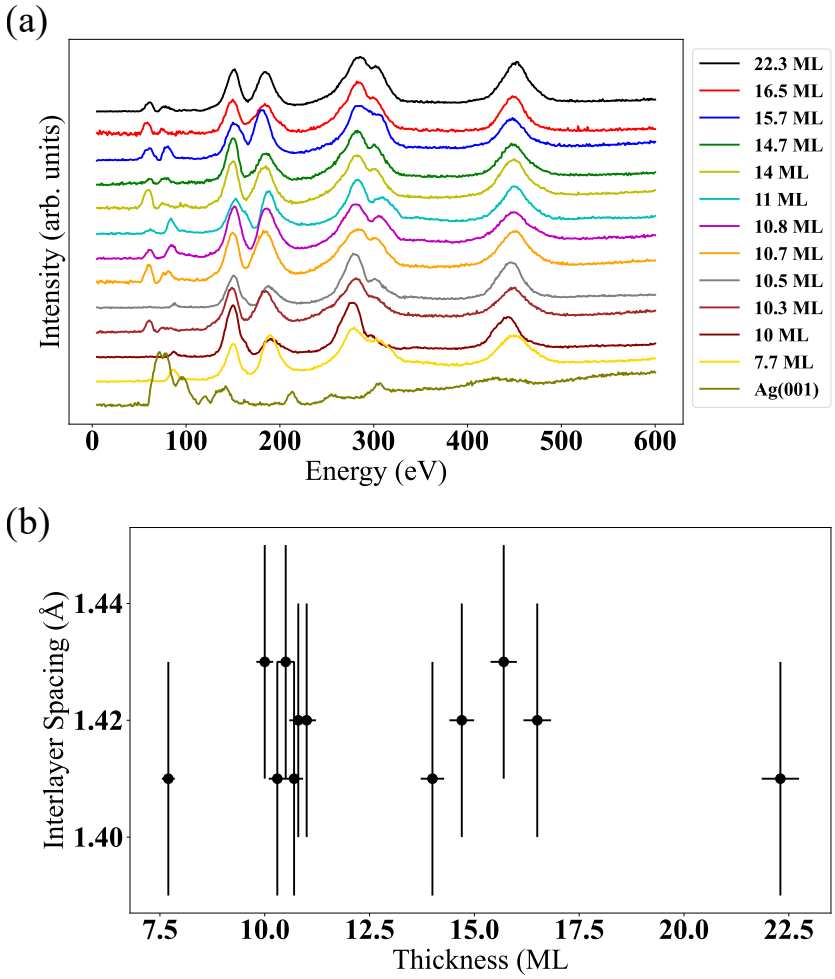

Figure 7.17: (a) LEED-I(V) for Fe films on Ag(001) (from 7.7 to 22.3 ML). (b) Vertical interlayer spacing for Fe films grown on Ag(001).

pict p(1×1) LEED patterns which are shown in Fig. 7.20, the same as Fe grown on Ag(001). However, the (10) spots are more brighter than the (11) spots for a beam energy of 100 eV. LEED-I(V) is employed for as-grown and post-annealed Mn_xAu_{1-x}, and after Fe growth on post-annealed Mn_xAu_{1-x}, which is depicted in Fig. 7.19. There are no changes after post-annealing in the LEED-I(V) curves. In Tab. 7.4, we show the d_p for as-grown and post-annealed Mn_xAu_{1-x} films. These Mn_xAu_{1-x} films can also be compared to the previous results in Tab. 7.3. The vertical interlayer spacing for Fe (d_p 1.41 Å) on post-annealed Mn_xAu_{1-x} is similar to the one of Fe (d_p 1.41 Å) grown on Ag(001).

In Fig. 7.21 (a), we show AES spectra of the as-grown Mn_xAu_{1-x} film and after post-annealing. Fig. 7.21 (b) shows the Auger ratio of the peak heights of

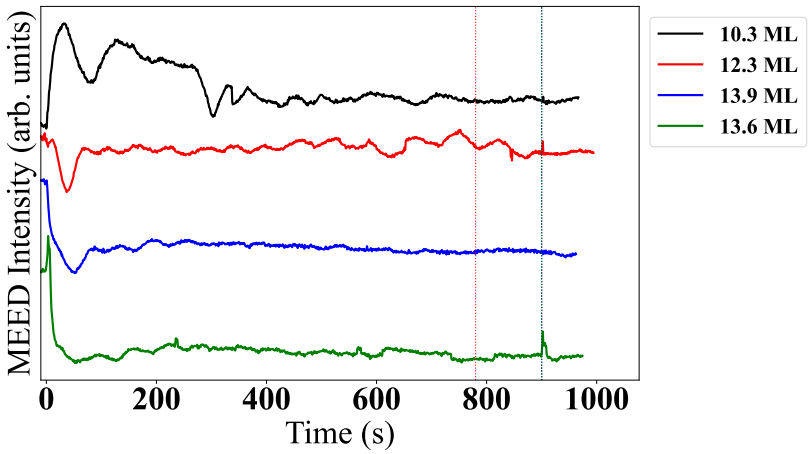

Figure 7.18: The MEED intensity curves of 10.3, 12.3, 13.9, and 13.6 ML Mn_xAu_{1-x} on Ag(001) prepared in 15, 13, 15, and 15 min, respectively. The post-annealing and x are summarized in Tabs. 7.4 and 7.5.

Table 7.4: LEED-I(V) results for as-grown and post-annealed (error in T is ±20 K) Mn_xAu_{1-x} films on Ag(001) as well as Fe on post-annealed Mn_xAu_{1-x}. Error in d_p is ±0.02 Å. x for the Mn_xAu_{1-x} films are shown in Fig. 7.21.

	as-grown Mn_xAu_{1-x}			after pa			Fe	
d (ML)	d_p (Å)	LEED	T (K)	d_p (Å)	LEED	d (ML)	d_p (Å)	LEED
10.3	1.93	c(2×2)	400	1.93	c(2×2)	13.6	1.41	1×1
12.3	-	1×1	530	-	1×1	13.6	1.42	1×1
13.9	1.92	c(2×2)	430	1.92	1×1	13.6	1.42	1×1
13.6	1.95	c(2×2)	470	1.95	1×1	3.4	1.42	1×1

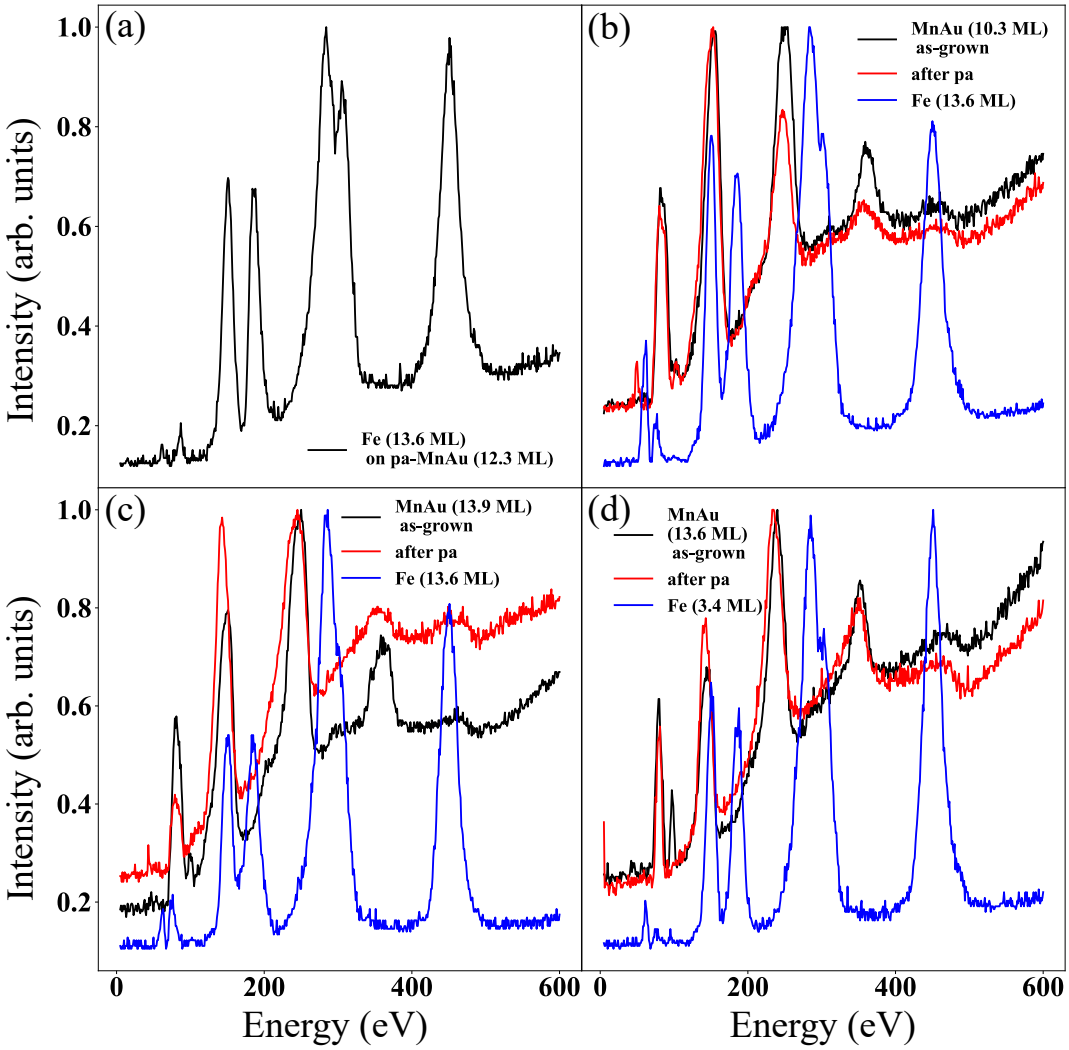

Figure 7.19: (a) LEED-I(V) 13.6 ML Fe on Mn_xAu_{1-x} post-annealed at 530 K for 3 min. (b), (c), and (d) display LEED-I(V) of as-grown Mn_xAu_{1-x}, post-annealed Mn_xAu_{1-x}, and as well as Fe on post-annealed Mn_xAu_{1-x}. (b), (c), and (d) Mn_xAu_{1-x} are post-annealed at 400 K (4 min), 430 K (4 min), and 470 K (4 min), respectively. The post-annealing and x are summarized in Tabs. 7.4 and 7.5.

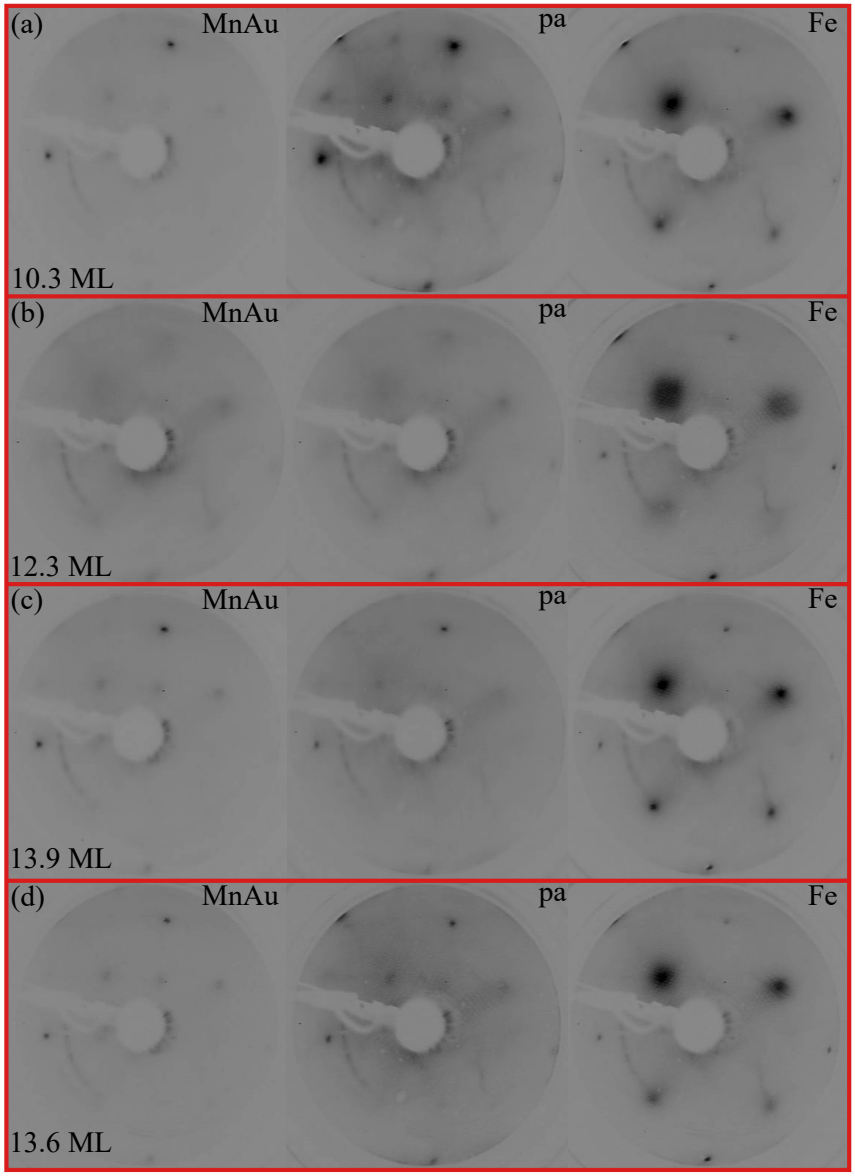

Figure 7.20: The LEED patterns of the samples in Fig. 7.19 at 100 eV. (a), (b), (c), and (d) display LEED patterns of as-grown Mn_xAu_{1-x}, post-annealed Mn_xAu_{1-x}, and as well as Fe on post-annealed Mn_xAu_{1-x}. (a), (b), (c), and (d) Mn_xAu_{1-x} are post-annealed at 530 K (3 min), 400 K (4 min), 430 K (4 min), and 470 K (4 min), respectively. The post-annealing and x are summarized in Tabs. 7.4 and 7.5.

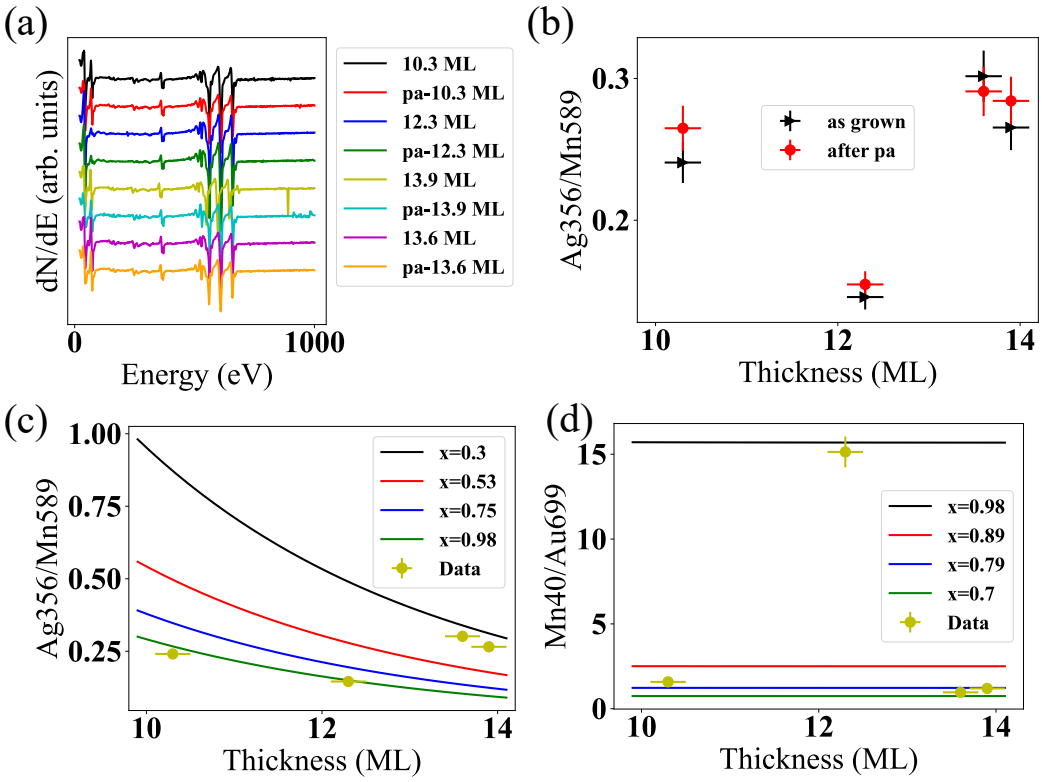

Figure 7.21: (a) AES spectra of Mn_xAu_{1-x} on Ag(001) samples as-grown and after post-annealing from Figs. 7.19 and 7.20. (b) The Auger ratio of Ag356/Mn589 for as-grown Mn_xAu_{1-x} and after post-annealing at 400 (4 min), 530 (1 min), 430 (4 min), and 470 K (4 min) for 10.3, 12.3, 13.9, 13.6 ML Mn_xAu_{1-x} films on Ag(001), respectively. (c) and (d) for Mn and Au ratio calculation for as-grown Mn_xAu_{1-x} on Ag(001) from the Auger ratios Ag356/Mn589 and Mn40/Au69, respectively.

Table 7.5: Mn and Au ratio obtained from Mn589/Ag356 and Mn40/Au69 Auger peak ratios.

	as-grown		after pa	
Thickness (ML)	x^{a}	x^{b}	x^{a}	x^{b}
10.3 ±0.3	1±0.2	0.82±0.2	0.98±0.5	0.81±0.2
12.3 ±0.2	1±0.2	0.98±0.2	0.95±0.5	0.97±0.2
13.9 ±0.2	0.35±0.2	0.79±0.2	0.33±0.2	0.78±0.2
13.6 ±0.6	0.34±0.2	0.75±0.2	0.35±0.2	0.75±0.2

^{a} and ^{b} are for Ag356/Mn589 and Mn40/Au69, respectively.

Ag (356 eV) and Mn (589 eV). We can see that after post-annealing, the peak ratio does not change dramatically. In Fig. 7.21 (c) and (d) x is calculated by using the Ag356/Mn589 and Mn40/Au69 peak height ratios, respectively. In Tab. 7.5, we can see that there is no big difference in x after post-annealing. The Ag356/Mn589 ratio gives information from more depth, while the Mn40/Au69 ratio gives information close to the surface. If the Au or Mn growth rate changes at the end, we might obtain different x. In the samples with 13.9 and 13.6 ML Mn_xAu_{1-x}, we have a big difference in x. x is calculated from Ag356/Mn589 gives 0.35 and 0.34, from Mn40/Au69 ratio, it gives 0.79 and 0.75 for the 13.9 and 13.6 ML Mn_xAu_{1-x} samples, respectively.

7.6 L-MOKE Results of Fe/Mn_xAu_{1-x}/Ag(001)

The samples are analyzed in situ by L-MOKE. The samples are Fe-Mn_xAu_{1-x} bilayer films grown on Ag(001). The thicknesses of Fe or Mn_xAu_{1-x} vary, and L-MOKE is employed to study the magnetic properties. Fe films have a strong in-plane anisotropy with easy axes along the [110] directions [127, 133].

In Fig. 7.22, we have grown 5 times 7.5 ML Fe on 5.2 ML $Mn_{0.9}Au_{0.1}$/Ag(001) to observe coercivity changes. In the initial growth of 7.5 ML, the loop signal is distorted, but the coercivity is still not much different than in the other loops. After 15 ML of Fe growth, there is no change in the hysteresis. In AFM-FM coupled bilayers, when the FM thickness increases, the coercivity is supposed to reduce, but in Fig. 7.22 the MOKE hysteresis does not show any change. This could be due to the very low thickness of the AFM film of 5.2 ML $Mn_{0.9}Au_{0.1}$ on Ag(001). Due

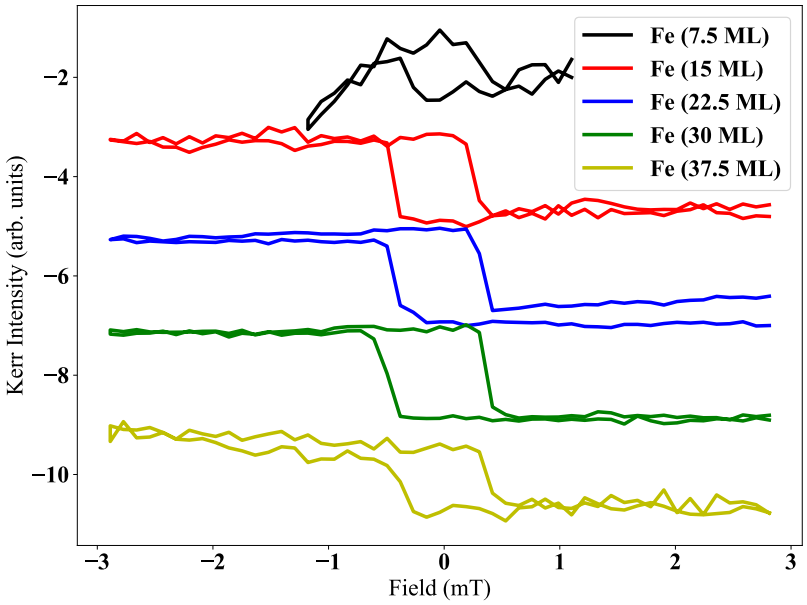

Figure 7.22: L-MOKE of 5×7.5 ML of Fe on 5.2 ML $Mn_{0.9}Au_{0.1}$/Ag(001) deposited subsequently. The loops are normalized to the maximum intensity (y-axis) of the entire range. The hysteresis loops are shifted vertically for clarity.

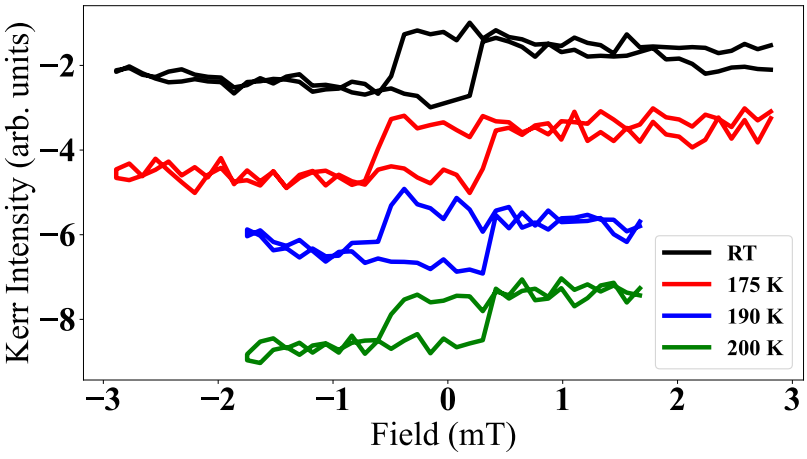

Figure 7.23: L-MOKE of Fe (9.4 ML) on 13.7 ML $Mn_{0.7}Au_{0.3}$/Ag(001) post-annealed at 500 K for 1 min at low temperature. The loops are normalized to the maximum intensity (y-axis) of the entire range. The hysteresis loops are shifted vertically for clarity.

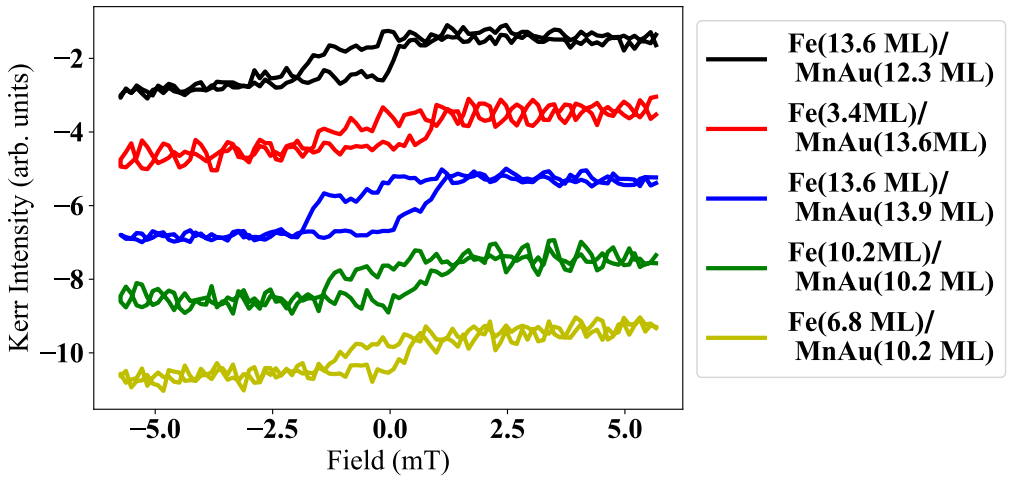

Figure 7.24: L-MOKE of Fe (13.6 ML) on Mn_xAu_{1-x} (12.3 ML), Fe (3.4 ML) on Mn_xAu_{1-x} (13.6 ML), Fe (13.6 ML) on Mn_xAu_{1-x} (13.9 ML), Fe (10.2 ML) on Mn_xAu_{1-x} (10.2 ML) and Fe (6.8 ML) on Mn_xAu_{1-x} (10.2 ML) on Ag(001). x is tabulated in Tab. 7.5 for 12.3, 13.6, 13.9 ML Mn_xAu_{1-x}/Ag(001). x is shown in Tab. 7.3 for 10.2 ML Mn_xAu_{1-x}/Ag(001). The loops are normalized to the maximum intensity (y-axis) of the entire range. The hysteresis loops are shifted vertically for clarity.

to finite-size effects, T_N increases with AFM film thickness [134, 135]. In work of Won et al., the AFM ordering exists around 9 ML thickness of an FeMn film [135]. Therefore, our Mn_xAu_{1-x} film might be to thin to establish AFM ordering. In Fig. 7.23, we did L-MOKE at low temperature without field cooling for the sample of Fe (9.4 ML) on $Mn_{0.7}Au_{0.3}$ (13.7 ML)/Ag(001), which does also not show any change. Coupling to an AFM could increase the coercivity when temperature decreases. In Fig. 7.24, we have 5 samples, Fe (13.6 ML) on Mn_xAu_{1-x} (12.3 ML), Fe (3.4 ML) on Mn_xAu_{1-x} (13.6 ML), Fe (13.6 ML) on Mn_xAu_{1-x} (13.9 ML), Fe (10.2 ML) on Mn_xAu_{1-x}(10.2 ML), Fe (6.8 ML) on Mn_xAu_{1-x} (10.2 ML). All samples were grown on Ag(001). In Fig. 7.24, we measured 6.8 ML of Fe on post-annealed Mn_xAu_{1-x} (10.2 ML) at 400 K for 3 min, then we grow another 3.4 ML Fe on it. In Fig. 7.24, we tried different Fe thicknesses on Mn_xAu_{1-x} for x in the range of 0.3 to 1. This FM/AFM bilayer was studied by MOKE, however, we do not observe any changes. To observe exchange bias, we need to field-cool from or above T_N, which could be hard for Mn_2Au, because it has a very high T_N for a bulk crystal

(above 1000 K [17, 16]).

We also study some other samples, which are displayed in appendix C. In Fig. C.1, we start the presentation of the L-MOKE measurements first with 11.0 ML Fe on Ag(001), then 22.3 ML Fe, then grow 15.8 ML $Mn_{0.99}Au_{0.01}$ on top of 22.3 ML Fe. We can see a very small change in coercivity which gets a little bigger but is not a clear change to confirm the AFM/FM coupling. The double step in the hysteresis loop of Fe on Ag(001) could be due to a step-induced anisotropy which could persist even after growth of $Mn_{0.99}Au_{0.01}$ (15.8 ML) on Fe [136, 137, 138]. In Fig. C.2, we have two samples, Fe (9.4 ML), on $Mn_{0.88}Au_{0.12}$ (5.2 ML), and Fe (12.5 ML) on $Mn_{0.77}Au_{0.23}$ (7.6 ML).

In the work of Wu [96] et al., they grew Fe (from 3 to 10 nm) on 10 nm Mn_2Au on MgO(001) substrate for different thickness of Fe from 3 to 10 nm. They observed the exchange bias effect from 300 to 5 K under the field of 5 T. And they also saw the coercivity changes with Fe thickness. Zhou et al. also observed the H_{EB} for Py(5 nm)/ Mn_2Au(10 nm) bilayer films at 20 K after FC at 10 kOe [126]. However, in the work of Jourdan et al., they did not observe any exchange bias shift (there is a negligible shift) for an Fe(5 nm) on Mn_2Au(7 nm) sample measured at temperatures of 300, 170, and 10 K. But, they observed clear coercivity changes for low temperatures (170 and 10 K) [27]. Bommanaboyena et al. did not observe an exchange bias shift for Mn_2Au(40 nm)/Py(2-10 nm) bilayer, but they show the coercivity decreases with increasing Py thickness. They also observed that H_C increased with increasing Mn_2Au layer thickness [87].

In our work, we mainly change the FM thickness while trying to observe a coercivity enhancement. However, we could not observe any clear changes in coercivity. And we also measured our sample below room temperature; also, there was no change in coercivity. There might be several reasons for that. In some films, it could be that the AFM films are too thin. Or, at the interface, we might not have an AFM-FM coupling because we do not have the right stoichiometry of Mn-Au alloy. We also did not cool our sample to very low temperatures (175 K due to the limit of

the setup).

7.7 Summary

The Mn, Mn_xAu_{1-x} and Fe thin films grow epitaxially on Ag(001). MEED intensity oscillations are observed for Mn and Mn_xAu_{1-x}. LEED and LEED-I(V) have been employed on either bilayers or single films grown on Ag(001) to observe the crystallinity of the films. While for Mn films and Fe films on bare Ag(001), we observe p(1×1) LEED patterns, for Mn_xAu_{1-x} we observe p(1×1) and c(2×2) LEED patterns. The error bars for the thickness are calculated as explained in Fig. 2.9. The error-bar calculation for d_p is explained in Fig. 2.7. The error bars in x come from the fitting.

Mn_xAu_{1-x} films' d_p are close to Ag(001), but bigger than the Mn films' d_p. We saw that d_p is bigger for smaller x, as shown in Tab. 7.3. For x = 0.98, d_p is 1.87 Å, for x in the range from 0.63 to 0.84, the vertical interlayer distances are around 2.0 Å, while for pure Mn films from 6.3 to 11.7 ML on Ag(001), vertical interlayer distances are in the range from 1.84 to 1.92 Å. As a consequence, we can say that d_p is increasing with the amount of Au in Mn_xAu_{1-x} films. Different thicknesses of Fe films on Ag(001) show the same (within the error) vertical interlayer distance (d_p is around 1.42 Å). We also study the annealing effect on the films on Ag(001). We conclude that for higher annealing temperatures (above 500 K), we can see a very big diffusion of films into the substrate. We also observed that when the films are oxidized, there is no diffusion or only a very small diffusion to the substrate. STM images show the topography of the growth of Mn_xAu_{1-x} on Ag(001) for 1.7 ML Mn_xAu_{1-x} on Ag(001), which has one complete layer and on top of this layer islands. For the magnetic properties of the films, we employed MOKE. However, we could not observe any clear changes in MOKE loops for different Fe and Mn_xAu_{1-x} on Ag(001) bilayer thickness and also for different x.

CHAPTER 8

Summary

The goal of the thesis is to study the structure and magnetic property of AFM Mn_2Au thin films grown on Cu(001) and Ag(001) single crystals in UHV. However, due to the difficulty of Mn_2Au growth, we study Mn_xAu_{1-x} to observe the Mn-Au alloy ratio's effect on the structure and magnetic properties. The thesis consists of four works which are explained in four chapters.

Chapter 4 starts by studying the Au/Mn/Co trilayer on Cu(001), employing MEED, LEED, LEED-I(V), MOKE, STM, XMCD, and XRMR. So we could obtain the growth rate for Au, Mn, and Co on Cu(001) subsequently because these three materials show MEED oscillations on Cu(001) in the Au/Mn/Co sequence. By employing the LEED-I(V), we saw that Co films have a lower vertical interlayer distance than Cu(001). However, Mn films on Co show bigger vertical interlayer distances. While we could observe p(1×1) LEED patterns for only Co and Mn on Co films, we could not see a clear LEED pattern for an Au film on Mn/Co/Cu(001). We also see that the STM image of Au/Mn/Co/Cu(001) displays a rough surface. We investigate the magnetic and chemical profile of an Au/Mn/Co trilayer on Cu(001) using XAS and XRMR. The Co $L_{2,3}$ edge shows an obvious XMCD, but there is no XMCD for the Mn $L_{2,3}$ edge. We could simulate Au/Mn/Co/Cu(001) XRMR results to understand or investigate sample properties such as film thickness and roughness. The XRMR simulation shows that the sample does not have considerable interface roughness.

In Chapter 5, to understand the morphology and structure of Mn_xAu_{1-x} films grown on Cu(001), we start with a study of Mn_xAu_{1-x} growth on Cu(001) using AES, LEED, MEED, and STM from sub-ML to thicker films. For up to around 1 ML thickness, LEED patterns show a c(2×2) structure. STM shows island growth, and when the coverage reaches around 1 ML, the islands merge and

create full coverage. However, no LEED patterns could be observed above 1 ML Mn_xAu_{1-x} on Cu(001). Mn on Cu(001) and Au on Cu(001) have already been studied before and have shown the same LEED patterns as observed here for the Mn-Au alloy on Cu(001).

In Chapter 6, to unveil the magnetic properties of Mn_xAu_{1-x}, we grow Mn_xAu_{1-x} in contact with a Co layer on Cu(001). We observe that the coercivity changes with temperature. However, we did not observe any exchange bias. The reason could be a too low T_N for these films of very low thickness. While we could observe MEED oscillations for Mn_xAu_{1-x} on Cu(001), we could not see any LEED patterns, which means that there is no long-range structural order of Mn_xAu_{1-x} on Cu(001).

In Chapter 7, we study Mn and Mn_xAu_{1-x} growth on Ag(001) to investigate the structure of Mn-Au alloys compared to pure Mn. In contrast to Mn_xAu_{1-x} on Cu(001), Mn_xAu_{1-x} films grown on Ag(001) display LEED patterns. Mn and Mn_xAu_{1-x} on Ag(001) show MEED oscillations during deposition. The MEED oscillations and the LEED patterns are an indication of epitaxial growth on Ag(001). We also observed that the vertical interlayer distances for Mn films, as evaluated from a kinematic analysis of LEED-I(V) curves, are lower than the one of the Ag(001) bulk crystal. However, the vertical interlayer distances for Mn_xAu_{1-x} films are close to the one of the Ag(001). We also observed that post-annealing of the films above 500 K causes diffusion of the film into the substrate. However, when Mn_xAu_{1-x} films oxidize, this diffusion stops. STM images of Mn_xAu_{1-x} on Ag(001) show that Mn_xAu_{1-x} film grows uniformly. Bilayers of Mn_xAu_{1-x} and Fe have been grown to investigate magnetic properties. For that, MOKE measurements have been performed to obtain hysteresis loops. However, we could not observe any obvious changes in coercivity for different thicknesses of Mn_xAu_{1-x} and Fe films.

All in all, we find that obtaining Mn_2Au thin films is very difficult. First, the growth of Au from a tungsten wire is not easily controllable without the help of a QCM to know the deposition rate. In an electron beam evaporator, we can at least

monitor the flux of Mn, but we cannot do it for Au. Therefore, it could be good to have a QCM. And also, using a PBN crucible for Au evaporation could be better for a controllable growth rate of Au. Growth of Mn_2Au thin films on a metallic surface, for which we used Ag(001) and Cu(001), makes the post-annealing hard because for post-annealing to above 500 K, the films diffuse into the substrate. So, for the substrate selection, one should consider other substrates with a high covalent bonding to prevent diffusion of these metallic films. For the magnetic investigation, we could have tried an experimental set-up that can provide a high magnetic field (at least 1 T) and very low temperature (at least around 10 K). The sub-ML of Mn_xAu_{1-x} could be studied by low-temperature STM with atomic resolution and with respect to local electronic properties, which we could not perform.

References

[1] A. H. Morrish, "The physical principles of magnetism," *The Physical Principles of Magnetism, by Allan H. Morrish, pp. 696. ISBN 0-7803-6029-X. Wiley-VCH, January 2001.*, p. 696, 2001.

[2] D. Weller and A. Moser, "Thermal effect limits in ultrahigh-density magnetic recording," *IEEE Transactions on Magnetics*, vol. 35, pp. 4423–4439, 1999.

[3] G. Binasch, P. Grünberg, F. Saurenbach, and W. Zinn, "Enhanced magnetoresistance in layered magnetic structures with antiferromagnetic interlayer exchange," *Physical Review B*, vol. 39, p. 4828, 1989.

[4] M. N. Baibich *et al.*, "Giant magnetoresistance of (001)Fe/(001)Cr magnetic superlattices," *Physical Review Letters*, vol. 61, p. 2472, 1988.

[5] S. Mao *et al.*, "Commercial TMR heads for hard disk drives: characterization and extendibility at 300 gbit^2," *IEEE Transactions on Magnetics*, vol. 42, pp. 97–102, 2006.

[6] D. Abramovitch and G. Franklin, "A brief history of disk drive control," *IEEE Control Systems Magazine*, vol. 22, pp. 28–42, 2002.

[7] M. M. Waldrop, "More than moore," *Nature*, vol. 530, pp. 144–148, 2016.

[8] V. K. Joshi, "Spintronics: A contemporary review of emerging electronics devices," *Engineering Science and Technology, an International Journal*, vol. 19, pp. 1503–1513, 2016.

[9] J. Nogués and I. K. Schuller, "Exchange bias," *Journal of Magnetism and Magnetic Materials*, vol. 192, pp. 203–232, 1999.

[10] A. Kimel, A. Kirilyuk, A. Tsvetkov, R. Pisarev, and T. Rasing, "Laser-induced ultrafast spin reorientation in the antiferromagnet $TmFeO_3$," *Nature*, vol. 429, pp. 850–853, 2004.

[11] M. Fiebig *et al.*, "Ultrafast magnetization dynamics of antiferromagnetic compounds," *Journal of Physics D: Applied Physics*, vol. 41, p. 164 005, 2008.

[12] V. Baltz, A. Manchon, M. Tsoi, T. Moriyama, T. Ono, and Y. Tserkovnyak, "Antiferromagnetic spintronics," *Reviews of Modern Physics*, vol. 90, p. 015 005, 2018.

[13] I. Kumberg *et al.*, "Accelerating the laser-induced demagnetization of a ferromagnetic film by antiferromagnetic order in an adjacent layer," *Physical Review B*, vol. 102, p. 214 418, 2020.

[14] T. Shinwari *et al.*, "Bulk and Interfacial Effects in the Co/Ni_xMn_{100-x} Exchange-Bias System due to Creation of Defects by Ar^+ Sputtering," *Physica Status Solidi (RRL)–Rapid Research Letters*, vol. 15, p. 2 100 195, 2021.

[15] T. Shinwari *et al.*, "Growth, Structure, and Magnetic Properties of Artificially Layered NiMn in Contact to Ferromagnetic Co on Cu3Au(001)," *Physica Status Solidi (b)*, p. 2 200 518, 2023.

[16] S. Khmelevskyi and P. Mohn, "Layered antiferromagnetism with high Néel temperature in the intermetallic compound Mn_2Au," *Applied Physics Letters*, vol. 93, p. 162 503, 2008.

[17] V. M. T. S. Barthem, C. V. Colin, H. Mayaffre, M. H. Julien, and D. Givord, "Revealing the properties of Mn_2Au for antiferromagnetic spintronics," *Nature Communications*, vol. 4, pp. 1–7, 2013.

[18] G. E. Bacon and E. W. Mason, "The magnetic structures of the alloys $Au_2(Mn, Al)_2$," *Proceedings of the Physical Society (1958-1967)*, vol. 92, p. 713, 1967.

[19] T. Yamada *et al.*, "Spin-polarized scanning tunneling microscopy/spectroscopy study of MnAu(001) thin films," *Physical Review B*, vol. 72, p. 014 410, 2005.

[20] S. Abe, M. Matsumoto, H. Yoshida, S. Mori, T. Kanomata, and T. Kaneko, "Thermal expansion anomalies at the magnetic transition temperatures of Au_4Mn and Au_2Mn," *Journal of Magnetism and Magnetic Materials*, vol. 104, pp. 2059–2060, 1992.

[21] A. B. Shick, S. Khmelevskyi, O. N. Mryasov, J. Wunderlich, and T. Jungwirth, "Spin-orbit coupling induced anisotropy effects in bimetallic antiferromagnets: A route towards antiferromagnetic spintronics," *Physical Review B*, vol. 81, p. 212 409, 2010.

[22] P. Roy, R. Otxoa, and J. Wunderlich, "Robust picosecond writing of a layered antiferromagnet by staggered spin-orbit fields," *Physical Review B*, vol. 94, p. 014 439, 2016.

[23] P. Wadley *et al.*, "Electrical switching of an antiferromagnet," *Science*, vol. 351, pp. 587–590, 2016.

[24] M. Meinert, D. Graulich, and T. Matalla-Wagner, "Electrical switching of antiferromagnetic $\mathrm{Mn_2Au}$ and the role of thermal activation," *Physical Review Applied*, vol. 9, p. 064 040, 2018.

[25] X. Chen *et al.*, "Electric field control of Néel spin-orbit torque in an antiferromagnet," *Nature Materials*, vol. 18, pp. 931–935, 2019.

[26] L. Salemi, M. Berritta, A. K. Nandy, and P. M. Oppeneer, "Orbitally dominated Rashba-Edelstein effect in noncentrosymmetric antiferromagnets," *Nature Communications*, vol. 10, pp. 1–10, 2019.

[27] M. Jourdan, H. Bräuning, A. Sapozhnik, H. J. Elmers, H. Zabel, and M. Kläui, "Epitaxial Mn_2Au thin films for antiferromagnetic spintronics," *Journal of Physics D: Applied Physics*, vol. 48, p. 385 001, 2015.

[28] X. Chen *et al.*, "Observation of the antiferromagnetic spin Hall effect," *Nature Materials*, vol. 20, pp. 800–804, 2021.

[29] X.-T. Jia *et al.*, "Spin Hall effect induced Néel order switching in the tetragonal Mn2Au," *Journal of Physics D: Applied Physics*, vol. 53, p. 245 001, 2020.

[30] B. J. Knapp, J. C. Hansen, J. A. Benson, and J. G. Tobin, "The electronic structure of gold overlayers on Cu(001)," *Surface Science*, vol. 188, pp. L675–L684, 1987.

[31] Y. Huttel, C. M. Teodorescu, F. Bertran, and G. Krill, "Experimental evidence of long-range magnetic order in the c(2×2) MnCu(100) surface alloy," *Physical Review B*, vol. 64, p. 094 405, 2001.

[32] K. Oura, V. G. Lifshits, A. A. Saranin, A. V. Zotov, and M. Katayama, *Surface Science: An Introduction*. Springer Berlin Heidelberg, 2003.

[33] H. Lüth, *Solid Surfaces, Interfaces and Thin Films*. Springer, 2001, vol. 4.

[34] A. G. Elliot, "The condensation of gold onto tantalum (100) single crystal surfaces: LEED, AES analysis," *Surface Science*, vol. 51, pp. 489–503, 1975.

[35] A. C. Levi and M. Kotrla, "Theory and simulation of crystal growth," *Journal of Physics: Condensed Matter*, vol. 9, p. 299, 1997.

[36] E. Golias *et al.*, "Ultrafast optically induced ferromagnetic state in an elemental antiferromagnet," *Physical Review Letters*, vol. 126, p. 107 202, 2021.

[37] C. Davisson and L. H. Germer, "Diffraction of electrons by a crystal of nickel," *Physical Review*, vol. 30, p. 705, 1927.

[38] R. Memeo, F. Ciccacci, C. Mariani, and S. Ossicini, "On the use of the Auger technique for quantitative analysis of overlayers," *Thin Solid Films*, vol. 109, pp. 159–167, 1983.

[39] D. P. Woodruff, "Methods of surface structure determination," in *Modern Techniques of Surface Science*, 3rd ed. Cambridge University Press, 2016, 98–214.

[40] P. J. Jennings and S. M. Thurgate, "The inner potential in LEED," *Surface Science Letters*, vol. 104, pp. L210–L212, 1981.

[41] C. Tieg, W. Kuch, S. G. Wang, and J. Kirschner, "Growth, structure, and magnetism of single-crystalline Ni_xMn_{100-x} films and NiMn/Co bilayers on Cu(001)," *Physical Review B*, vol. 74, p. 094 420, 2006.

[42] J. M. Walls, *Methods of surface analysis: Techniques and Applications*. CUP Archive, 1990.

[43] G. Binnig, H. Rohrer, C. Gerber, and E. Weibel, "Surface studies by scanning tunneling microscopy," *Physical Review Letters*, vol. 49, p. 57, 1982.

[44] S. Heinze *et al.*, "Real-space imaging of two-dimensional antiferromagnetism on the atomic scale," *Science*, vol. 288, pp. 1805–1808, 2000.

[45] A. Li Bassi *et al.*, "Bulk Cr tips for scanning tunneling microscopy and spin-polarized scanning tunneling microscopy," *Applied Physics Letters*, vol. 91, p. 173 120, 2007.

[46] R. Young, J. Ward, and F. Scire, "Observation of metal-vacuum-metal tunneling, field emission, and the transition region," *Physical Review Letters*, vol. 27, p. 922, 1971.

[47] J. Song, "Structural, electronic and magnetic properties of ultrathin epitaxial manganese films," Ph.D. dissertation, Freie Universität Berlin, 2015.

[48] C.-B. Wu, J. Song, and W. Kuch, "Spin-polarized scanning tunneling microscopy study of Mn/Co/Cu(001) using a bulk Fe ring probe," *Applied Physics Letters*, vol. 101, p. 012 404, 2012.

[49] W. Kuch, R. Schäfer, P. Fischer, and F. U. Hillebrecht, *Magnetic Microscopy of Layered Structures*. Springer, 2015, vol. 57.

[50] Z. Q. Qiu and S. D. Bader, "Surface magneto-optic Kerr effect (SMOKE)," *Journal of Magnetism and Magnetic Materials*, vol. 200, pp. 664–678, 1999.

[51] Z. Yang and M. Scheinfein, "Combined three-axis surface magneto-optical Kerr effects in the study of surface and ultrathin-film magnetism," *Journal of Applied Physics*, vol. 74, pp. 6810–6823, 1993.

[52] J. Kerr, "Xxiv. On reflection of polarized light from the equatorial surface of a magnet," *The London, Edinburgh, and Dublin Philosophical Magazine and Journal of Science*, vol. 5, pp. 161–177, 1878.

[53] A. Scherz, *Spin dependent x-ray absorption spectroscopy of 3d transition metals: systematics and applications*. PhD thesis, Freie Universität Berlin, 2004.

[54] Z. Q. Qiu and S. D. Bader, "Surface magneto-optic Kerr effect," *Review of Scientific Instruments*, vol. 71, pp. 1243–1255, 2000.

[55] E. R. Moog and S. D. Bader, "SMOKE signals from ferromagnetic monolayers: p(1x1) Fe/Au (100)," *Superlattices and microstructures*, vol. 1, pp. 543–552, 1985.

[56] J. Stöhr, "X-ray magnetic circular dichroism spectroscopy of transition metal thin films," *Journal of Electron Spectroscopy and Related Phenomena*, vol. 75, pp. 253–272, 1995.

[57] T. Noll, F. Radu, *et al.*, "The mechanics of the VEKMAG experiment," *Proc. of MEDSI2016, Barcelona, Spain*, pp. 370–373, 2016.

[58] C. T. Chen *et al.*, "Experimental Confirmation of the X-ray Magnetic Circular Dichroism Sum Rules for Iron and Cobalt," *Physical Review Letters*, vol. 75, p. 152, 1995.

[59] J. Stöhr, "Exploring the microscopic origin of magnetic anisotropies with X-ray magnetic circular dichroism (XMCD) spectroscopy," *Journal of Magnetism and Magnetic Materials*, vol. 200, pp. 470–497, 1999.

[60] S. Brück, S. Bauknecht, B. Ludescher, E. Goering, and G. Schütz, "An advanced magnetic reflectometer," *Review of Scientific Instruments*, vol. 79, p. 083 109, 2008.

[61] J. Krieft, D. Graulich, A. Moskaltsova, L. Bouchenoire, S. Francoual, and T. Kuschel, "Advanced data analysis procedure for hard x-ray resonant magnetic reflectivity discussed for Pt thin film samples of various complexity," *Journal of Physics D: Applied Physics*, vol. 53, p. 375 004, 2020.

[62] S. Macke and E. Goering, "Magnetic reflectometry of heterostructures," *Journal of Physics: Condensed Matter*, vol. 26, p. 363 201, 2014.

[63] D. Lott, "Magnetic x-ray reflectivity," Ph.D. dissertation, Ludwig-Maximilians-Universität München, 2001.

[64] C. Sorg, *Magnetic properties of 3d and 4f ferromagnets studied by X-ray absorption spectroscopy*. PhD thesis, Freie Universität Berlin, 2006.

[65] F. Scheurer, E. Beaurepaire, H. Bulou, and J. P. Kappler, "Magnetism and Synchrotron Radiation New Trends," *Springer Proceedings in Physics*, vol. 133, 2010.

[66] I. Kumberg, "Ultrafast demagnetization in metallic ferromagnetic/antiferromagnetic heterostructures," Ph.D. dissertation, Freie Universität Berlin, 2022.

[67] D. Schick, "UDKM1DSIM - a Python toolbox for simulating 1D ultrafast dynamics in condensed matter," *Computer Physics Communications*, vol. 266, p. 108 031, 2021.

[68] S. Macke, www.remagx.org.

[69] S. Macke *et al.*, "Element Specific Monolayer Depth Profiling," *Advanced Materials*, vol. 26, pp. 6554–6559, 2014.

[70] W. C. Cain and M. H. Kryder, "Investigation of the exchange mechanism in NiFe-TbCo bilayers," *Journal of Applied Physics*, vol. 67, pp. 5722–5724, 1990.

[71] P. Van der Zaag, R. Wolf, A. Ball, C Bordel, L. Feiner, and R Jungblut, "A study of the magnitude of exchange biasing in [111] Fe3O4/CoO bilayers," *Journal of Magnetism and Magnetic Materials*, vol. 148, pp. 346–348, 1995.

[72] W. Meiklejohn, "Exchange anisotropy—a review," *Journal of Applied Physics*, vol. 33, pp. 1328–1335, 1962.

[73] E. D. T. de Lacheisserie, D. Gignoux, and M. Schlenker, *Magnetism: I - Fundamentals*. Kluwer Academic Publishers: Norwell, 2002.

[74] W. H. Meiklejohn and C. P. Bean, "New magnetic anisotropy," *Physical Review*, vol. 102, p. 1413, 1956.

[75] R. L. Stamps, "Mechanisms for exchange bias," *Journal of Physics D: Applied Physics*, vol. 33, R247, 2000.

[76] A. A. Sapozhnik, M. Jourdan, H. Zabel, M. Kläui, and H. J. Elmers, "Exchange bias in epitaxial Mn_2Au(001)/Fe(001) bilayers," *Journal of Physics D: Applied Physics*, vol. 52, p. 465 003, 2019.

[77] J.-g. Hu, G.-j. Jin, and Y.-q. Ma, "Thickness dependence of exchange bias and coercivity in a ferromagnetic layer coupled with an antiferromagnetic layer," *Journal of applied physics*, vol. 94, pp. 2529–2533, 2003.

[78] M. Kiwi, "Exchange bias theory," *Journal of Magnetism and Magnetic materials*, vol. 234, pp. 584–595, 2001.

[79] A. E. Berkowitz and K. Takano, "Exchange anisotropy — a review," *Journal of Magnetism and Magnetic materials*, vol. 200, pp. 552–570, 1999.

[80] A. P. Malozemoff, "Mechanisms of exchange anisotropy," *Journal of Applied Physics*, vol. 63, pp. 3874–3879, 1988.

[81] A. P. Malozemoff, "Random-field model of exchange anisotropy at rough ferromagnetic-antiferromagnetic interfaces," *Physical Review B*, vol. 35, p. 3679, 1987.

[82] T. Kampfrath *et al.*, "Coherent terahertz control of antiferromagnetic spin waves," *Nature Photonics*, vol. 5, pp. 31–34, 2011.

[83] A. A. Sapozhnik *et al.*, "Direct imaging of antiferromagnetic domains in Mn_2Au manipulated by high magnetic fields," *Physical Review B*, vol. 97, p. 134 429, 2018.

[84] J. Hirst, U. Atxitia, S. Ruta, J. Jackson, L. Petit, and T. Ostler, "Temperature-dependent micromagnetic model of the antiferromagnet Mn_2Au: A multi-scale approach," *Physical Review B*, vol. 106, p. 094 402, 2022.

[85] S. Selzer *et al.*, "Current-induced switching of antiferromagnetic order in Mn_2Au from first principles," *Physical Review B*, vol. 105, p. 174 416, 2022.

[86] P. Wells and J. H. Smith, "The structure of Mn_2Au and Mn_3Au," *Acta Crystallographica Section A: Crystal Physics, Diffraction, Theoretical and General Crystallography*, vol. 26, pp. 379–381, 1970.

[87] S. P. Bommanaboyena *et al.*, "Readout of an antiferromagnetic spintronics system by strong exchange coupling of Mn_2Au and Permalloy," *Nature Communications*, vol. 12, pp. 1–7, 2021.

[88] S. Y. Bodnar *et al.*, "Imaging of current induced Néel vector switching in antiferromagnetic Mn_2Au," *Physical Review B*, vol. 99, p. 140 409, 2019.

[89] J. Železnỳ *et al.*, "Relativistic Néel-order fields induced by electrical current in antiferromagnets," *Physical review letters*, vol. 113, p. 157 201, 2014.

[90] H.-C. Wu *et al.*, "Anomalous anisotropic magnetoresistance of antiferromagnetic epitaxial bimetallic films: Mn_2Au and Mn_2Au/Fe bilayers," *Advanced Functional Materials*, vol. 26, pp. 5884–5892, 2016.

[91] M. Arana *et al.*, "Observation of magnons in Mn_2Au films by inelastic Brillouin and Raman light scattering," *Applied Physics Letters*, vol. 111, p. 192 409, 2017.

[92] X. F. Zhou *et al.*, "From fieldlike torque to antidamping torque in antiferromagnetic Mn_2Au," *Physical Review Applied*, vol. 11, p. 054 030, 2019.

[93] V. M. T. S. Barthem, C. V. Colin, R. Haettel, D. Dufeu, and D. Givord, "Easy moment direction and antiferromagnetic domain wall motion in Mn_2Au," *Journal of Magnetism and Magnetic Materials*, vol. 406, pp. 289–292, 2016.

[94] V. Grigorev *et al.*, "Optical Readout of the Néel Vector in the Metallic Antiferromagnet Mn_2Au," *Physical Review Applied*, vol. 16, p. 014 037, 2021.

[95] S. Y. Bodnar *et al.*, "Writing and reading antiferromagnetic mn2au by néel spin-orbit torques and large anisotropic magnetoresistance," *Nature communications*, vol. 9, pp. 1–7, 2018.

[96] H. C. Wu *et al.*, "Mn_2Au: Body-centered-tetragonal bimetallic antiferromagnets grown by molecular beam epitaxy," *Advanced Materials*, vol. 24, pp. 6374–6379, 2012.

[97] A. A. Sapozhnik *et al.*, "Manipulation of antiferromagnetic domain distribution in Mn_2Au by ultrahigh magnetic fields and by strain," *physica status solidi (RRL)–Rapid Research Letters*, vol. 11, p. 1 600 438, 2017.

[98] Z. Jin *et al.*, "Ultrafast electron transport in metallic antiferromagnetic Mn_2Au thin films probed by terahertz spectroscopy," *Physical Review B*, vol. 102, p. 014 438, 2020.

[99] B. B. Singh and S. Bedanta, "Large spin Hall angle and spin-mixing conductance in the highly resistive antiferromagnet Mn_2Au," *Physical Review Applied*, vol. 13, p. 044 020, 2020.

[100] U. Bovensiepen, *Phasenübergänge in magnetischen Monolagen und austauschgekoppelten Schichten: Eine in situ Studie mit ac-Suszeptibilität und Kerr-Effekt*. PhD thesis, Freie Universität Berlin: Shaker Verlag (Aachen), 2000.

[101] P. J. Hsu *et al.*, "Layered antiferromagnetic spin structures of expanded face-centered-tetragonal Mn(001) as an origin of exchange bias coupling to the magnetic Co layer," *Physical Review B*, vol. 85, p. 174 434, 2012.

[102] F. Offi, W. Kuch, and J. Kirschner, "Structural and magnetic properties of Fe_xMn_{1-x} thin films on Cu(001) and on Co/Cu(001)," *Physical Review B*, vol. 66, p. 064 419, 2002.

[103] J. T. Kohlhepp, H. Wieldraaijer, and W. J. M. de Jonge, "Exchange anisotropy as a probe of antiferromagnetism in expanded face-centered-tetragonal mn (001) layers," *Applied Physics Letters*, vol. 89, p. 032 507, 2006.

[104] B. C. Choi, P. J. Bode, and J. A. C. Bland, "Formation of a two-dimensional c(2×2) Mn-Co(001) ferromagnetic surface alloy on Cu(001)," *Physical Review B*, vol. 58, p. 5166, 1998.

[105] J. T. Kohlhepp and W. J. M. De Jonge, "Stabilization of metastable expanded face-centered-tetragonal manganese," *Physical Review Letters*, vol. 96, p. 237 201, 2006.

[106] E. Gullikson, *X-Ray Database: The Center for X-Ray Optics, Lawrence Berkeley National Laboratory's Materials Sciences Division :* `http://https://henke.lbl.gov/optical_constants`.

[107] B. L. Henke, E. M. Gullikson, and J. C. Davis, "X-ray interactions: photoabsorption, scattering, transmission, and reflection at E= 50-30,000 eV, Z= 1-92," *Atomic Data and Nuclear Data Tables*, vol. 54, pp. 181–342, 1993.

[108] M. Wuttig, Y. Gauthier, and S. Blügel, "Magnetically driven buckling and stability of ordered surface alloys: Cu(100) c(2×2) Mn," *Physical Review Letters*, vol. 70, p. 3619, 1993.

[109] J. C. Hansen and J. G. Tobin, "Angle-resolved photoelectron spectroscopy studies of surface alloying in Au/Cu (001)," *Journal of Vacuum Science & Technology A: Vacuum, Surfaces, and Films*, vol. 7, pp. 2475–2480, 1989.

[110] R. Van der Kraan and H. Van Kempen, "Growth of Mn on Cu(100) studied by STM: The c(2× 2) and pgg (4× 2) ordered surface alloys," *Surface Science*, vol. 338, pp. 19–30, 1995.

[111] J. Tobin, J. Hansen, and M. Wagner, "Probing bimetallic surfaces with photoelectron diffraction: Au/Cu(001) and Fe/Cu(001)," *Journal of Vacuum Science & Technology A: Vacuum, Surfaces, and Films*, vol. 8, pp. 2494–2496, 1990.

[112] T. K. Yamada, A. L. Vázquez de Parga, M. M. J. Bischoff, T. Mizoguchi, and H. van Kempen, "Study of c(2×2)-MnAu(001) layers on Mn(001) by means of scanning tunneling microscopy/spectroscopy," *Surface Science*, vol. 600, pp. 1048–1053, 2006.

[113] M. Eder, J. Hafner, and E. Moroni, "Structural, electronic, and magnetic properties of thin Mn/Cu(100) films," *Physical Review B*, vol. 61, p. 11 492, 2000.

[114] D. Wortmann, S. Heinze, G. Bihlmayer, and S. Blügel, "Interpreting STM images of the MnCu/Cu(100) surface alloy," *Physical Review B*, vol. 62, p. 2862, 2000.

[115] Y. Shokr, "Interaction Mechanisms and Magnetization Dynamics in Ultrathin Antiferromagnetic Films and their Correlation with Structure and Morphology," Ph.D. dissertation, Freie Universität Berlin, 2016.

[116] S. P. Bommanaboyena, T. Bergfeldt, R. Heller, M. Kläui, and M. Jourdan, "High quality epitaxial $Mn_2Au(001)$ thin films grown by molecular beam epitaxy," *Journal of Applied Physics*, vol. 127, p. 243 901, 2020.

[117] K. Hermann and M. A. Van Hove, *LEEDpat4.2: Simulation of LEED Pattern; FHI-Berlin, 2023*.

[118] T. Shinwari, "Fundamental Aspects of Exchange Bias Effect in (Ni/Co)/Ni_xMn_{100-x}/(Ni/Co) Bilayers, Trilayers and Multilayers on Cu_3Au (001)," Ph.D. dissertation, Freie Universität Berlin, 2022.

[119] W. F. Egelhoff and I. Jacob, "Reflection high-energy electron diffraction (RHEED) oscillations at 77 K," *Physical Review Letters*, vol. 62, pp. 921–924, 1989.

[120] H. Li *et al.*, "Quantitative low-energy electron-diffraction study of the epitaxy of Fe on Ag001: Questions about the growth mode," *Physical Review B*, vol. 42, pp. 9195–9198, 1990.

[121] J. W. Evans, D. E. Sanders, P. A. Thiel, and A. E. DePristo, "Low-temperature epitaxial growth of thin metal films," *Physical Review B*, vol. 41, p. 5410, 1990.

[122] J. G. Hu, G. Jin, A. Hu, and Y. Q. Ma, "Temperature dependence of exchange bias and coercivity in ferromagnetic/antiferromagnetic bilayers," *The European Physical Journal B-Condensed Matter and Complex Systems*, vol. 40, pp. 265–271, 2004.

[123] J. Camarero, J. J. De Miguel, R. Miranda, and A. Hernando, "Thickness-dependent coercivity of ultrathin Co films grown on Cu(111)," *Journal of Physics: Condensed Matter*, vol. 12, p. 7713, 2000.

[124] C. M. Schneider, P. Bressler, P. Schuster, J. Kirschner, J. J. De Miguel, and R. Miranda, "Curie temperature of ultrathin films of fcc-cobalt epitaxially grown on atomically flat Cu(100) surfaces," *Physical Review Letters*, vol. 64, p. 1059, 1990.

[125] P. Borisov, A. Hochstrat, X. Chen, W. Kleemann, and C. Binek, "Magnetoelectric switching of exchange bias," *Physical Review Letters*, vol. 94, p. 117 203, 2005.

[126] X. F. Zhou *et al.*, "Strong orientation-dependent spin-orbit torque in thin films of the antiferromagnet Mn_2Au," *Physical Review Applied*, vol. 9, p. 054 028, 2018.

[127] K. B. Urquhart, "The magnetic properties of ultrathin films of Fe(001) grown on Ag(001) substrates," Ph.D. dissertation, Simon Fraser University, 1989.

[128] B. T. Jonker, J. J. Krebs, and G. A. Prinz, "Growth and magnetic characterization of Mn films and superlattices on Ag(001)," *Physical Review B*, vol. 39, pp. 1399–1402, 1989.

[129] H. J. Elmers *et al.*, "Néel vector induced manipulation of valence states in the collinear antiferromagnet Mn_2Au," *ACS nano*, vol. 14, pp. 17 554–17 564, 2020.

[130] G. Longworth and B. Window, "Mössbauer studies of gold manganese alloys," *Journal of Physics F: Metal Physics*, vol. 1, p. 217, 1971.

[131] R. J. Hicken *et al.*, "Magnetic anistropy in ultrathin epitaxial Fe/Ag(100) films with overlayers," *Physical Review B*, vol. 55, p. 5898, 1997.

[132] D. Bruns, S. R. Lindemann, K. Kuepper, T. Schemme, and J. Wollschläger, "Fe3O4 films on Ag(001)—Generation of high-quality epitaxial ferrimagnetic metal oxide films," *Applied Physics Letters*, vol. 103, p. 052 401, 2013.

[133] R. M. Abrudan, "Growth, structure and magnetic properties of single crystalline Fe/CoO/Ag(001) bilayers," Ph.D. dissertation, Freie Universität Berlin, 2007.

[134] T. Ambrose and C. L. Chien, "Finite-size effects and uncompensated magnetization in thin antiferromagnetic CoO layers," *Physical Review Letters*, vol. 76, p. 1743, 1996.

[135] C. Won *et al.*, "Studies of FeMn/Co/Cu(001) films using photoemission electron microscopy and surface magneto-optic Kerr effect," *Physical Review B*, vol. 71, p. 024 406, 2005.

[136] R. K. Kawakami, E. J. Escorcia-Aparicio, and Z. Q. Qiu, "Symmetry-induced magnetic anisotropy in Fe films grown on stepped Ag(001)," *Physical Review Letters*, vol. 77, p. 2570, 1996.

[137] Y. Z. Wu, C. Won, and Z. Q. Qiu, "Magnetic uniaxial anisotropy of Fe films grown on vicinal Ag(001)," *Physical Review B*, vol. 65, p. 184 419, 2002.

[138] J. Chen and J. L. Erskine, "Surface-step-induced magnetic anisotropy in thin epitaxial Fe films on W(001)," *Physical Review Letters*, vol. 68, p. 1212, 1992.

List of Abbreviations

Å	Ångstrom
AES	Auger electron spectroscopyp
AFM	antiferromagnetic
Ag	silver
AMR	anisotropic magnetoresistance
Au	gold
bcc	body-centered cubic
c-fct	contracted face-centered tetragonal
CCD	charge-coupled device
CCT	constant-current tunneling
Co	Cobalt
Cu	Copper
e-fct	expanded face-centered tetragonal
EB	exchange bias
FC	field cooling
fcc	face-centered cubic
fct	face-centered tetragonal
Fe	Iron
FeMn	iron-manganese

FM	ferromagnetic
FvM	Frank-van der Merwe
GMR	giant magnetoresistance
h	hour
H_C	coercive field
H_{EB}	exchange-bias field
HZB	Helmholtz-Zentrum Berlin
IMFP	inelastic mean free path
IrMn	iridium-manganese
keV	kiloelectronvolt
kV	kilovolt
LEED	low-energy electron diffraction
LN_2	liquid nitrogen
MEED	medium-energy electron diffraction
ML	monolayer
Mn	Manganese
MOKE	magneto-optic Kerr effect
NiMn	nickel-manganese
PBN	pyrolytic boron nitride
PdMn	palladium-manganese
PtMn	platinum-manganese

Py	permalloy
QCM	quartz crystal microbalance
rf	radio frequency
RhMn	rhodium-manganese
RT	room temperature
RuMn	ruthenium-manganese
s	second
sc	simple cubic
SK	Stranski-Krastanov
SP-STM	spin-polarized scanning tunneling microscopy
STM	scanning tunneling microscopy
Ta	tantalum
TEY	total electron yield
TMP	turbomolecular pump
TMR	tunneling magnetoresistance
TSP	titanium sublimation pump
UHV	ultra high vacuum
VW	Volmer-Weber
W	tungsten
XAS	X-ray absorption spectroscopy
XMCD	X-ray magnetic circular dichroism

XMLD	X-ray magnetic linear dichroism
XRMR	X-ray resonant magnetic reflectometry
XRR	X-ray reflectivity
ZFC	zero-field cooling

List of Publications

1. Kumberg, I., Golias, E., Pontius, N., Hosseinifar, R., Frischmuth, K., **Gelen**, **I.**, ... & Kuch, W. (2020). Accelerating the laser-induced demagnetization of a ferromagnetic film by antiferromagnetic order in an adjacent layer. Physical Review B, 102(21), 214418.
2. Golias, E., Kumberg, I., **Gelen**, **I.**, Thakur, S., Gördes, J., Hosseinifar, R., ... & Kuch, W. (2021). Ultrafast optically induced ferromagnetic state in an elemental antiferromagnet. Physical Review Letters, 126(10), 107202.
3. Shinwari, T., **Gelen**, **I.**, Shokr, Y. A., Kumberg, I., Sajjad, M., Kuch, W., & Khan, M. Y. (2021). Bulk and Interfacial Effects in the Co/Ni_xMn_{100-x} Exchange-Bias System due to Creation of Defects by Ar+ Sputtering. Physica Status Solidi (RRL)–Rapid Research Letters, 15(9), 2100195.
4. Shinwari, T., **Gelen**, **I.**, Villanueva, M., Kumberg, I., Shokr, Y. A., Khan, M. Y. & Kuch, W. (2023). Growth, structure, and magnetic properties of artificially layered NiMn in contact to ferromagnetic Co on $Cu_3Au(001)$. Physica Status Solidi (B), 2200518.
5. **Gelen, I.**, Shinwari, T., Kumberg, I., Hadjadj S. E., Shokr, Y. A., Golias, E., and Kuch, W. Mn_xAu_{1-x} growth on Cu(001) and Ag(001) (in preparation).

Appendices

APPENDIX A

Au/Mn/Co/Cu(001)

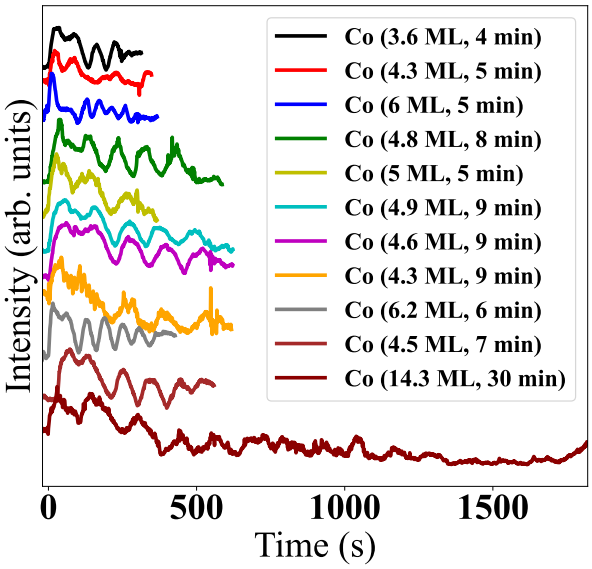

Figure A.1: The MEED oscillations for Co growth on Cu(001) from 3.6 to 14.3 ML. The ”0” defines the shutter open and the closing time is defined in the label in the bracket.

APPENDIX B

Co/Mn_xAu_{1-x} Bilayer Growth on Cu(001)

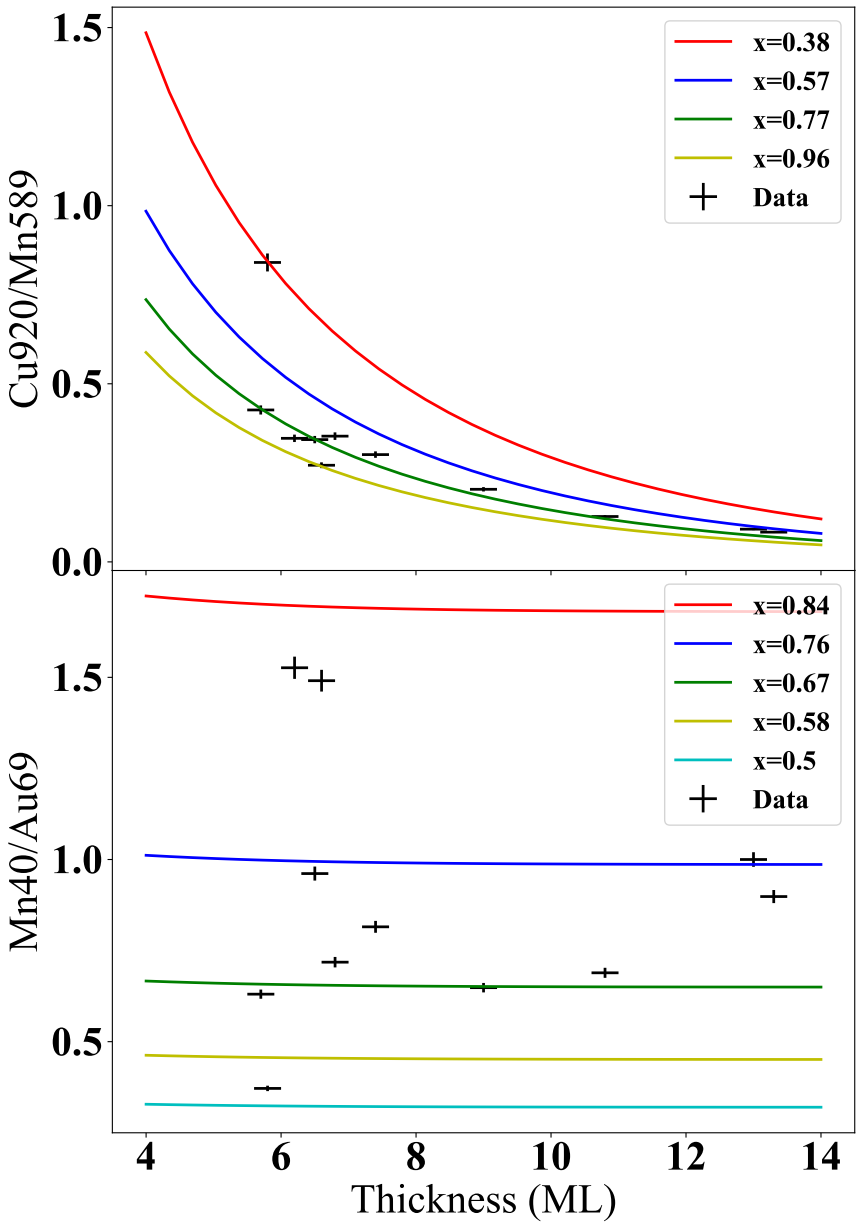

Figure B.1: Mn_xAu_{1-x} film composition (x) evaluation from the AES (a) Mn(589eV)/Cu(920eV) and (b) Mn(40 eV)/Au(69 eV) ratios for the samples in Fig. 6.2. The results are presented in Tab. 6.1.

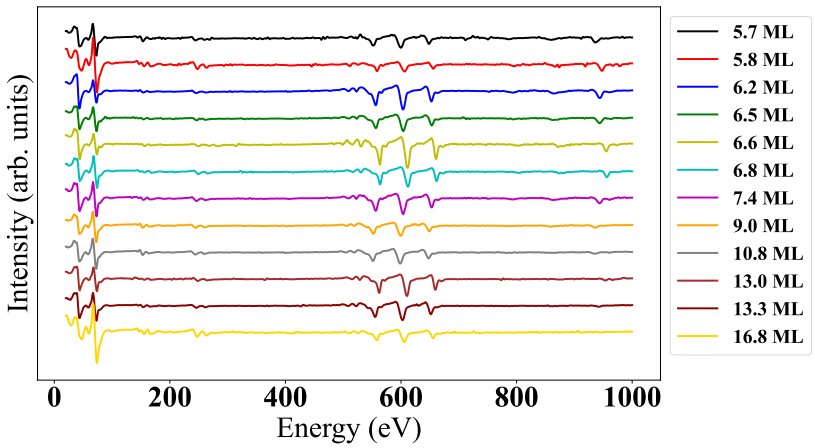

Figure B.2: AES spectra of Mn_xAu_{1-x} (from 5.7 to 16.8 ML) on Cu(001) for the samples in Fig. 6.2.

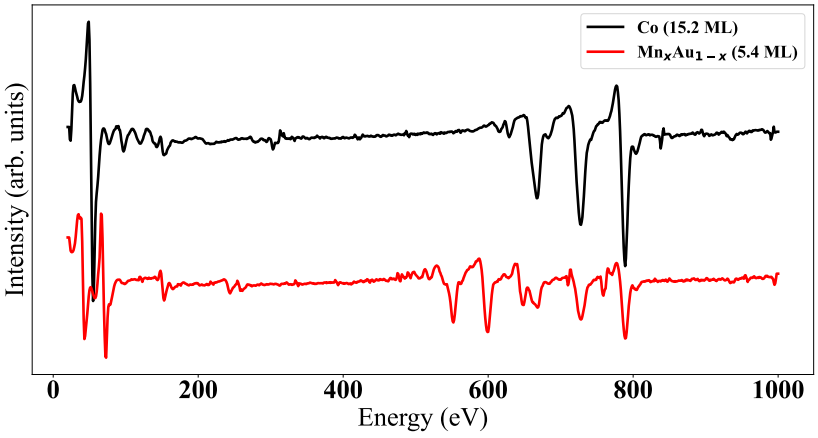

Figure B.3: AES spectra of 15.2 ML Co on Cu(001) and 5.4 ML $Mn_{0.72}Au_{0.28}$ on Co(15.2 ML)/Cu(001) sample, corresponding to the MEED oscillations shown in Fig. 6.2.

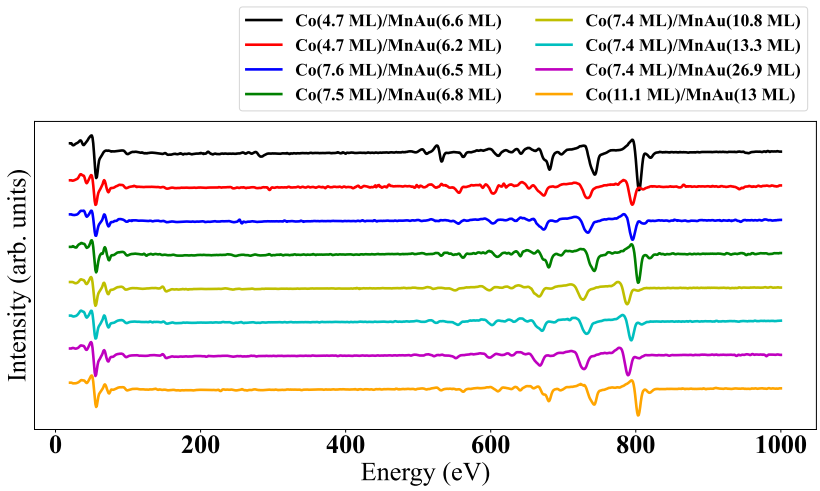

Figure B.4: AES spectra of Co on Cu(001) and Mn_xAu_{1-x} on Co/Cu(001) samples. AES spectra of samples that are used in Chapter. 6.

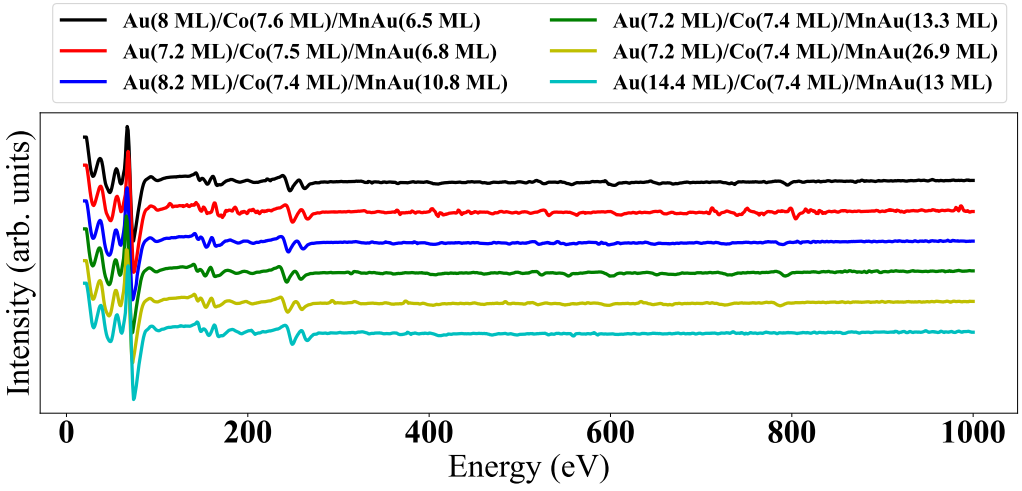

Figure B.5: AES spectra of Au/Co/Mn_xAu_{1-x}/Cu(001) samples. AES of samples that are used in Chapter. 6.

APPENDIX C

Fe/Mn_xAu_{1-x} Bilayer Growth on Ag(001)

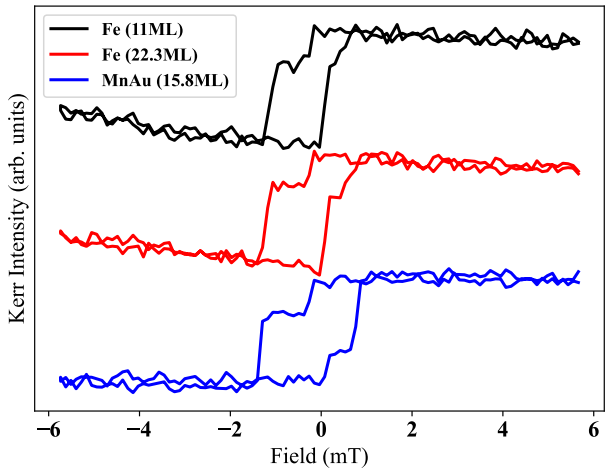

Figure C.1: L-MOKE of Fe (11 ML) and Fe (22.3 ML) on Ag(001), and L-MOKE of $Mn_{0.99}Au_{0.01}$ (15.8 ML) on Fe (22.3 ML).

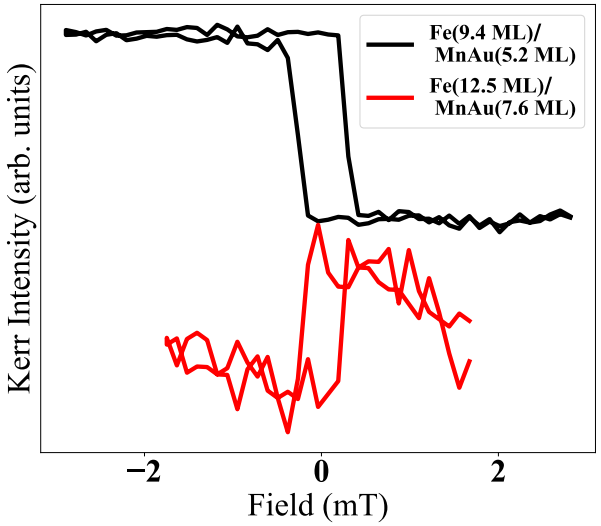

Figure C.2: L-MOKE of 9.4 and 12.5 ML Fe on 5.2 $Mn_{0.88}Au_{0.12}$ and 7.6 ML $Mn_{0.77}Au_{0.23}$, post-annealed at 600 K for 3 min, respectively, on Ag(001). The reversed sign of the MOKE signal is due to a different polarizer setting.

ACKNOWLEDGEMENTS

First of all, I want to express my gratitude to my supervisor, Prof. Dr. Wolfgang Kuch, for the opportunity to do my Ph.D. in his research group and for his continuous support and understanding. He was always there for open discussions on physics, related or not to this work. I would like to thank Prof. Dr. Paul Fumagalli for being my second supervisor and for offering me the opportunity to give presentations in his group and discuss my thesis with him.

I would like to thank Dr. Ivar Kumberg, Dr. Tauqir Shinwari, Dr. Evangelos Golias, and Dr. Yasser Shokr for their technical support and scientific discussion.

I would like to thank Dr. Sangeeta Thakur, Rahil Hosseinifar, Sebastien Hadjadj, David Swerev, Jorge Torres, Marcel Walter, Jendrik Gördes, and Awsaf Chowdhury for spending valuable time together.

I thank our former group fellows for their cooperation: Prof. Dr. Mustafa Erkovan, Dr. Lalminthang Kipgen, Dr. Matthias Bernien, Dr. Andrew J. Britton, Dr. Fabian Nickel, Dr. Lucas M. Arruda, Travis Edward Gustafson, and Oliver Sandig.

Thanks to AG Kuch's former secretary Marion Badow, who helped me with order-related work. I want to thank Christiane Cech for her paperwork, Uwe Lipowski for technical assistance, especially for building a new flashing stage and a motor system for the manipulator.

I want to thank the electronic and mechanic workshops of the physics department for their help.

I am grateful to the Republic of Türkiye Ministry of National Education and Freie Universität Berlin for their financial support.

In the end, I consider it obligatory to acknowledge and thank all members of my family, my parents, and my brothers and sisters. I dedicate my thesis to my wife Saadet, her love and care always encouraged me to do my best, and to my little daughters Zümra and Emma.